Determination of the phase diagram of Quantum Chromodynamics from the regions with no sign problem

境, 祐二
九州大学大学院理学府

https://doi.org/10.15017/21708

Determination of the phase diagram of Quantum Chromodynamics from the regions with no sign problem

Yuji Sakai

Theoritical Nuclear Physics, Department of Physics,
Graduate School of Sciences, Kyushu University

Acknowledgements

I would like to express my special gratitude to Prof. Masanobu Yahiro who is teaching and supporting me as a supervisor. By his valuable suggestions through many discussions, my Master and Doctoral Course become a fruitful and wonderful period in my life. I would like to thank Prof. Masayuki Matsuzaki and Associate Prof. Hiroaki Kouno who gave me a lot of useful comments and helpful discussions on this thesis. Through many discussions, I was able to obtain much beneficial knowledge. I wish to express my deep appreciation to Associate Prof. Yoshifumi R. Shimizu, Assistant Prof. Kazuyuki Ogata and Assistant Prof. Takuma Matsumoto. They gave me much important knowledge of Nuclear Physics from all seminars, lessons and discussions. I would like to thank Assistant Prof. Namiko Mitarai for her helpful comments in the Front Researcher Development program. I would like to thank my friends in the Nuclear Theory Group and other divisions in Kyushu University. This work was supported by the Research Fellowships of the Japan Society for the Promotion of Science (JSPS) for Young Scientists. Finally, I deeply appreciated grateful supports of my families who stood by me and gave me intelligent advices whenever I was at a loss what to do. Without their supports I never accomplished this great works.

Abstract

Quantum chromodynamics (QCD) is the theory of the strong interaction between quarks and gluons. The interaction becomes small at high energy, while it does strong at low energy. It is highly expected from the energy dependence that the QCD matter at high temperature T and/or high quark chemical potential $\mu_{\rm q}$ experiences a phase transition from a confined state with the chiral symmetry breaking to a deconfined state with the symmetry restoration. The phase diagram in the T-$\mu_{\rm q}$ plane is relevant to the early universe, compact stars and heavy-ion collisions. The first-principle lattice QCD (LQCD) suffers from the sign problem at finite $\mu_{\rm q}$ where the integrand of the partition function is complex and LQCD techniques break down. Therefore the QCD phase diagram at finite $\mu_{\rm q}$ is unclear. In this thesis, we propose a new strategy to investigate the QCD phase diagram at finite $\mu_{\rm q}$. There are some regions with no sign problem, imaginary $\mu_{\rm q}$ and real and imaginary isospin chemical potentials $\mu_{\rm iso}$. We then propose an analytic continuation from the regions with no sign problem to the real $\mu_{\rm q}$ region with the sign problem by using an effective model that can evaluate the QCD partition function in all the regions. The Polyakov-loop extended Nambu–Jona-Lasinio (PNJL) model is only the effective model that can do this. We show that the PNJL model reproduces LQCD data qualitatively in all the regions, but not quantitatively. We then extend the PNJL model in order to reproduce the LQCD data quantitatively. The QCD phase diagram at real $\mu_{\rm q}$ is predicted by the new model.

Contents

List of Figures

Chapter 1

Introduction

Quantum chromodynamics (QCD) is the theory of the strong interaction between quarks and gluons. The interaction becomes small at high energy, while it does strong at low energy. As a result of the strong interaction, the QCD vacuum has two remarkable phenomena, spontaneous chiral symmetry breaking and confinement. The spontaneous chiral symmetry breaking provides us the mechanism of generation of massive nucleons from light quarks and that of pions as Nambu-Goldstone bosons. The confinement is a phenomenon that color charged particles, quarks and gluons, cannot be isolated. Since the interaction decreases with increasing the energy scale, it is natural to consider that the QCD matter at high energy density undergoes a phase transition from a confined state with the chiral symmetry broken to a deconfined state with the symmetry restored. The QCD phase diagram in the plane of temperature T and quark chemical potential $\mu_{\rm q}$ provides us many insights of nature. The early universe after the Big Bang would be very hot and thus have experienced the QCD phase transition at high T and low $\mu_{\rm q}$. The core of compact stellar objects such as neutron stars would be a relevant place for dense QCD matter at low T and high $\mu_{\rm q}$. Experimentally, the heavy-ion collisions, such as the Relativistic Heavy-ion Collider (RHIC) at BNL, the Large Hadron Collider (LHC) at CERN and Japan Proton Accelerator Research Complex (J-PARC) at JAEA and KEK, provides us with a chance to create hot and/or dense QCD matter. In order to investigate the QCD phase diagram, we have to deal with some nonperturbative methods. Lattice QCD (LQCD) is only a reliable method of solving the nonperturbative nature,

i.e., to evaluate the partition function numerically on a spacetime lattice. LQCD provides us many insights at finite T and zero $\mu_{\rm q}$; for example the chiral phase transition is crossover there. It, however, suffers from the sign problem at finite $\mu_{\rm q}$ where the integrand of the partition function is complex and thereby LQCD techniques break down. The QCD phase diagram at finite $\mu_{\rm q}$ is therefore unclear.

In this thesis, we propose a new strategy to investigate the QCD phase diagram at finite $\mu_{\rm q}$. There are some regions with no sign problem, imaginary $\mu_{\rm q}$, real and imaginary isospin chemical potentials $\mu_{\rm iso}$. We then propose an analytic continuation from the regions with no sign problem to the real $\mu_{\rm q}$ region by using an effective model that can evaluate the QCD partition function in all the regions. The Polyakov-loop extended Nambu–Jona-Lasinio (PNJL) model is an effective model that can do this. We show that the PNJL model reproduces LQCD data qualitatively in all the regions with no sign problem, but not quantitatively. We then extend the PNJL model in order to reproduce the LQCD results quantitatively.

This thesis is organized as follows. In Chapter 2, we overview properties of QCD at vacuum and the QCD phase diagram at finite T and $\mu_{\rm q}$. This shows current states and difficulties in the study of the QCD phase diagram. In Chapter 3, we recapitulate thermal properties of the PNJL model at zero $\mu_{\rm q}$. After these introductory chapters, Chapters 4-7 are devoted to our study. In Chapter 4, we investigate the sign problem by using the PNJL model. We evaluate the average phase factor as an indicator of the sign problem. The severe region where the factor is small or zero spreads widely over the phase diagram. It is thus difficult to investigate the phase diagram by LQCD directly. In Chapters 5 and 6, we analyze the imaginary $\mu_{\rm q}$ region and the real and imaginary $\mu_{\rm iso}$ regions with the PNJL model, respectively. For all the regions, the PNJL model reproduces the LQCD data qualitatively, but not for the coincidence between the chiral and deconfinement crossover transitions. In Chapter 7, we extend the PNJL model to solve this problem. The new model reproduces LQCD data quantitatively in all the regions with no sign problem. Finally we predict the QCD phase diagram with the new model.

Chapter 2

Quantum Chromodynamics

In this chapter we introduce Quantum chromodynamics (QCD) as the fundamental theory of strong interactions. We discuss two important phenomena of QCD vacuum, the spontaneous chiral symmetry breaking and confinement, which play an important role in later parts of this work. We also discuss the QCD phase diagram at finite temperature and finite quark chemical potential [1].

2.1 Quantum Chromodynamics

Quantum Chromodynamics (QCD), the non-Abelian gauge theory with color $SU(3)_{\rm c}$ gauge invariance, is the theory of the strong interaction. The fundamental degrees of freedom are spin-1 gauge bosons (gluons A_μ), and massive spin-$\frac{1}{2}$ fermions (quarks q). Gluons and quarks belong to the adjoint and fundamental representations of $SU(3)_{\rm c}$, respectively. QCD is defined as a field theory with the Lagrangian density,

$$\mathcal{L} = \bar{q}\left(i\gamma^\mu D_\mu - m\right) q - \frac{1}{4g^2} F^a_{\mu\nu} F_a^{\mu\nu}, \tag{2.1}$$

where m is the current quark mass, $D_\mu = \partial_\mu + iA^a_\mu t^a$ is the covariant derivative with the coupling constant g and t^a is the generators of $SU(3)_{\rm c}$ satisfying the commutation relations, $[t^a, t^b] = if^{abc}t^c$, and the normalization, $\mathrm{tr}(t^a t^b) = \frac{1}{2}\delta^{ab}$, where f^{abc} are the group structure constants. The field strength tensor is defined as $F^a_{\mu\nu} = \partial_\mu A^a_\nu - \partial_\nu A^a_\mu + f^{abc}A^b_\mu A^c_\nu$. The Lagrangian density is invariant under

the $SU(3)_{\rm c}$ gauge transformation

$$q \to U(x)q, \quad A_\mu \to U(x)(A_\mu + i\partial_\mu)U^\dagger(x), \tag{2.2}$$

where $U(x) = \exp(-i\theta^a(x)t^a)$. Since QCD is renormalizable, its bare parameters g and m depend on the energy scale Q. The renormalization group equation based on the perturbative calculation reads

$$\alpha(Q^2) = \frac{g(Q^2)}{4\pi} = \frac{1}{4\pi\beta_0 \ln(Q^2/\Lambda_{\rm QCD})}, \tag{2.3}$$

where $\beta_0 = \frac{1}{(4\pi)^2}\left(11 - \frac{2}{3}N_{\rm f}\right)$ and $N_{\rm f}$ is the number of quark flavors. The QCD scale parameter is given by $\Lambda_{\rm QCD} = \kappa \exp(-1/2\beta_0 g^2)$ with the renormalization point κ and determined from experiment to be $\Lambda_{\rm QCD} \approx 200{\rm MeV} \approx 1{\rm fm}^{-1}$. As long as $\beta_0 > 0$ ($N_{\rm f} \leq 16$), the running coupling decreases logarithmically at large energy (or short distance) so that the asymptotic freedom of QCD can be realized [2]. In contrast, the coupling increases at low energy and the perturbative calculation breaks down. Quarks have flavors of $N_{\rm f} = 6$ with the masses $m_u \approx m_d \approx 5{\rm MeV}$, $m_s \approx 150{\rm MeV}$, $m_c \approx 1.5{\rm GeV}$, $m_b \approx 5{\rm GeV}$, $m_t \approx 170{\rm GeV}$, respectively. In this thesis, we focus on physics at the energy scale $\sim \Lambda_{\rm QCD}$ and we consider mainly the two-flavor case of u and d, since the influence of heavy quarks is negligible there.

2.2 Symmetries in QCD Lagrangian

Symmetries of Lagrangian are important to describe a main property of theories. As for QCD, one of important symmetries is the chiral symmetry. In the massless limit $m = 0$, the QCD Lagrangian density (2.1) is divided into the left- and right-handed quark parts that are the eigenstates of the chirality operator γ_5, $q_{\rm R/L} = \frac{1}{2}(1 \pm \gamma_5)q$. In this limit, the QCD Lagrangian is thus invariant under the flavor $U(N_{\rm f})_{\rm L} \times U(N_{\rm f})_{\rm R}$ global transformation, $q_{\rm R/L} \to \exp\left(-i\theta^a t^a\right) q_{\rm R/L}$ where t^a is the generator of $U(N_{\rm f})$. This is the chiral symmetry. The transformation

converts the vector and axial-vector ones as

$$q \to e^{-i\theta_{\rm V}^a t^a} q, \quad q \to e^{-i\theta_{\rm A}^a t^a \gamma_5} q, \tag{2.4}$$

with $\theta_{\rm V} = \theta_{\rm L} = \theta_{\rm R}$ and $\theta_{\rm A} = -\theta_{\rm L} = \theta_{\rm R}$. The corresponding conserved currents are vector and axial-vector currents, $J_{\rm V}^{a\mu} = \bar{q}\gamma^\mu t^a q$ and $J_{\rm A}^{a\mu} = \bar{q}\gamma^\mu\gamma_5 t^a q$, and thereby they have the following relations

$$\partial_\mu J_{\rm V}^{a\mu} = i\bar{q}[m, t^a]q, \quad (a = 0, ..., N_{\rm f}^2 - 1), \tag{2.5}$$

$$\partial_\mu J_{\rm A}^{a\mu} = i\bar{q}\{m, t^a\}\gamma_5 q, \quad (a = 1, ..., N_{\rm f}^2 - 1), \tag{2.6}$$

$$\partial_\mu J_{\rm A}^{0\mu} = \sqrt{2/N_{\rm f}}\left(i\bar{q}m\gamma_5 q - \frac{2N_{\rm f}}{64\pi^2}F_a^{\mu\nu}\tilde{F}_{\mu\nu}^a\right), \tag{2.7}$$

where $\tilde{F}_{\mu\nu}^a = \epsilon_{\mu\nu\rho\sigma}F_a^{\rho\sigma}$ ($\epsilon_{0123} = 1$) is the dual field strength. The $U(1)_{\rm A}$ current $J_{\rm A}^{0\mu}$ is explicitly broken even at $m = 0$ by the quantum effect that is originated from the non-invariance of the path integral measure under the $U(1)_{\rm A}$ transformation. This gives rise to an unnaturally large η' meson mass.

2.3 QCD vacuum structure

Since the QCD running coupling becomes stronger at low energy, quarks and gluons interact nonperturbatively there. There are two remarkable phenomena in the nonperturbative regime, spontaneous chiral symmetry breaking and confinement.

2.3.1 Chiral symmetry breaking

The chiral symmetry $SU(N_{\rm f})_{\rm V} \times SU(N_{\rm f})_{\rm A}$ in the Lagrangian is broken at vacuum. Here we consider the $N_{\rm f} = 2$ case for simplicity. In nature, there is a triplet of light pseudoscalar mesons π, while the parity partner of scalar meson σ has much heavier mass. This mass gap is explained as spontaneous breaking of the chiral symmetry. For nonperturbative nature, the ground state $|0\rangle$ of QCD is symmetric only under the $SU(N_{\rm f})_{\rm V}$ transformation generated by the vector charges $Q_{\rm V}^a = \int d^3\mathbf{x} J_{\rm V}^{a0}$, i.e., $Q_{\rm V}^a|0\rangle = 0$, but not under the $SU(N_{\rm f})_{\rm A}$ transformation generated by the axial-vector charges $Q_{\rm A}^a = \int d^3\mathbf{x} J_{\rm A}^{a0}$, i.e., $Q_{\rm A}^a|0\rangle = |\pi^a\rangle \neq 0$, which is

energetically degenerate with the ground state $|0\rangle$ and which carries the quantum numbers of the corresponding axial charges. These are Nambu-Goldstone bosons of light pseudoscalar mesons. The $SU(N_{\rm f})_{\rm A}$ transformation of the pion state, $\pi^a = \bar{q} i\gamma_5 t^a q$, is given as, for $N_{\rm f} = 2$

$$[Q^a_{\rm A}, \bar{q} i\gamma_5 t^a q] = -i\delta^{ab}\bar{q}q, \tag{2.8}$$

thus the chiral partner of the pseudoscalar mesons is the sigma meson $\sigma = \bar{q}q$ and the expectation value of the σ state is an order parameter of the chiral symmetry,

$$\langle \bar{q}q \rangle = \langle \bar{q}_{\rm L} q_{\rm R} + \bar{q}_{\rm R} q_{\rm L} \rangle. \tag{2.9}$$

The decay amplitude of the pion is written as

$$\langle 0 | \, J^{a\mu}_{\rm A}(x) \, | \pi^b(p) \rangle = -ip^\mu f_\pi \delta^{ab} e^{-ipx}, \tag{2.10}$$

where f_π is the pion decay constant. By combining (2.6) with (2.8), we obtain

$$\langle 0 | \left[Q^1_{\rm A}, \partial_\mu J^{1\mu}_{\rm A} \right] | 0 \rangle = -\frac{i}{2}(m_u + m_d)\langle \bar{q}q \rangle, \tag{2.11}$$

where m_u and m_d are u and d quark masses, respectively. The expression on the left-hand side can also be calculated from (2.10) by inserting a complete set of pseudoscalar states in the commutator. Truncating this set by the one-pion states $|\pi^a\rangle$, one obtains

$$M_\pi^2 f_\pi^2 = -m \langle \bar{q}q \rangle + \mathcal{O}(m^2), \tag{2.12}$$

where the isospin symmetry is assumed, $m_u = m_d = m$. The relation (2.12) is called the Gell-Mann–Oakes–Renner relation [7]. Here inserting $f_\pi \approx 93$MeV, $M_\pi \approx 140$MeV and $m \approx 5$MeV into (2.12), we obtain $\langle \bar{q}q \rangle \approx -(250\text{MeV})^3$ and the chiral symmetry is spontaneously broken at vacuum.

2.3.2 Confinement

Another important aspect of nonperturbative QCD is quark confinement. The mechanism is however much less known. Confinement is the phenomenon that all color charges are completely screened in the far away region of the color source. In the heavy quark limit, confinement means that a system with a static color source and a static color sink at infinite separation has an infinite free energy. More precisely, the free energy $F_{\bar{Q}Q}$ of a heavy quark $\bar{Q}Q$ pair is proportional to the separation R of the two quarks. The free energy is obtained from the expectation value of the Wilson loop [8]

$$W(C) = \mathrm{Tr}\left[\mathcal{P}\exp\left(-i\oint_C A_\mu dx^\mu\right)\right], \tag{2.13}$$

where the integral is made over a closed path C and $\mathcal{P}$ denotes the path ordering. In order to relate the Wilson loop to the free energy, we consider the process where a heavy static $\bar{Q}Q$ pair is created at $x_0 = 0$, propagates to time $x_0 = T \to \infty$, and then is annihilated. The Euclidian amplitude for the process is obtained as

$$\left\langle Q\bar{Q}\right| e^{-HT} \left|Q\bar{Q}\right\rangle = \int \mathcal{D}A^a_\mu e^{-S - i\int A^a_\mu J^{a\mu} d^4x} = e^{-F_{\bar{Q}Q}(R)T}, \tag{2.14}$$

where H is the Hamiltonian and $F_{\bar{Q}Q}$ is the free energy. The current $J^{a\mu}$ describes the closed path C of the creation and annihilation of the $Q\bar{Q}$ pair. We take the current $J^{a\mu} = \oint_C dz^\mu t^a \delta^4(x - z)$ corresponding to a quark Q moving along the path C,

$$e^{-F_{\bar{Q}Q}(R)T} = \int \mathcal{D}A^a_\mu e^{-S - i\oint_C A^a_\mu t^a dx^\mu} = \langle W(C)\rangle. \tag{2.15}$$

Evaluating the expectation value of the Wilson loop, we thus get the free energy of a heavy static particle-antiparticle pair. The free energy proportional to the distance does not allow the flux to spread over infinite space. The factor of the proportionality is called string tension.

2.3.3 Relation between two phenomena

The chiral symmetry is realized only in the limit of light quark. Meanwhile, the confinement is well defined only at heavy quark masses. Thus the two phenomena can be considered in the opposite limits. Here we comment on the simple argument about the relation between the two phenomena. An argument [4] made by Casher is that the chiral symmetry should be broken in the confinement phase. The argument is simple and transparent. Suppose quarks are confined in hadrons and the attraction is chiral invariant. In a semi-classical description a bound state is constructed by superposing paths where the bound quarks have to reverse its direction of motion. Since the chirality, that is helicity in massless limit, is conserved in the interaction, the force can flip neither the spin nor the direction of motion due to the helicity conservation. In compensation for the chirality the chiral condensate has a non-zero expectation value and then the chiral symmetry is spontaneously broken in the confinement phase. Another argument [5] is based on the anomaly matching condition proposed by 't Hooft [6]. Some of the electroweak anomalies are canceled between quarks and leptons. Since the leptonic anomaly is unchanged in the confinement phase, the hadrons must represent the flavor anomalies of QCD and ensure the cancellation of the leptonic anomaly. We consider flavor currents such as a left-handed current $J_\mu = \bar{q}\xi(1-\gamma_5)\gamma_\mu q$ where ξ is some combination of the generators of $SU(N_\mathrm{f})$ with $\mathrm{tr}(\xi^3) \neq 0$. This current has an anomaly expressed as

$$r^\alpha \Gamma_{\mu\nu\alpha}(p,q,r) = i\frac{g^2}{4\pi^2}\mathrm{tr}(\xi^3)\epsilon_{\mu\nu\beta\gamma}p^\beta q^\gamma, \tag{2.16}$$

$$\Gamma_{\mu\nu\alpha}(p,q,r) = \int d^4x_1 d^4x_2 e^{ipx_1+iqx_2}\left\langle J_\mu(x_1)J_\nu(x_2)J_\alpha(0)\right\rangle \tag{2.17}$$

where $(p+q+r)^\alpha = 0$. This amplitude $\Gamma_{\mu\nu\alpha}$ has massless poles like p^2, q^2 or r^2. Thus the current J_μ has to create massless states, that is, the Nambu-Goldstone boson due to the spontaneous chiral symmetry breaking.

2.4 QCD phase diagram

Since the QCD running coupling decreases with respect to increasing the energy scale, it is natural to consider that the QCD matter at high energy density undergoes the phase transition from a confined state with the chiral symmetry breaking to a deconfined state with the chiral symmetry restoration. The former (latter) is called the hadron (quark-gluon plasma: QGP) phase. Since the intrinsic scale of QCD is $\Lambda_{\rm QCD} \sim 200$MeV, the QCD phase transition may take place around temperature $T \sim \Lambda_{\rm QCD}$ or the baryon number density $\rho_{\rm B}^{1/3} \sim \Lambda_{\rm QCD} = 1{\rm fm}^{-1}$. In the early universe about 10^{-5}s after the Big Bang, the universe would have

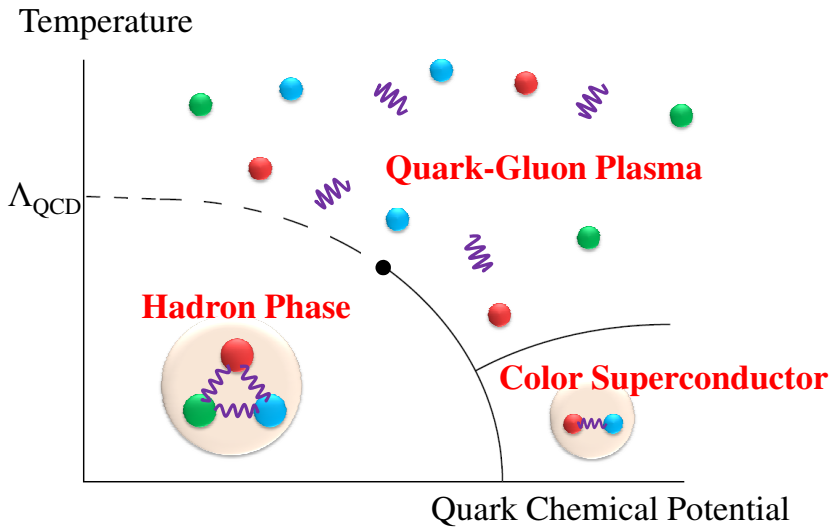

Figure 2.1: Schematic picture of the QCD phase diagram.

experienced the QCD phase transition. The core of compact stellar objects such as neutron stars thus would be the relevant place where dense QCD matter at low temperature is realized. For asymptotically high density, the QCD ground state forms a condensate of quark Cooper pairs, namely the color superconductor. Since quarks have color and flavor quantum numbers, the color superconductor phase has a rich structure. Experimentally, the heavy-ion collisions such as the Relativistic Heavy-ion Collider (RHIC) at BNL, the Large Hadron Collider (LHC) at CERN and Japan Proton Accelerator Research Complex (J-PARC) at JAEA

and KEK provides us with a chance to create hot and/or dense QCD matter [3]. Figure 2.1 sketches a schematic picture of the QCD phase diagram in the plane of temperature T and quark chemical potential $\mu_{\rm q}$. At present, our knowledge is limited only in asymptotically high $\mu_{\rm q}$ region, where the perturbative calculation is available, and small $\mu_{\rm q}/T \ll 1$ region, where the numerical calculation on lattice is available as explained in Sec. 2.6.

2.5 Thermodynamics of QCD

For QCD in equilibrium with volume V, temperature T and quark chemical potential $\mu_{\rm q}$, the partition function of the grand-canonical ensemble $Z(T,\mu_{\rm q})$ is defined as

$$Z(T,\mu_{\rm q}) = {\rm tr}\left(e^{-\beta(\hat{H}-\mu_{\rm q}\hat{N}_{\rm q})}\right), \tag{2.18}$$

where $\beta = 1/T$ and $\hat{H}$ and $\hat{N}_{\rm q}$ are the Hamiltonian and the quark-number operators, respectively. The thermodynamic potential is defined as $\Omega = -\frac{T}{V}\ln Z$. The partition function (2.18) is expressed as a Euclidian functional integral

$$Z(T,\mu_{\rm q}) = \int \mathcal{D}\bar{q}\mathcal{D}q\mathcal{D}A_\nu \exp\left[-\int_0^\beta d\tau \int d^3x \left(\mathcal{L}_{\rm E} - \mu_{\rm q}\bar{q}\gamma_4 q\right)\right], \tag{2.19}$$

where $\mathcal{L}_{\rm E}$ denotes the Lagrangian density in the Euclidian spacetime. Quarks and gluons satisfy antiperiodic and periodic boundary conditions in τ, respectively. Since the τ direction is compacted, the momentum integral is replaced as

$$\int \frac{d^4p}{(2\pi)^4} \xrightarrow{T\neq 0} \frac{1}{\beta}\sum_n \int \frac{d^3\mathbf{p}}{(2\pi)^3} \tag{2.20}$$

with the momentum $p = (\mathbf{p},\omega_n)$ where $\omega_n = 2n\pi T$ for gluons and $\omega_n = (2n+1)\pi T$ for quarks. From now on we work in Euclidean spacetime without exception. The Wilson loop (2.13) with the path connecting two points at $\tau = 0$ and β is then rewritten into

$$\langle W\rangle = \langle {\rm tr}_{\rm c} L^\dagger(\mathbf{R}){\rm tr}_{\rm c} L(\mathbf{0})\rangle = e^{-F_{\bar{Q}Q}(\mathbf{R})\beta}, \tag{2.21}$$

where $F_{\bar{Q}Q}(\mathbf{R})$ is the free energy of heavy quarks with the separation $\mathbf{R}$. Here the contributions from two paths in the opposite space direction at $\tau = 0$ and β are canceled out each other, note that the τ direction is compacted. The Polyakov loop Φ [9] is defined by

$$\Phi(\mathbf{x}) = \frac{1}{3}\mathrm{tr}_c L(\mathbf{x}), \quad L(\mathbf{x}) = \mathcal{P}\exp\left(-i\int_0^\beta A_4(\tau,\mathbf{x})d\tau\right), \tag{2.22}$$

where $\mathcal{P}$ denotes the path ordering. Therefore the Polyakov loop $\Phi(\mathbf{x})$ is related to the free energy $F_{\bar{Q}Q}$ at temperature T of two static color sources $\bar{Q}$ and Q with a spatial separation $\mathbf{R}$ [10]. In the limit $|\mathbf{R}| \to \infty$, the free energy is reduced to

$$F^\infty_{\bar{Q}Q} = -T\ln|\langle\Phi\rangle|^2. \tag{2.23}$$

This expression can be related to the free energy of a single quark, F^∞_Q, and a single antiquark, $F^\infty_{\bar{Q}}$. Consequently, $\langle\Phi\rangle$ is an order parameter for the confinement. In the confinement phase, the free energy is infinite so that $\langle\Phi\rangle = 0$, while $\langle\Phi\rangle \neq 0$ in the deconfinement phase. The Polyakov loop is also an order parameter of the $\mathbb{Z}_3$ symmetry [11] that is the center elements of color $SU(3)_c$, $z_k = e^{-2\pi ik/3}$ for integer k. Under a non-periodic gauge transformation $U_k(x) = [z_k]^{\tau/\beta}$, the temporal gauge field is shifted as $A_4 \to A_4 + \frac{2\pi k}{3\beta}$ so that the Polyakov loop is changed as $\Phi \to z_k\Phi$. The gauge fields satisfy the periodic boundary condition and the $\mathbb{Z}_3$ symmetry is exact in pure gauge limit. The boundary condition for quarks is however changed as $q(\beta,\mathbf{x}) = z_k q(0,\mathbf{x})$ under the transformation so that the $\mathbb{Z}_3$ symmetry is explicitly broken in the presence of quarks.

2.6 Lattice QCD

In order to investigate the QCD phase diagram, we have to deal with some non-perturbative methods. Only a reliable method to do this is lattice QCD (LQCD) where the partition function (2.19) is evaluated numerically on the spacetime lattice with a lattice spacing a by using importance sampling techniques. In LQCD, the ingredients are the link variables $U_\mu(n) = e^{-iaA_\mu(n)}$ that connect the neighbor sites at n and $n + \hat{\mu}$. The path integral over quark fields can be carried out

analytically:

$$Z = \sum_n \sum_\mu \det \mathcal{D}[U] e^{-S_g[U]}, \tag{2.24}$$

where $\mathcal{D}[U]$ tends to the Dirac operator $\gamma_\nu D_\nu + m - \mu_\mathrm{q}\gamma_4$ in the continuum limit. For a lattice with N_s (N_t) sites in each spatial (temporal) direction, the total number of integration is $N_s^3 \times N_t \times N_U$ where $N_U = 4 \times 8$ is degrees of freedom of the link variables at a point. For such a high-dimensional integral, Monte-Carlo methods with importance sampling are suitable where the sampling is generated with a probability proportional to $\det \mathcal{D}[U] e^{-S_g[U]}$. For finite quark chemical potential μ_q, the probability is no longer positive due to the property of the Dirac operator

$$\begin{aligned} [\det \mathcal{D}(\mu_\mathrm{q})]^* &= \det \left(\gamma_\nu D_\nu + m - \mu_\mathrm{q}\gamma_4\right)^\dagger \\ &= \det \left[\gamma_5 \left(\gamma_\nu D_\nu + m + \mu_\mathrm{q}^* \gamma_4\right) \gamma_5\right] = \det \mathcal{D}(-\mu_\mathrm{q}^*), \end{aligned} \tag{2.25}$$

so that the importance sampling techniques break down for finite μ_q. This is called the sign problem. Several approaches have been proposed so far to circumvent the difficulty; for example, the Taylor-expansion method [13], the reweighting method [12], and the analytic continuation from imaginary μ_q to real μ_q [34; 35; 36; 37]. The Taylor-expansion method has the convergence problem, i.e., the radius of convergence is limited to $\mu_\mathrm{q}/T < 1$. In the reweighting method, an expectation value of operator $\mathcal{O}$ at $\mu_\mathrm{q} \neq 0$ can be rewritten in terms of an ensemble average at $\mu_\mathrm{q} = 0$:

$$\langle \mathcal{O} \rangle_{\mu_\mathrm{q}} = \langle \mathcal{O} R(\mu_\mathrm{q}) \rangle_0 \Big/ \langle R(\mu_\mathrm{q}) \rangle_0, \tag{2.26}$$

where $R(\mu_\mathrm{q}) = \det \mathcal{D}(\mu_\mathrm{q}) / \det \mathcal{D}(0)$ is called the reweighting factor. The reweighting method has the overlap problem that the factor R is small in addition to the sign problem. For imaginary μ_q, there is no sign problem because of the relation (2.25). Quantities evaluated in LQCD at imaginaryμ_q can be continued to real μ_q by some analytic functions. The truncation of the functions, however, limits the range of applicability of this method. All the methods are still far from perfection

and the QCD phase diagram at finite μ_{q} is still under discussion.

Chapter 3

Polyakov-loop extended Nambu–Jona-Lasinio model

In the previous chapter, we discussed the QCD phase diagram. The first-principle lattice QCD (LQCD) is only a reliable method to investigate such a nonperturbative region, however it has the sign problem at finite quark chemical potential. As an approach complementary to LQCD, many effective models have been proposed so far. In the QCD phase diagram, important phenomena are chiral symmetry restoration and deconfinement. Recently an effective model which can treat both the phenomena was proposed. The model is call the Polyakov-loop extended Nambu–Jona-Lasinio (PNJL) model. In this chapter, we review properties of the PNJL model at finite temperature and zero chemical potential.

3.1 PNJL Model

The Nambu–Jona-Lasinio (NJL) model [14] has a long history and has been used extensively to describe the dynamics and the thermodynamics of light hadrons, including investigations of the phase diagrams [15]. Such a schematic model offers a simple and practical illustration of the mechanism of the spontaneous chiral symmetry breaking that is a key feature of low-energy QCD. The NJL model is based on an effective Lagrangian of quarks that interact through local current-current couplings, assuming that gluonic degrees of freedom can be frozen into

pointlike effective interactions between quarks. The gluonic correlation length calculated in lattice QCD (LQCD) [16] is small, say ~ 0.2 fm, compared with a characteristic momentum scale $\Lambda_{\rm QCD}^{-1} \approx 1$ fm. Consider the non-local interaction between two quark color currents, $J^{a\mu} = \bar{q}\gamma^\mu t^a q$, where t^a are the generators of the color $SU(3)_{\rm c}$ gauge group. The contribution of this current-current coupling to the action is

$$S_{\rm int} = -\frac{1}{2}\int d^4x d^4y J^{a\mu}(x) D^{ab}_{\mu\nu}(x-y) J^{b\nu}(y), \tag{3.1}$$

where $D^{ab}_{\mu\nu}$ is the full gluon propagator. This $S_{\rm int}$ generates the familiar one-gluon exchange between quarks and maintains its higher interactions. Since the gluonic correlation length is much shorter than the typical momentum scale of quarks, the interaction can be approximated by a local coupling between their color currents

$$S_{\rm int} = -G_{\rm c}\int d^4x J^{a\mu}(x) J^a_\mu(x). \tag{3.2}$$

By integrating out gluon degrees of freedom and absorbing them in the four-quark interaction $S_{\rm int}$, the local $SU(3)_{\rm c}$ gauge symmetry is now reduced to a global one in the NJL model. The interaction action $S_{\rm int}$ evidently preserves the chiral symmetry in the massless limit. A Fiertz transformation of the color current-current interaction (3.2) produces a set of exchange terms acting in quark-antiquark channels: for the two-flavor case,

$$S_{\rm int} \to -G_{\rm s}\int d^4x[(\bar{q}q)^2 + (\bar{q}i\gamma_5\vec{\tau}q)^2] + \cdots, \tag{3.3}$$

where $\vec{\tau}$ are the isospin $SU(2)$ Pauli matrix. The color-singlet pair of scalar-isoscalar and pseudoscalar-isovector operators (3.3) is a minimal subset satisfying the chiral symmetry. The four-quark interaction (3.3) is the starting point of the NJL model. The NJL model illustrates the spontaneous chiral symmetry breaking, that is, the generation of massive quasiparticles from light quarks and that of pions as Nambu-Goldstone bosons. Despite of the success to describe the chiral symmetry breaking, the NJL model lacks the confinement mechanism, a key feature of low-energy QCD besides the chiral symmetry breaking. The

deconfinement phase transition is characterized by spontaneous breaking of the $\mathbb{Z}_3$ center symmetry of color $SU(3)_c$ as discussed in Sec. 2.5. The order parameter is the Polyakov loop

$$\Phi(\mathbf{x}) = \frac{1}{3}\mathrm{tr}_c L(\mathbf{x}), \qquad L(\mathbf{x}) = \mathcal{P}\exp\left(-i\int_0^\beta d\tau A_4(\mathbf{x},\tau)\right), \tag{3.4}$$

where A_4 is the temporal gauge field and $\mathcal{P}$ denotes path ordering. The Polyakov-loop extended NJL (PNJL) model, recently proposed in Ref. [64], can describe the spontaneous breaking of the chiral symmetry and the deconfinement mechanism simultaneously. In the PNJL model, the coupling of the Polyakov loop Φ to the quark fields q is accomplished by the minimal gauge coupling procedure, where the temporal component of the gauge field is assumed to be spatially constant and the other components are neglected. Its basic ingredients are the NJL type four-quark contact interaction and the coupling to a spatially-constant temporal gauge field representing the Polyakov loop. The model Lagrangian is obtained in the Euclidian spacetime as

$$\mathcal{L} = \bar{q}(\gamma_\nu D_\nu + m_0)q - G_s[(\bar{q}q)^2 + (\bar{q}i\gamma_5\vec{\tau}q)^2] + U_\Phi, \tag{3.5}$$

where $D_\nu = \partial_\nu + iA_4\delta_{4\nu}$ and m_0 is the current quark mass. U_Φ is an effective potential for the Polyakov loop and is called as the Polyakov potential. In the PNJL model, the chiral and deconfinement transitions are described as the four-quark interaction and the Polyakov potential, respectively.

3.2 Polyakov potential

In the PNJL model the gluonic dynamics is incorporated into the Polyakov potential U_Φ. The functional form is inspired by the strong coupling expansion [17]. In the strong coupling limit, the effective action in terms of the Polyakov loop reads

$$S_L = -e^{-\sigma a\beta}\sum_{\text{n.n.}}\mathrm{tr}_c L^\dagger(\mathbf{x}_i)\mathrm{tr}_c L(\mathbf{x}_j), \tag{3.6}$$

which describes a hopping interaction between adjacent Polyakov loops. Here a and σ are the lattice spacing and the string tension, respectively. This action is similar to the nearest neighbor interaction of a spin system of the Polyakov loop. The partition function of the action is

$$Z_\Phi = \int \mathcal{D}L \; e^{-S_L} = e^{-V_\Phi^{\rm eff}}, \tag{3.7}$$

where $\mathcal{D}L$ represents the functional integral with the group invariant (Haar) measure, i.e., the Faddeev-Popov determinant. In the mean field approximation, the effective potential (per volume) for the Polyakov loop is obtained as

$$V_\Phi^{\rm eff} = -54 e^{-\sigma a/\beta} \Phi^* \Phi - \ln \mathcal{M}_{\rm Haar}, \tag{3.8}$$

where the Haar measure for the $SU(3)_{\rm c}$ group is given by

$$\mathcal{M}_{\rm Haar} = 1 - 6\Phi^*\Phi + 4(\Phi^{*3} + \Phi^3) - 3(\Phi^*\Phi)^2 \tag{3.9}$$

in the Polyakov gauge where the temporal gauge field is diagonal and static. The second term in (3.8) favors the confined state at $\Phi = 0$, while the first term does the deconfined state $\Phi = 1$. Thus, the Haar measure could play an essential role in the realization of the confinement [18]. Together with the two terms, a phase transition takes place. Here, we distinguish the conjugate of the Polyakov loop, $\Phi^* = \langle \frac{1}{3} {\rm tr}_{\rm c} L^\dagger \rangle$, from Φ; they are just identical at zero quark chemical potential, $\mu_{\rm q} = 0$, but a difference between them arises at finite $\mu_{\rm q}$. The difference has much to do with the sign problem as discussed in Sec. 4.6.1. Inspired by the functional form from the strong-coupling analysis, we adopt the following ansatz to fit the pressure in the pure gluonic sector [25]:

$$U_\Phi = -\frac{a(T)}{2}\Phi^*\Phi + b(T) \ln[1 - 6\Phi^*\Phi + 4(\Phi^{*3} + \Phi^3) - 3(\Phi^*\Phi)^2]. \tag{3.10}$$

The parameters are determined to reproduce the LQCD data [19] in the pure gauge limit, $a(T)/T^4 = 3.51 - 2.47t + 15.2t^2$ and $b(T)/T^4 = -1.75t^3$ with $t = T_0/T$. The first term in $a(T)$ is constrained by the Stefan-Boltzmann limit at $T \to \infty$. The potential enforces the first-order phase transition at $T = T_0$ and

LQCD yields $T_0 = 270$ MeV in pure gauge limit.

3.3 Thermodynamics in the PNJL model

3.3.1 Thermodynamic potential

Given the PNJL model Lagrangian (3.5), we can discuss the thermodynamics. We start with the partition function

$$Z = \int dA_4 \mathcal{D}\bar{q}\mathcal{D}q \ \exp\left[-\int d^4x \left(\mathcal{L} - \mu_{\rm q}\bar{q}\gamma_4 q\right)\right], \tag{3.11}$$

where the temporal gauge field A_4 is assumed to be spatially and temporally constant in the PNJL model. For proceeding the path integral of the quark field q, we introduce the auxiliary bosonic fields, σ and $\vec{\pi}$.

$$\mathcal{N} = \int \mathcal{D}\sigma\mathcal{D}\pi_i \exp\left(-G_{\rm s}[(\bar{q}q - \sigma)^2 + (\bar{q}i\gamma_5\tau_i q - \pi_i)^2]\right). \tag{3.12}$$

Inserting the constant terms in the partition function, we can convert the four-quark interaction to the bosonic one. The path integration over the quark fields can be carried out and then the partition function is obtained as

$$Z = \int dA_4 \mathcal{D}\sigma\mathcal{D}\pi_i \ e^{-S_{\rm bos}}, \tag{3.13}$$

with the bosonized action

$$S_{\rm bos} = -\ln\det[\beta(\gamma_\nu D_\nu + M_{\rm q} - \mu_{\rm q}\gamma_4)] + \int d^4x \left(G_{\rm s}[\sigma^2 + \vec{\pi}^2] + U_\Phi\right), \tag{3.14}$$

where the symbol det denotes the functional determinant and $M_{\rm q} = m_0 - 2G_{\rm s}(\sigma + i\gamma_5\tau_i\pi_i)$ is the dynamical quark mass. We evaluate the partition function (3.13) in the mean field approximation. In the mean field approximation, the field variables φ are replaced by the mean fields $\bar{\varphi}$. The mean field configurations are spatially and temporally constants that contribute mostly to the path integral. In this approximation, the partition function is reduced to $Z = e^{-S(\bar{\varphi})} = e^{-\beta V\Omega}$, where Ω is the thermodynamic potential and V is the volume. The mean fields

are determined by minimizing the potential, i.e., the stationary condition

$$\frac{\partial\Omega}{\partial\varphi} = 0 \qquad \text{for} \quad \varphi = \bar{\varphi}. \tag{3.15}$$

For finite quark chemical potential $\mu_{\rm q}$, the action (3.14) is in general complex. It is then difficult to take the configurations that most contribute to the partition function, i.e., the sign problem. We address this problem in Chapter 4. Here we consider only the zero $\mu_{\rm q}$ case where the action remains real. The thermodynamic potential Ω in the mean field approximation is obtained as

$$\Omega_{\rm mf} = -2N_{\rm f}\frac{1}{\beta}\sum_n \int^{\Lambda} \frac{d^3\mathbf{p}}{(2\pi)^3}{\rm tr_c}\ln\left[(\omega_n^{\rm c})^2 + \mathbf{p}^2 + M_{\rm q}^2\right] + G_{\rm s}[\sigma^2 + \pi_i^2] + U_\Phi, \tag{3.16}$$

where $\omega_n^{\rm c} = \omega_n - i\mu_{\rm q} - A_4$ and $\omega_n = (2n+1)\pi T$ are the Matsubara frequencies for quarks. Here we introduce the momentum cutoff Λ since the PNJL model is nonrenormalizable. We assume that there is no pion condensate $\langle\pi_i\rangle = 0$, which is justified whenever the isospin chemical potential is zero. By using some technique for the sum, the first term of the potential becomes

$$\ln\left[(\omega_n^{\rm c})^2 + \mathbf{p}^2 + M_{\rm q}^2\right] = \left[E_{\rm q} + \ln\left(1 + Le^{-\beta(E_{\rm q}-\mu_{\rm q})}\right) + \ln\left(1 + L^\dagger e^{-\beta(E_{\rm q}+\mu_{\rm q})}\right)\right] \tag{3.17}$$

with the quasiparticle energy $E_{\rm q} = \sqrt{\mathbf{p}^2 + M_{\rm q}^2}$ and $L = e^{-i\beta A_4}$ in the Polyakov gauge. Furthermore the color trace is explicitly taken to be a form of

$${\rm tr_c}\ln\left(1 + Le^{-\beta(E_{\rm q}-\mu_{\rm q})}\right) = \ln\left(1 + 3\Phi e^{-\beta(E_{\rm q}-\mu_{\rm q})} + 3\Phi^* e^{-2\beta(E_{\rm q}-\mu_{\rm q})} + e^{-3\beta(E_{\rm q}-\mu_{\rm q})}\right), \tag{3.18}$$

$${\rm tr_c}\ln\left(1 + L^\dagger e^{-\beta(E_{\rm q}+\mu_{\rm q})}\right) = \ln\left(1 + 3\Phi^* e^{-\beta(E_{\rm q}+\mu_{\rm q})} + 3\Phi e^{-2\beta(E_{\rm q}+\mu_{\rm q})} + e^{-3\beta(E_{\rm q}+\mu_{\rm q})}\right). \tag{3.19}$$

From the stationary condition for σ, we can get the relation

$$\langle\sigma\rangle = -4N_{\rm f}\frac{1}{\beta}\sum_n \int \frac{d^3\mathbf{p}}{(2\pi)^3}{\rm tr_c}\left(\frac{M_{\rm q}}{(\omega_n^{\rm c})^2 + \mathbf{p}^2 + M_{\rm q}^2}\right) = \langle\bar{q}q\rangle, \tag{3.20}$$

that is the self-consistence condition in the PNJL model. This relation connects the scalar meson field σ to the chiral condensate.

3.3.2 Meson properties

Here we consider the mesonic fluctuations around the mean fields. We write $\sigma(x) = \langle\sigma\rangle + \delta\sigma(x)$, $\pi_i(x) = \delta\pi_i(x)$ and expand the bosonized action (3.14) per volume around the mean field up to the second order of the mesonic fluctuations $\delta\sigma$, $\delta\pi$

$$S_{\rm bos} = S^{(0)}_{\rm bos} + S^{(2)}_{\rm bos}, \tag{3.21}$$

where $S^{(0)}_{\rm bos}$ corresponds to the mean field part (3.16). The second term is obtained as

$$S^{(2)}_{\rm bos} = \frac{1}{2}\int \frac{d^4p}{(2\pi)^4}\left(F^+(p^2)\delta\sigma(p)\delta\sigma(-p) + F^-(p^2)\delta\pi_i(p)\delta\pi_i(-p)\right), \tag{3.22}$$

where $p = (\mathbf{p}, \omega_m)$ with the Matsubara frequencies $\omega_m = 2m\pi T$ for meson. The inverse meson propagators, $F^+(p^2) = \frac{1}{V}\frac{\delta^2 S_{\rm bos}}{\delta\sigma(p)\delta\sigma(-p)}$ and $F^-(p^2) = \frac{1}{V}\frac{\delta^2 S_{\rm bos}}{\delta\pi(p)\delta\pi(-p)}$, are obtained as

$$F^\pm(p^2) = \int \frac{d^4q}{(2\pi)^4}{\rm tr}\left[\Gamma^\pm S(q^+)\Gamma^\pm S(q^-)\right] + 2G_{\rm s} = (2G_{\rm s})^2\left(N^\pm I(p^2) + \frac{m_0}{2G_{\rm s}M_{\rm q}}\right), \tag{3.23}$$

where $S(q^\pm) = (i\gamma\cdot q^\pm + M_{\rm q})^{-1}$ is the quark propagator with $q^\pm = q \pm p/2$ and $q = (\mathbf{q}, \omega^{\rm c}_n)$. The trace is taken over Dirac, flavor and color. The symbol $+(-)$ represents the σ (π_i) meson mode and $N^+ = p^2 - 4M_{\rm q}^2$, $N^- = p^2$, $\Gamma^+ = 1$, $\Gamma^- = i\gamma_5\tau_i$ and

$$I(p^2) = 2N_{\rm f}\int \frac{d^4q}{(2\pi)^4}{\rm tr}_{\rm c}\frac{1}{[(q^+)^2 + M_{\rm q}^2][(q^-)^2 + M_{\rm q}^2]}. \tag{3.24}$$

The pion mass M_π is determined by the pole of the pion propagator, while the quark-pion coupling constant $g^2_{\pi\bar{q}q}$ is by the residue of the pion pole,

$$M_\pi^2 = g^2_{\pi\bar{q}q}\frac{m_0}{2G_{\rm s}M_{\rm q}}, \quad g^{-2}_{\pi\bar{q}q} = I(p^2). \tag{3.25}$$

This relation shows that when the chiral symmetry is broken in the massless limit $m_0 = 0$, the pion behaves as the massless Nambu-Goldstone boson. The

pion decay constant is defined as the matrix element connecting the vacuum to the pion state through the axial current $J_{\mathrm{A}}^{a\mu}$. The pion decay constant therefore is evaluated as

$$if_\pi p^\mu \delta^{ab} = \langle 0|J_{\mathrm{A}}^{a\mu}(0)|\pi^b(p)\rangle = -ig_{\pi\bar{q}q}\delta^{ab}p^\mu M_{\mathrm{q}} I(p^2). \tag{3.26}$$

Combining (3.25) and (3.26), we obtain the Gell-Mann–Oakes–Renner relation

$$f_\pi^2 M_\pi^2 = \frac{m_0 M_{\mathrm{q}}}{2G_{\mathrm{s}}} = -m_0\langle\bar{q}q\rangle + \mathcal{O}(m_0^2). \tag{3.27}$$

3.3.3 Parameter set

The parameters of the PNJL model, G_{s}, Λ and m_0, are determined to reproduce the meson properties at vacuum, the pion mass $M_\pi = 138\mathrm{GeV}$ and its decay constant $f_\pi = 93.3\mathrm{MeV}$, and the chiral condensate $\langle\bar{q}q\rangle = (247\mathrm{MeV})^3$. The parameters result in $\Lambda = 631.5\mathrm{MeV}$, $G_{\mathrm{s}} = (426.5\mathrm{MeV})^{-2}$ and $m_0 = 5.5\mathrm{MeV}$ [20].

3.3.4 Chiral and deconfinement phase transitions

The order parameters of the chiral and deconfinement phase transitions are the chiral condensate σ and the Polyakov loop Φ, respectively. The critical temperatures of the phase transitions are determined by the peak positions of the corresponding susceptibilities,

$$\chi_\sigma = \chi_{\sigma\sigma} = \langle(\sigma - \langle\sigma\rangle)^2\rangle, \quad \chi_\Phi = \chi_{\Phi\Phi} = \langle(\Phi - \langle\Phi\rangle)^2\rangle, \tag{3.28}$$

for the chiral and deconfinement phase transitions, respectively . The susceptibility represents the correlation of the order parameters and has the maximum at the critical point. The susceptibilities $\chi_{\varphi_i\varphi_j}$ are defined as the inverse curvature matrix C of the potential

$$\chi_{\varphi_i\varphi_j} = C^{-1}_{\varphi_i\varphi_j}, \quad C_{\varphi_i\varphi_j} = \frac{\partial^2\Omega_{\mathrm{mf}}}{\partial\varphi_i\partial\varphi_j}, \tag{3.29}$$

where φ is the field variables. Figure 3.1 shows T dependence of σ (solid) and Φ

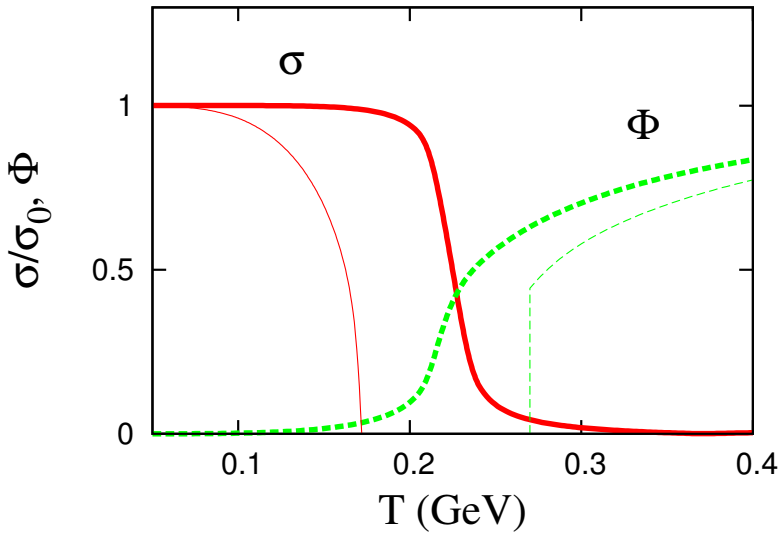

Figure 3.1: T dependence of the chiral condensate σ (solid) and the Polyakov loop Φ (dashed) at $\mu_{\rm q} = 0$. The chiral condensate is normalized by the value σ_0 at vacuum. The bold curves represent the PNJL model results, while the thin curves does the NJL model with $m_0 = 0$ for σ and the Polyakov potential for Φ.

(dashed) at $\mu_{\rm q} = 0$. The thin solid and dashed curves represent σ in only the NJL sector with $m_0 = 0$ and Φ calculated in only the Polyakov potential. In the case of no coupling between the quark fields and the Polyakov loop, the second-order chiral phase transition and the first-order deconfinement transition appear at very different critical temperatures, that is $T_\sigma \approx 172$MeV for the chiral phase transition and $T_\Phi \approx 270$MeV for the deconfinement one. The coupling between the quark fields and the Polyakov loop moves the deconfinement transition to lower temperature, while the chiral transition to higher temperature, and eventually both the transitions nearly coincide with each other, $T_\sigma \approx T_\Phi \approx 220$MeV. However the nearly coincidence temperature is different from LQCD one, $T_\sigma \approx T_\Phi \approx 173$MeV. The difference can be understood below [21]. The Polyakov potential U_Φ has a parameter to determine the scale of T, i.e., T_0. When only the Polyakov potential is considered, the first-order $\mathbb{Z}_3$ phase transition occurs at $T = T_0$ as shown by the thin-dashed curves of Fig. 3.1. The value of the QCD scale parameter $\Lambda_{\rm QCD}$ decreases as the number of flavor $N_{\rm f}$, so that T_0 decreases similarly. The $N_{\rm f}$ dependence is estimated with perturbation [21]. Here we determine $T_0 = 212$MeV to

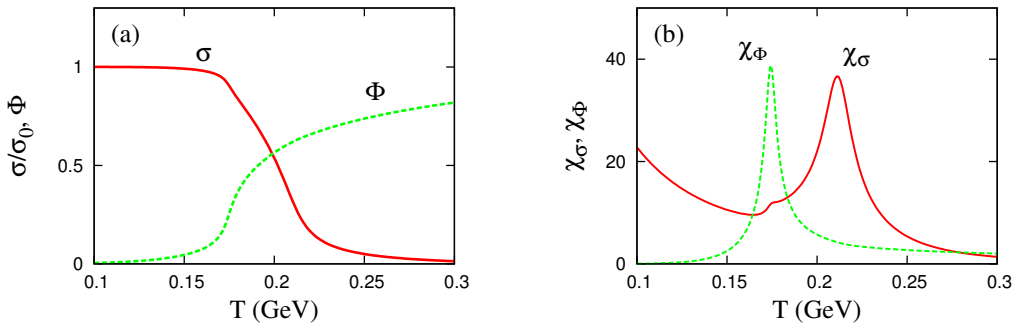

Figure 3.2: (a) T dependence of the chiral condensate σ (solid) and the Polyakov loop Φ (dashed) in the PNJL model with $T_0 = 212$MeV at $\mu_q = 0$. (b) T dependence of the susceptibilities χ_σ (solid) and χ_Φ (dashed) at $\mu_q = 0$.

reproduce $T_\Phi = 173$MeV of the LQCD result. Figure 3.2 (a) shows T dependence of σ and Φ with $T_0 = 212$MeV. Figure 3.2 (b) shows T dependence of the susceptibilities for σ and Φ, χ_σ and χ_Φ, with $T_0 = 212$MeV. The critical temperatures move to lower temperature and the values are $T_\sigma = 216$MeV and $T_\Phi = 173$MeV. The relative difference of the two critical temperatures is $T_\sigma - T_\Phi \approx 40$MeV. The result is inconsistent with the LQCD one where the two critical temperatures coincide with each other. We address this problem in Chapter 7. From now on $T_0 = 212$MeV is taken unless explicitly mentioned.

3.3.5 Thermodynamic quantities

Figure 3.4 shows T dependence of the pressure p at $\mu_q = 0$. The pressure is obtained from the thermodynamic potential Ω with $p = -\Omega$. In the mean field approximation, the pressure is determined by the quarks moving as quasiparticles in the background with the expectation values of the sigma field σ and the Polyakov loop Φ. In the hadronic phase at lower T, however, the mesonic contributions are dominant and we have to evaluate them. The mesonic contributions come from the effective action with the inverse propagators (3.22) of σ and π. In the pole approximation, where the imaginary part of the propagators corresponding to the decay modes is ignored, the inverse propagators of mesons with momentum p and masses M_m are proportional to $p^2 + M_m^2$, so that the mesonic

pressure $p_{\rm m}$ is obtained as

$$p_{\rm m} = -\frac{T}{2} \sum_{{\rm m}=\pi,\sigma} \int \frac{d^3\mathbf{p}}{(2\pi)^3} \ln\left(1 - e^{-\beta\sqrt{\mathbf{p}^2+M_{\rm m}^2}}\right). \tag{3.30}$$

Each meson mass is determined by a pole of each meson propagator (3.23). Figure

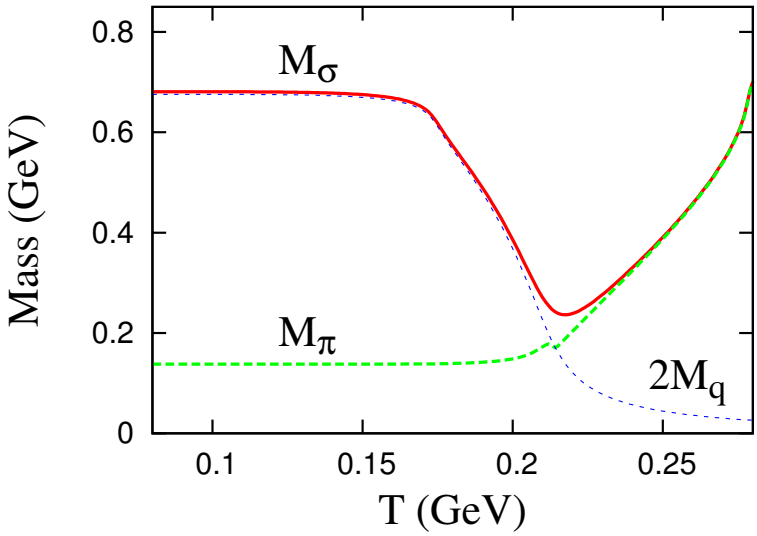

Figure 3.3: T dependence of the sigma M_σ (solid) and the pion mass M_π (dashed) at $\mu_{\rm q} = 0$. The dotted line shows twice the quark mass $M_{\rm q}$.

3.3 shows T dependence of the sigma-meson mass M_σ and the pion mass M_π at $\mu_{\rm q} = 0$. In the chiral symmetry broken phase at low T, the π meson behaves as the Nambu-Goldstone boson, while the σ meson has the mass about $2M_{\rm q}$. In the chiral symmetry restored phase at high T, the chiral partner, π and σ, degenerates with each other and the mass increases with T. Figure 3.4 shows T dependence of the pressure. The dashed and dotted curves represent the quark pressure in the mean field approximation and the mesonic pressure, respectively. The solid curve represents the total pressure in the mean field approximation plus the mesonic correction. In the confinement phase at low T, the pressure is dominated by the mesonic one. In the deconfinement phase at high T, the pressure is dominated by the quark-gluon one calculated in the mean field approximation.

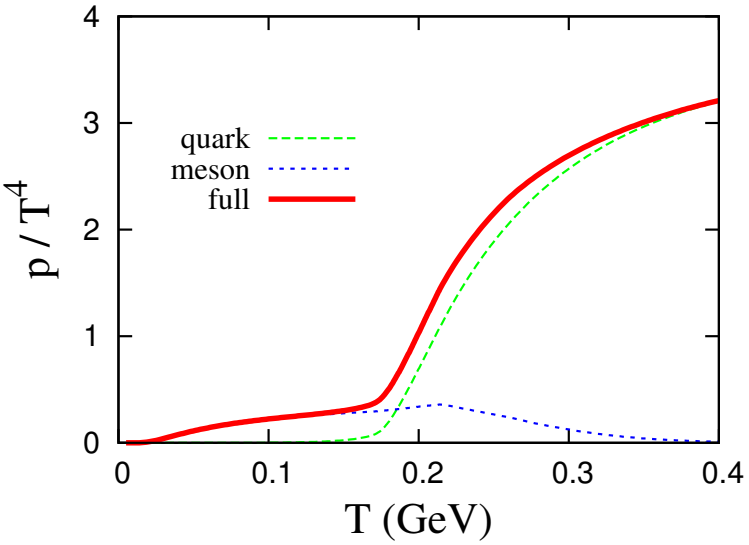

Figure 3.4: T dependence of pressure. The dashed and dotted curves represent the quark (in the mean field) and the mesonic pressure, respectively. The solid curve represents the total pressure of the mean field plus the mesonic correction.

3.4 Summary

We review thermodynamic properties of the PNJL model at zero quark chemical potential $\mu_{\rm q} = 0$. The PNJL model can treat both the chiral and deconfinement phase transition simultaneously. The model possesses the chiral properties such as the Gell-Mann–Oakes–Renner relation. Recent study [25] reported that the model reproduces the first-principle lattice QCD data at zero $\mu_{\rm q}$, but it is highly nontrivial whether the model predicts properly physical quantities at finite chemical potential. In this thesis, we propose a new approach to test the model reliability in the finite chemical potential regions. We show how reliable the PNJL model is and extend the model.

Chapter 4

Sign Problem

When we consider the effect of the quark chemical potential $\mu_{\rm q}$ in QCD, we encounter the sign problem. The integrand of the partition function with finite $\mu_{\rm q}$ oscillates hardly and hence the importance sampling in the Monte Carlo calculation breaks down. The sign problem appears even in the mean field approximation. In this chapter, we consider the sign problem by using the PNJL model. This chapter is mainly based on our paper of Ref. [22].

4.1 Sign Problem in the PNJL model

The PNJL model provides us with an ideal setup to consider the sign problem. The thermal part of the PNJL thermodynamic potential (3.16) is given by

$$\Omega^{\rm th}_{\rm PNJL} = -2N_{\rm f}\frac{1}{\beta}\int\frac{d^3\mathbf{p}}{(2\pi)^3}\sum_j\left\{\ln\left(1+e^{-\beta(E_{\rm q}-\mu_{\rm q}+i\phi_j)}\right)+\ln\left(1+e^{-\beta(E_{\rm q}+\mu_{\rm q}-i\phi_j)}\right)\right\} \quad (4.1)$$

with the Polyakov gauge where the temporal gauge fields ϕ_j is diagonal and static. For the $SU(N_{\rm c})$ gauge group, the gauge fields ϕ_j satisfy the condition, $\sum_j \phi_j = 0 \mod 2\pi/\beta$. The first and second logarithms represent quark and anti-quark excitations, respectively. In the $SU(2)$ gauge group, the terms with $j=2$ are the complex conjugate to the terms with $j=1$, since $\phi_1 = -\phi_2$. Thus the thermodynamic potential $\Omega_{\rm PNJL}$ is real and hence there is no sign problem. Unless the gauge group is $SU(2)$, the potential $\Omega^{\rm th}_{\rm PNJL}$ generally takes a complex value.

It is difficult to determine the energetically favorite values of internal variables, i.e., ϕ_j, from such a complex potential. This complex potential manifests the sign problem. The sign problem hinders the LQCD simulation at finite chemical potential. The sign problem is actually a quite generic problem of the importance sampling not only in the LQCD simulation but also in the mean field approximation. Note that the mean field variables are chosen to be a configuration that maximizes the weight $w \sim \exp(-\beta V\Omega)$. When the potential is complex, therefore, the mean field approximation breaks down. We can also use (4.1) in order to deduce the situation where the sign problem does not appear: for example,

- Isospin Chemical Potential
  We see from (4.1) that $\Omega_{\rm PNJL}(-\mu_{\rm q}) = \Omega^*_{\rm PNJL}(\mu_{\rm q})$, meaning that $\Omega_{\rm PNJL}$ is positive for two degenerate quarks that have a chemical potential opposite to each other. For example, $\mu_u = \mu_{\rm iso}$ for u-quarks and $\mu_d = -\mu_{\rm iso}$ for d-quarks when it is assumed that $m_u = m_d$. This reality of the potential comes from the property of the Dirac operator $\mathcal{D} = \gamma_\nu D_\nu + m - \mu_{\rm q}\gamma_4$,

  $$\det \mathcal{D}(\mu_u) \det \mathcal{D}(\mu_d) = |\det \mathcal{D}(\mu_{\rm iso})|^2 \geq 0. \tag{4.2}$$

  This relation shows that the theory with the isospin chemical potential corresponds to the phase-quenched theory. Some physical features of QCD at isospin chemical potential are addressed in Chapter 6.

- Imaginary Chemical Potential
  The sign problem is originated from the imbalance between the quark and antiquark loop in (4.1). The imbalance does not appear when $\mu_{\rm q}$ is purely imaginary, i.e., $\mu_{\rm q} = i\theta_{\rm q}/\beta$ for real $\theta_{\rm q}$. $\Omega_{\rm PNJL}$ is then obviously real. Note that, in this case, the thermodynamic potential has the dimensionless chemical potential only with the form $\theta_{\rm q} - \beta\phi_j$. The chemical potential therefore can be partially canceled by the $\mathbb{Z}_{N_{\rm c}}$ transformation, $\beta\phi_j \to \beta\phi_j + 2\pi/N_{\rm c}$. This means that the potential has a periodicity of $\theta_{\rm q}$ with $2\pi/N_{\rm c}$. Some physical features at imaginary chemical potential are addressed in Chapter 5.

In spite of the complex potential, the partition function and the expectation values of real fields have to be real. The reality is guaranteed by charge-conjugation symmetry of the partition function [23; 24]. The partition function Z is transformed is Z^C under charge-conjugation:

$$Z = Z^C = \int \mathcal{D}A^C e^{-S^C[A,\mu_\mathrm{q}]} = \int \mathcal{D}A\ e^{-S[A,-\mu_\mathrm{q}]} = \int \mathcal{D}A\ e^{-S^*[A,\mu_\mathrm{q}]} = Z^*, \quad (4.3)$$

where use has been made of the relation, $S[A,-\mu_\mathrm{q}] = S^*[A,\mu_\mathrm{q}]$. The partition function Z is thus real even at finite quark chemical potential. The expectation values can be evaluated similarly. Actually the expectation value of the complex Polyakov loop is real:

$$\langle\Phi\rangle = \int \mathcal{D}A_\nu\Phi\ e^{-S[A_\nu,\mu_\mathrm{q}]} = \int \mathcal{D}A_\nu\Phi^*\ e^{-S^*[A_\nu,\mu_\mathrm{q}]} = \langle\Phi\rangle^*, \quad (4.4)$$

where the Polyakov loop Φ is $\Phi = \frac{1}{N_\mathrm{c}}\mathrm{tr_c}\mathcal{P}(e^{-i\int_0^\beta A_4 d\tau})$ with the path ordering $\mathcal{P}$. The same can of course be written down for $\langle\Phi^*\rangle$. The expectation values $\langle\Phi\rangle$ and $\langle\Phi^*\rangle$ however differ from each other. The difference is physically natural. The Polyakov loop represents the propagation of a quark and its conjugate does of an antiquark. The chemical potential exceeds quarks over antiquarks, so at $\mu_\mathrm{q} \neq 0$, quarks and antiquarks propagate differently and then $\langle\Phi\rangle \neq \langle\Phi^*\rangle$.

4.2 Mean Field Approximation

In the mean field (MF) approximation, the MF variables are chosen to be a configuration that maximizes the weight $w \sim \exp(-\beta V\Omega)$. This approximation is guaranteed in the infinite volume limit $V \to \infty$. For the real potential, the MF variables satisfy the stationary condition where the potential is minimum. For the complex potential, however it is difficult to determine the MF variables. The imaginary part of the potential causes an oscillation with higher frequencies, so that the strong cancellation occurs in the integration. This is also the case for the PNJL model. The field configuration φ that contributes most importantly to the path integral is considered to be the configuration that minimizes the real

part of the potential. The necessary condition for this minimum is

$$\frac{\partial \mathrm{Re}\left(\Omega^{\mathrm{mf}}\right)}{\partial \varphi} = 0. \tag{4.5}$$

In addition, it has to be ensured that the MF configuration obtained by solving (4.5) leads to a real-valued thermodynamic potential. Two methods for making the MF approximation have been proposed so far in the PNJL model:

I) One method [25] is based on the assumption that, in the MF approximation, the expectation values of the gauge fields, $\langle\phi_3\rangle$ and $\langle\phi_8\rangle$, are related to these of the Polyakov loop, $\langle\Phi\rangle$ and $\langle\Phi^*\rangle$, through

$$\langle\Phi\rangle = \frac{1}{N_\mathrm{c}}\mathrm{tr}_\mathrm{c} e^{-i\beta(\langle\phi_3\rangle\lambda_3+\langle\phi_8\rangle\lambda_8)}, \quad \langle\Phi^*\rangle = \frac{1}{N_\mathrm{c}}\mathrm{tr}_\mathrm{c} e^{i\beta(\langle\phi_3\rangle\lambda_3+\langle\phi_8\rangle\lambda_8)}. \tag{4.6}$$

This condition is in general not true because Φ and Φ^* are nonlinear functions of ϕ_3 and ϕ_8. Under this condition, $\langle\Phi^*\rangle$ is the complex conjugate of $\langle\Phi\rangle$ even in the MF approximation. In order to keep the thermodynamic potential real, we have to take $\langle\Phi\rangle = \langle\Phi^*\rangle \in \mathbb{R}$, leading to $\langle\phi_8\rangle = 0$. The derivative $\frac{\partial\Omega^{\mathrm{mf}}}{\partial\phi_8}$ at $\langle\phi_8\rangle = 0$ is purely imaginary. The stationary condition (4.5) is satisfied under the condition $\langle\phi_8\rangle = 0$.

II) In the second method [64], the Polyakov loop Φ and its conjugate Φ^* are treated as the internal variables instead of the gauge fields ϕ_3 and ϕ_8. Since the gauge fields appear only as the Polyakov loop in the PNJL model, we can consider the Polyakov loop and its conjugate instead of the gauge fields. There is no relation between the expectation values of the Polyakov loop, $\langle\Phi\rangle$ and $\langle\Phi^*\rangle$, and these of the gauge field, $\langle\phi_3\rangle$ and $\langle\phi_8\rangle$. In this MF approximation, $\langle\Phi\rangle$ and $\langle\Phi^*\rangle$ differ from each other at finite chemical potential.

4.3 Average Phase Factor

The sign problem is the main obstacle for the first-principle numerical investigations of the QCD phase diagram. Several approaches have been proposed so

far to circumvent the difficulty: see Sec. 2.6 for the details. The success of the approaches is linked to how difficult the sign problem is. As a good indicator of the difficulty, we can consider the average of the phase factor

$$e^{2i\theta} = \frac{\det \mathcal{D}^2}{|\det \mathcal{D}|^2} \tag{4.7}$$

with the Dirac operator $\mathcal{D} = \gamma_\nu D_\nu + m - \mu_{\rm q}\gamma_4$. If the average of the phase factor is tiny, then severe cancellations take place in the path integral. In this situation, validity of LQCD computations should be examined carefully. Studies on the average phase factor are therefore important in order to understand the validity of LQCD computations. The average is obtained by taking the expectation value of the phase factor in the phase-quenched theory where the fermion determinant is replaced by the absolute value. In the two-flavor case, the average is

$$\left\langle e^{2i\theta} \right\rangle_{\rm pq} = \frac{\int \mathcal{D}A_\nu \; e^{2i\theta} |\det \mathcal{D}|^2 e^{-S[A_\nu]}}{\int \mathcal{D}A_\nu \; |\det \mathcal{D}|^2 e^{-S[A_\nu]}} = \frac{Z_{\rm full}}{Z_{\rm pq}}, \tag{4.8}$$

where $Z_{\rm full}$ is the partition function of the ordinary two-flavor theory and $Z_{\rm pq}$ is that of the two-flavor phase-quenched theory. Therefore, the average phase factor expresses how the phase-quenched theory is different from the full theory. In the two-flavor case, the phase-quenched theory with the quark chemical potential $\mu_{\rm q}$ is equivalent to the theory with the isospin chemical potential $\mu_{\rm iso} = \mu_{\rm q}$, as shown in (4.2).

4.4 Purpose

It is not easy to calculate the average phase factor with LQCD even for small chemical potential. Actually, several LQCD results on the average phase factor are spotted [27]. It is then important to make a systematic analysis on the phase factor by using effective theories. This was done by the chiral perturbation theory [28; 29]. The result is consistent with the LQCD one [27] at lower T. However, the theory is not valid for temperature near and above the transition one $T_{\rm c}$. The purpose of this chapter is to examine the average phase factor also above $T_{\rm c}$ where the chiral perturbation theory is not applicable. In order to carry

out such a study we have to rely on a specific model. Here we consider the PNJL model. The PNJL model is suitable for this study since the model has the sign problem induce by the Polyakov loop at finite chemical potential just like QCD. We evaluate the average phase factor with the MF approximation and investigate the relation between the Polyakov loop and the average phase factor. We also consider the dynamical mesonic fluctuations as a correction to the MF approximation and investigate the effect on the average phase factor.

4.5 Formulation

We start with the Lagrangian of the two-flavor PNJL model with the chemical potential $\hat{\mu}$,

$$\mathcal{L}_{\mathrm{PNJL}} = \bar{q}(\gamma_\nu D_\nu + m_0 - \gamma_4\hat{\mu})q - G_{\mathrm{s}}\left[(\bar{q}q)^2 + (\bar{q}i\gamma_5\vec{\tau}q)^2\right] + U_\Phi, \tag{4.9}$$

where $D_\nu = \partial_\nu + iA_4\delta_{4\nu}$. The chemical potential $\hat{\mu}$ takes $\hat{\mu} = \mu_{\mathrm{q}}$ for the full theory with the sign problem and $\hat{\mu} = \mu_{\mathrm{q}}\tau_3$ for the phase-quenched theory. Note that, as mentioned in (4.2), the phase-quenched theory is equivalent to the theory with the isospin chemical potential. Here we summarize the symmetries and their breaking patterns in the two theories. For $m_0 = \hat{\mu} = 0$, the PNJL Lagrangian has the $SU(2)_{\mathrm{L}} \times SU(2)_{\mathrm{R}} \times U(1)_{\mathrm{V}}$ symmetry. In the full theory, the symmetry is reduced to $SU(2)_{\mathrm{V}} \times U(1)_{\mathrm{V}}$ at finite quark masses. In the phase-quenched theory, furthermore, the symmetry is reduced to $U(1)_{\mathrm{I}_3} \times U(1)_{\mathrm{V}}$ at the finite chemical potential, where $U(1)_{\mathrm{I}_3}$ is the isospin subgroup and quark is transformed as $q \to e^{-i\alpha\tau_3}q$ under the transformation. The spontaneous breakings of the chiral and the $U(1)_{\mathrm{I}_3}$ symmetry are described, respectively, by the chiral condensate $\sigma = \langle\bar{q}q\rangle$ and the charged pion condensate $\pi = \langle\bar{q}i\gamma_5\tau_1 q\rangle$, where the τ_1 direction is taken as the $U(1)_{\mathrm{I}_3}$ symmetry breaking. In the full theory, the chiral symmetry is spontaneously broken but the $U(1)_{\mathrm{I}_3}$ symmetry is not. In the phase-quenched theory, both the chiral and $U(1)_{\mathrm{I}_3}$ symmetries are spontaneously broken[1].

[1] We address this point in Sec. 6.2.

4.5.1 Mean Field Approximation

As discussed in Sec. 4.2, the PNJL model has the sign problem, so that the mean field (MF) approximation cannot be defined uniquely. In the PNJL model, there are two kinds of the MF approximations. Here we take the method I) where the mean field variables $\varphi^{\rm mf} = (\sigma, \vec{\pi}, \phi_3, \phi_8)$ are obtained by the stationary condition

$$\frac{\partial\ {\rm Re}\left(\Omega^{\rm mf}\right)}{\partial\varphi} = 0, \quad \varphi = \varphi^{\rm mf} \tag{4.10}$$

under the constraint $\phi_8 = 0$ that keeps the thermodynamic potential real. In the MF approximation, we can obtain the MF Lagrangian as

$$\mathcal{L}^{\rm mf}_{\rm PNJL} = \bar{q}(\gamma_\nu\partial_\nu + \gamma_4\{iA_4 - \hat{\mu}\} + M_{\rm q} + Ni\gamma_5\tau_1)q + G_{\rm s}\left[\sigma^2 + \pi^2\right] + U_\Phi \tag{4.11}$$

with $A_4 = \phi_3\lambda_3 + \phi_8\lambda_8$ under the Polyakov gauge, $M = m_0 - 2G_{\rm s}\sigma$ and $N = -2G_{\rm s}\pi$. The thermodynamic potential is then obtained as

$$\Omega^{\rm mf} = -2\sum_{i=\pm}\int\frac{d^3\mathbf{p}}{(2\pi)^3}\left[3E^i_{\rm q} + \frac{1}{\beta}\ln\mathcal{F}(E^i_{\rm q})\right] + G_{\rm s}\left[\sigma^2 + \pi^2\right] + U_\Phi \tag{4.12}$$

with $\mathcal{F}(E^i_{\rm q}) = 1 + 3\Phi(e^{-\beta E^i_{\rm q}} + e^{-2\beta E^i_{\rm q}}) + e^{-3\beta E^i_{\rm q}}$. Note that $\Phi = \Phi^*$ in this MF approximation, since we set $\phi_8 = 0$. The difference between the full and the phase-quenched theory appears only though the quasi-particle energies $E^i_{\rm q}$. They are written as

$$E^+_{\rm q} = E_{\rm q} + \mu_{\rm q}, \quad E^-_{\rm q} = E_{\rm q} - \mu_{\rm q}, \tag{4.13}$$

for the full theory, and, as

$$E^+_{\rm q} = \sqrt{(E_{\rm q} + \mu_{\rm q})^2 + N^2}, \quad E^-_{\rm q} = \sqrt{(E_{\rm q} - \mu_{\rm q})^2 + N^2}, \tag{4.14}$$

for the phase-quenched theory. It is clear from (4.12)-(4.14) that when the pion condensation does not occur in the phase-quenched theory, the thermodynamic potential $\Omega_{\rm pq}$ is the same as the thermodynamic potential $\Omega_{\rm full}$ in the full theory. As discussed in Chapter 7, when the chemical potential exceeds half the pion

mass in the phase-quenched theory, the vacuum with the pion condensate is more stable than the vacuum without the pion condensate, that is, $\Omega_{\rm full} > \Omega_{\rm pq}$. The two thermodynamic potentials thus differ from each other there. In the MF approximation, the partition function $Z^{\rm mf}$ is proportional to $e^{-\beta V \Omega^{\rm mf}}$ and hence the average phase factor becomes

$$\langle e^{2i\theta} \rangle^{\rm mf} = \exp\left[-\beta V(\Omega^{\rm mf}_{\rm full} - \Omega^{\rm mf}_{\rm pq})\right]. \tag{4.15}$$

Therefore the average phase factor is $\langle e^{2i\theta} \rangle^{\rm mf}$ is 1 for the vacuum without the pion condensate, and $\langle e^{2i\theta} \rangle^{\rm mf}$ nearly zero for the vacuum with the pion condensate.

4.5.2 Effect of the Static Fluctuation

In the normal phase where there is no pion condensate, the average phase factor does not depend on temperature and chemical potential and hence an unphysical discontinuity appears when the chemical potential exceeds half the pion mass. This implies that we should consider the fluctuations around the MF. Here we consider the static (homogeneous) fluctuations (SF) up to the second order terms. The assumption $\phi_8 = 0$ is an approximation in the MF level. The gradient $\frac{\delta \Omega^{\rm mf}}{\delta \phi_8}$ is thus finite and pure imaginary. We expand $\Omega^{\rm mf}$ up to quadratic terms of the fluctuations:

$$\Omega^{\rm sf} = \Omega^{\rm mf} + \left(\frac{\delta \Omega^{\rm mf}}{\delta \phi_8}\right) \delta\phi_8 + \frac{1}{2}\left(\frac{\delta^2 \Omega^{\rm mf}}{\delta \varphi_i \delta \varphi_j}\right) \delta\varphi_i \delta\varphi_j, \tag{4.16}$$

where $\varphi_i = (\varphi_i)^{\rm mf} + \delta\varphi_i$ for mean fields $(\varphi_i)^{\rm mf}$ and static fluctuations $\delta\varphi_i$. Since first-order terms in $\delta\phi_8$ are purely imaginary, we can regard an integral over φ_i as a Fourier integral. We then obtain

$$Z^{\rm sf} = \int \Pi_i d(\delta\varphi_i) \exp\left(-\beta V \Omega^{\rm sf}\right) = \frac{1}{\mathcal{N}} \exp\left(-\beta V \tilde{\Omega}^{\rm sf}\right), \tag{4.17}$$

with

$$\tilde{\Omega}^{\rm sf} = \Omega^{\rm mf} + \frac{1}{2}\left(\frac{\delta^2 \Omega^{\rm mf}}{\delta \phi_8^2}\right)^{-1} \left(\frac{\delta \Omega^{\rm mf}}{\delta \phi_8}\right)^2, \quad \mathcal{N}^{\rm sf} = \left(\frac{\beta V}{2\pi}\right)^{n/2} \det\left(\frac{\delta^2 \Omega^{\rm mf}}{\delta \varphi_i \delta \varphi_j}\right)^{1/2}, \tag{4.18}$$

where n is the number of fields. Note that the correction term of the potential respects contributions from non-vanishing imaginary parts of the potential. The corrected potential $\tilde{\Omega}^{\rm sf}$ is real. The average phase factor with the static fluctuations turns out to be

$$\left\langle e^{2i\theta} \right\rangle = \frac{\mathcal{N}^{\rm sf}_{\rm pq}}{\mathcal{N}^{\rm sf}_{\rm full}} \exp\left[-\beta V \left(\tilde{\Omega}^{\rm sf}_{\rm full} - \tilde{\Omega}^{\rm sf}_{\rm pq} \right) \right]. \tag{4.19}$$

We can see some features from this explanation. When the pion condensate does not occur in the phase-quenches theory, the thermodynamic potentials of the full and phase-quenched theories coincide with each other even in the MF+SF approximation, $\tilde{\Omega}^{\rm sf}_{\rm full} = \tilde{\Omega}^{\rm sf}_{\rm pq}$. Thus the average phase factor is dominated by the prefactor $\mathcal{N}^{\rm sf}_{\rm pq}/\mathcal{N}^{\rm sf}_{\rm full}$. When the pion condensate occurs in the phase-quenched theory, a massless mode in the τ_2 direction appears because we choose the τ_1 direction as the massive mode. Thus the average phase factor vanishes because of

$$\left(\frac{\delta^2 \Omega^{\rm mf}}{\delta \pi_2 \delta \varphi_j} \right)_{\rm pq} = 0 \;\rightarrow\; \mathcal{N}^{\rm sf}_{\rm pq} = \det \left(\frac{\delta^2 \Omega^{\rm mf}}{\delta \varphi_i \delta \varphi_i} \right)_{\rm pq} = 0. \tag{4.20}$$

The expectation value of the Polyakov loop $\langle \Phi \rangle$ and its conjugate $\langle \Phi^* \rangle$ are calculated in the MF+SF level [25]:

$$\langle \Phi \rangle^{\rm sf} = \langle \Phi \rangle^{\rm mf} - \left(\frac{\partial \Omega^{\rm mf}}{\partial \phi_8} \right) \left(\frac{\partial^2 \Omega^{\rm mf}}{\partial \phi_8^2} \right)^{-1} \left(\frac{\partial \Phi^{\rm mf}}{\partial \phi_8} \right), \tag{4.21}$$

$$\langle \Phi^* \rangle^{\rm sf} = \langle \Phi^* \rangle^{\rm mf} - \left(\frac{\partial \Omega^{\rm mf}}{\partial \phi_8} \right) \left(\frac{\partial^2 \Omega^{\rm mf}}{\partial \phi_8^2} \right)^{-1} \left(\frac{\partial \Phi^{*\rm mf}}{\partial \phi_8} \right), \tag{4.22}$$

where the factor $\left(\frac{\partial \Phi^{*\rm mf}}{\partial \phi_8} \right)$ is the complex conjugate of $\left(\frac{\partial \Phi^{\rm mf}}{\partial \phi_8} \right)$ and both are purely imaginary. The factor $\left(\frac{\partial \Omega^{\rm mf}}{\partial \phi_8} \right)$ comes from the imaginary part of the potential and then purely imaginary. This property makes the expectation values, $\langle \Phi \rangle^{\rm sf}$ and $\langle \Phi^* \rangle^{\rm sf}$ purely real and the expectation values are split out each other due to the correction from the imaginary part of the potential induced by the gauge field ϕ_8.

4.5.3 Effect of the Dynamic Fluctuation

The static fluctuations should be considered for σ, $\vec{\pi}$, ϕ_3 and ϕ_8. The PNJL Lagrangian has the kinetic term for the quarks but not for the gauge fields, ϕ_3 and ϕ_8. Therefore we can consider both the dynamical and static fluctuations for the meson fields, σ and $\vec{\pi}$, while we keep treating only the static fluctuations for the gauge fields. Therefore, in (4.16), the second derivative terms with respect to the meson fields $\varphi = (\sigma,\ \vec{\pi})$ are rewritten as

$$\int d^4x d^4y \Gamma_{ij}(x-y)\delta\varphi_i(x)\delta\varphi_j(y), \quad \Gamma_{ij}(x-y) = \frac{\delta^2\Omega^{\rm mf}(x-y)}{\delta\varphi_i(x)\delta\varphi_j(y)}. \tag{4.23}$$

The second derivatives Γ_{ij} of the potential with respect to meson fields yield the inverse meson propagators. If there is no pion condensate, where the parity is not broken, the scalar- and the pseudoscalar-meson modes are decoupled to each other. Hence, the mesonic polarization function matrix Γ_{ij} does not have any off-diagonal elements. Then it is written in the momentum space as

$$\Gamma_{ii}(p) \propto \Pi_i \left(p^2 + M_i^2\right), \tag{4.24}$$

where the M_i are the meson masses. Here we take the pole approximation [30] that neglects the imaginary part of Γ_{ij}, that is the scattering phase shift of quark-antiquark scattering in the interaction channel. Since we are interested in temperature lower than the critical one, and in the normal phase, the pole approximation works well. In this approximation, the thermodynamic potential can be obtained by a sum of four quasiparticles, σ, π^0, π^+, and π^-:

$$\Omega^{\rm df} = \Omega^{\rm mf} + \sum_j \int \frac{d^3\mathbf{p}}{(2\pi)^3}\left[\frac{1}{2}(E_j - \mu_j) + \frac{1}{\beta}\ln\left(1 + e^{-\beta(E_j-\mu_j)}\right)\right] \tag{4.25}$$

with the meson energies $E_j = \sqrt{\mathbf{p}^2 + M_j^2}$ and the meson chemical potentials μ_j. In the full theory, the mesons cannot carry the chemical potentials and then $\mu_j = 0$ for all the mesons. In the phase-quenched theory where the chemical potential corresponds to the isospin chemical potential, the $\pi^\pm$ mesons carry the chemical potentials and then $\mu_{\pi^+} = 2\mu_{\rm q}$, $\mu_{\pi^-} = -2\mu_{\rm q}$ and $\mu_\sigma = \mu_{\pi^0} = 0$. Here

the meson masses M_j are calculated at zero chemical potential. Combined with the static fluctuations of the gauge fields, $\phi = (\phi_3,\ \phi_8)$, the partition function with the mesonic dynamical fluctuations becomes

$$Z^{\rm df} = \frac{1}{\mathcal{N}^{\rm df}} \exp\left(-\beta V \tilde{\Omega}^{\rm df}\right), \tag{4.26}$$

with

$$\tilde{\Omega}^{\rm df} = \Omega^{\rm df} + \frac{1}{2}\left(\frac{\delta^2\Omega^{\rm mf}}{\delta\phi_8^2}\right)^{-1}\left(\frac{\delta\Omega^{\rm mf}}{\delta\phi_8}\right)^2, \quad \mathcal{N}^{\rm df} = \left(\frac{\beta V}{2\pi}\right)\det\left(\frac{\delta^2\Omega^{\rm mf}}{\delta\phi_i\delta\phi_j}\right)^{1/2}. \tag{4.27}$$

The average phase factor with the dynamical fluctuations (DF) is then obtained by

$$\left\langle e^{2i\theta}\right\rangle = \frac{\mathcal{N}^{\rm df}_{\rm pq}}{\mathcal{N}^{\rm df}_{\rm full}} \exp\left[-\beta V\left(\tilde{\Omega}^{\rm df}_{\rm full} - \tilde{\Omega}^{\rm df}_{\rm pq}\right)\right]. \tag{4.28}$$

Even when the pion condensate does not occur in the phase-quenches theory, the thermodynamic potentials of the full and phase-quenched theories differ from each other in the MF+DF level due to the existence of the mesonic fluctuations. The static fluctuations correspond to the dynamical ones with only zero momentum since the static fluctuations are constant in the space and time. The MF+SF calculation is thus an approximation of the MF+DF one.

4.6 Numerical Results

4.6.1 The Polyakov loop and its conjugate

As mentioned in Sec. 4.2, there are two methods for taking the MF approximation in the PNJL model. In the method I), the expectation values of the Polyakov loop $\langle\Phi\rangle$ and its conjugate $\langle\Phi^*\rangle$ coincide with each other in the MF level because of the constraint of the gauge field $\langle\phi_8\rangle = 0$. Meanwhile, in the method II), the two expectation values are split out each other in the MF level at $\mu_{\rm q} \neq 0$. It is important to compare the difference between the MF approximations. Figure 4.1 shows T dependence of $\langle\Phi\rangle$ and $\langle\Phi^*\rangle$ at (a) $\mu_{\rm q} = 100$MeV and (b) $\mu_{\rm q} = 200$MeV.

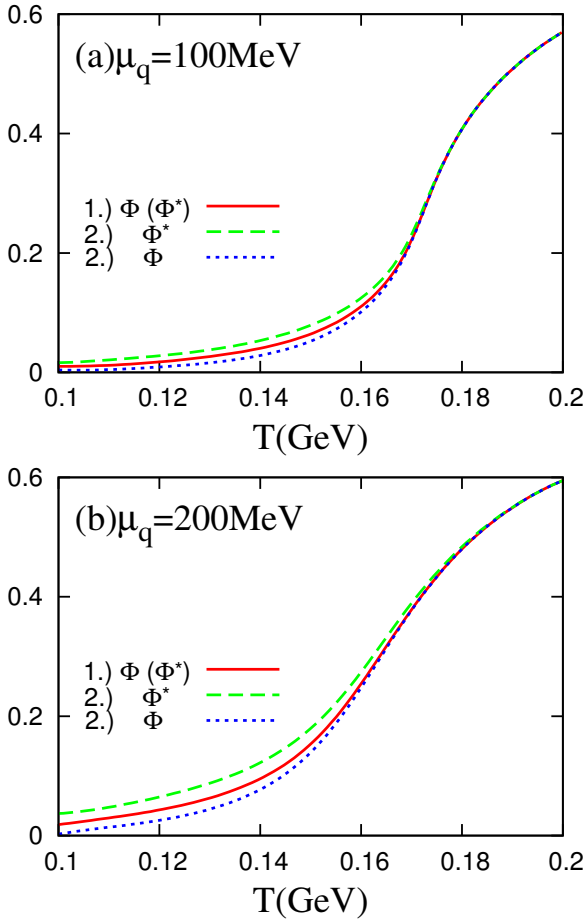

Figure 4.1: T dependence of the Polyakov loop Φ and its conjugate Φ^* in two kinds of MF approximations at (a) $\mu_{\rm q} = 100$MeV and (b) $\mu_{\rm q} = 200$MeV.

The result of the method I) is shown by the solid lines, where $\Phi = \Phi^*$. The results of the method II) are shown by dashed and dotted lines for $\langle\Phi^*\rangle$ and $\langle\Phi\rangle$, respectively. Comparing these three lines, we can see that the difference between the MF approximations is small. As shown in Ref. [25], the difference between the two MF approximations is improved by considering the static fluctuations, (4.21) and (4.22) in the method I). The splitting between $\langle\Phi\rangle$ and $\langle\Phi^*\rangle$ is caused by the corrections from the imaginary part of the potential induced by the gauge field ϕ_8. Thus the difference $\langle\Phi^*\rangle - \langle\Phi\rangle$ is naively related to the imaginary part of the potential, that is, the severeness of the sign problem. Figure 4.2 shows the difference $\langle\Phi^*\rangle^{\rm mf} - \langle\Phi\rangle^{\rm mf}$ in the T-$\mu_{\rm q}$ plane, where the method II) is considered in the MF level. The difference vanishes at zero chemical potential or large temperature. The difference increases with $\mu_{\rm q}$ for small T.

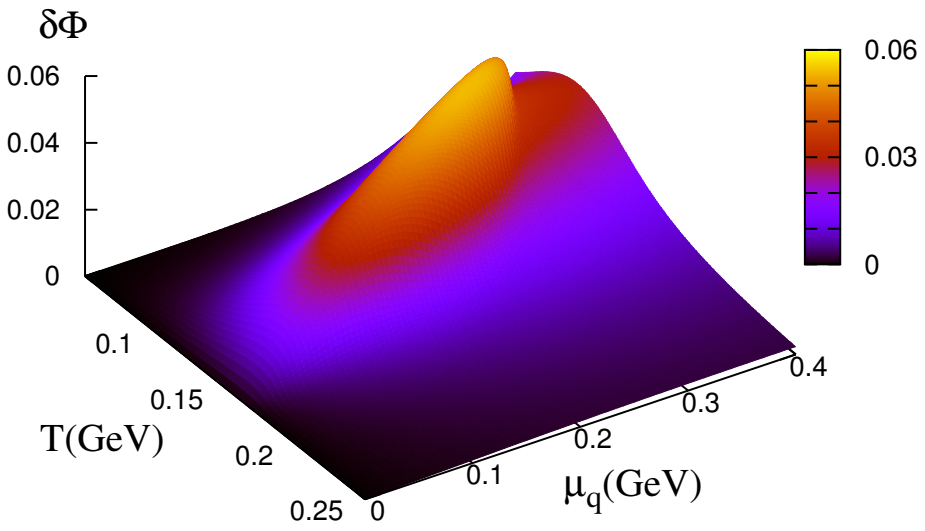

Figure 4.2: The difference between the Polyakov loop and its conjugate $\langle\Phi^* - \Phi\rangle^{\rm mf}$ in the $\mu_{\rm q}$-T plane.

4.6.2 Average Phase Factor

The average phase factor $\langle e^{2i\theta} \rangle$ is a good indicator for the severeness of the sign problem. As shown in (4.15), (4.19) and (4.28), the average phase factor depends on the volume βV. Here we take the condition, $L = 4\beta$, where L and β are the spatial and temporal lengths, respectively, in the PNJL calculation. Thus the volume $\beta V = 64\beta^4$ is controlled by β. This condition agrees with the condition where many LQCD calculations have. Although the average phase factor seems to depend on the volume, the volume dependence appears only when the thermodynamic potential in the phase-quenched theory differs from that in the full theory, $\Omega_{\rm full} \neq \Omega_{\rm pq}$, where the pion condensate occurs. When the pion condensate occurs, meanwhile, the average phase factor is almost zero. The average phase factor is thus dominated by the prefactor $\mathcal{N}_{\rm pq}/\mathcal{N}_{\rm full}$ in (4.19) and (4.28), and the following results little depend on the value. Figure 4.3 shows $\mu_{\rm q}$ dependence of the average phase factor at $T = 0.9T_{\rm c}$, $T_{\rm c}$, and $1.1T_{\rm c}$, where $T_{\rm c}$ is the deconfinement transition temperature at zero chemical potential and $T_{\rm c} = 173$MeV in the present calculation. The red, green and blue lines are results of the MF, MF+SF and MF+DF approximations, respectively. The results at $T = 0.9T_{\rm c}$ and $T_{\rm c}$ are almost the same. The average phase factor at $T = 1.1T_{\rm c}$ is larger than those at lower T. Therefore the average phase factor does not depend on T below $T_{\rm c}$, while it increases with T above $T_{\rm c}$. In the MF and MF+SF calculations, the average phase factor has an unphysical singularity at $\mu_{\rm q} = M_\pi/2$ where M_π is the pion mass at vacuum, but it smoothly tends to zero in the MF+DF calculation. Furthermore the effects of the fluctuations suppress the average phase factor at both lower and higher temperatures.

4.6.3 Comparison to the LQCD results

The average phase factor was calculated with LQCD [31] where the lattice size is $16^3 \times 4$ and the pion mass at vacuum is $M_\pi^{\rm LQCD} \approx 280$MeV. In the PNJL calculation, we have varied the quark mass from $m_0 = 5.5$MeV to 22.5MeV to reproduce $M_\pi^{\rm LQCD} = 280$MeV. For this value of m_0, the deconfinement transition temperature becomes a bit higher value, i.e., $T_{\rm c} = 180$MeV. Figure 4.4 shows $\mu_{\rm q}$ dependence of the average phase factor at $T = 0.9T_{\rm c}$, $T_{\rm c}$ and $1.25T_{\rm c}$. The

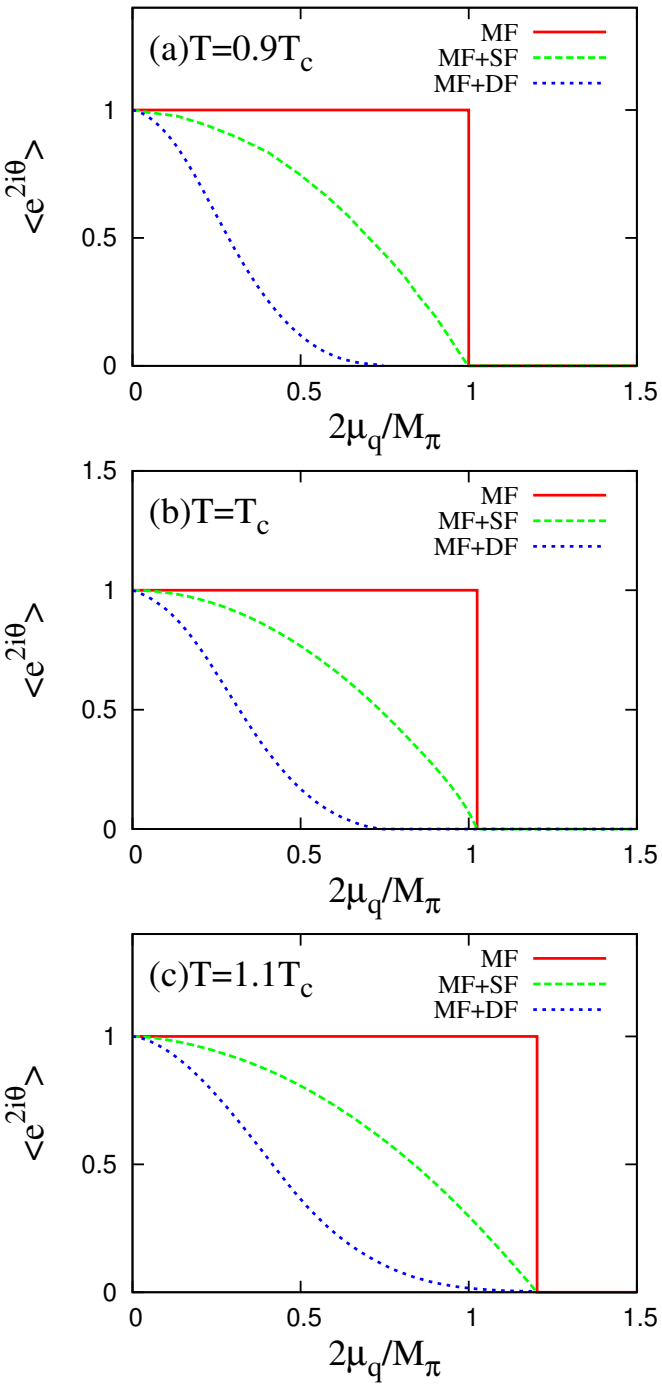

Figure 4.3: The average phase factor $\langle e^{2i\theta} \rangle$ as a function of μ_{q} at (a)$T = 0.9T_{\mathrm{c}}$, (b)T_{c}, and (c)$1.1T_{\mathrm{c}}$. The red, green, and blue lines represent results of the MF, MF+SF, and MF+DF approximations, respectively.

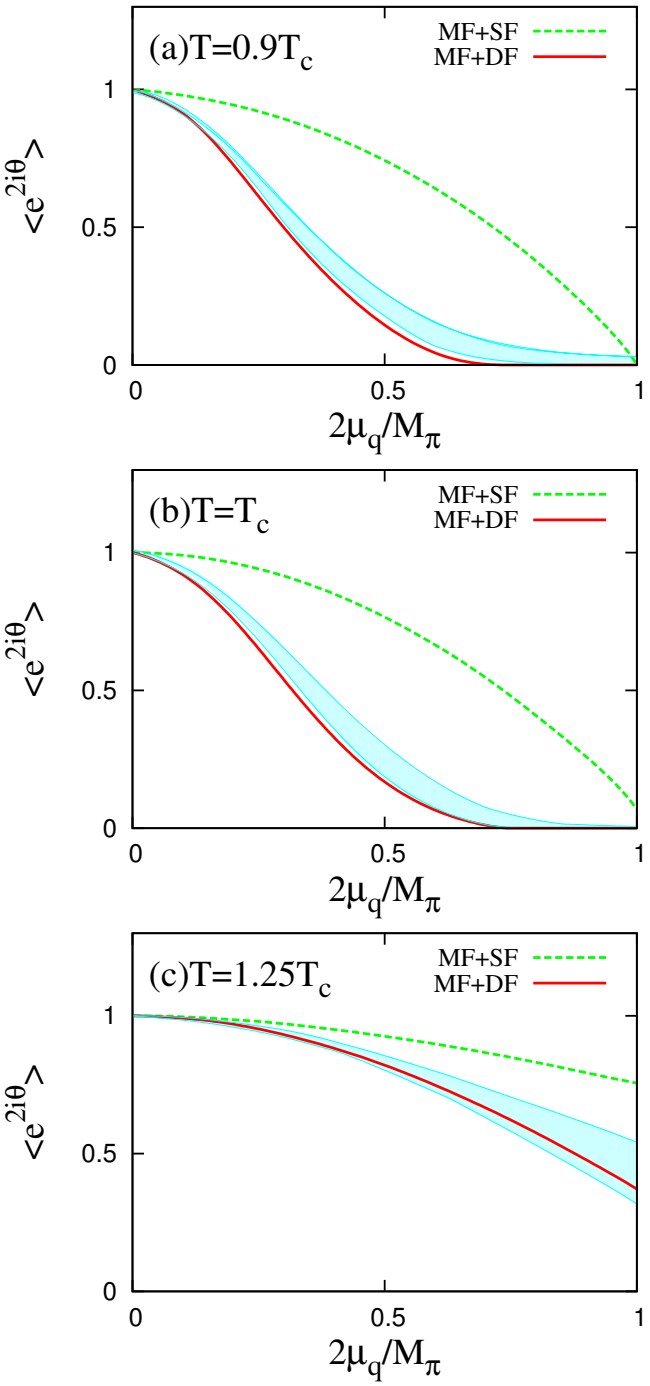

Figure 4.4: Comparison of the PNJL results in MF+DF calculations to the LQCD results at (a) $T = 0.9T_c$, (b) T_c and (c) $1.25T_c$. In each panel, the hatched region represents the LQCD prediction [31].

LQCD results are evaluated from analytic continuation of LQCD data at imaginary chemical potential by assuming a polynomial function. The hatched regions represent the LQCD results with the 90% confidence level for the extrapolation. The greed and red lines represent results of the MF+SF and MF+DF calculations, respectively. The MF+DF calculation almost reproduces the LQCD data as a consequence of the strong suppression by the mesonic fluctuations. Meanwhile, the MF+SF calculation underestimates the suppression due to not including the mesonic fluctuations with finite momentum. Below T_c, the pion mass is almost constant as shown in Fig. 3.3, so that the average phase factor little change with T because the pion modes are dominant in the fluctuations. Above T_c, the pion mass increases with T. The increase of the pion mass suppresses the pion fluctuation effects, so that the average phase factor becomes larger than that below T_c. As a consequence of the suppression of the mesonic fluctuations, the average phase factor in the MF+DF calculation is enhanced and approaches that in the MF+SF calculation.

4.6.4 The average phase factor in the μ_q-T plane

The full plot of the average phase factor in the μ_q-T plane is given in figure 4.5. In this figure, the average phase factor is calculated in the MF+SF calculation. The sign problem is exponentially bad in the pion condensate phase in the phase-quenched theory. Before reaching this region, the average phase factor is dominated by the mesonic fluctuations and it drops smoothly from one to zero. The critical end point (CEP) of the first-order chiral phase transition is plotted as a plus (+) for the PNJL model. The CEP and the first-order phase transition are in the $\langle e^{2i\theta} \rangle = 0$ region. This implies that the location of the CEP cannot be determined by LQCD directly.

4.6.5 Relation of the phase factor to the Polyakov loop

Figure 4.6 shows the relation of the average phase factor and the pion condensate to the Polyakov loop, varying T at $\mu_q = 100$MeV. Since Φ is an increasing function of T, the increase of Φ means that of T. The pion condensate π decreases as Φ increases and finally vanishes at a critical value Φ_c. Below Φ_c, the average phase

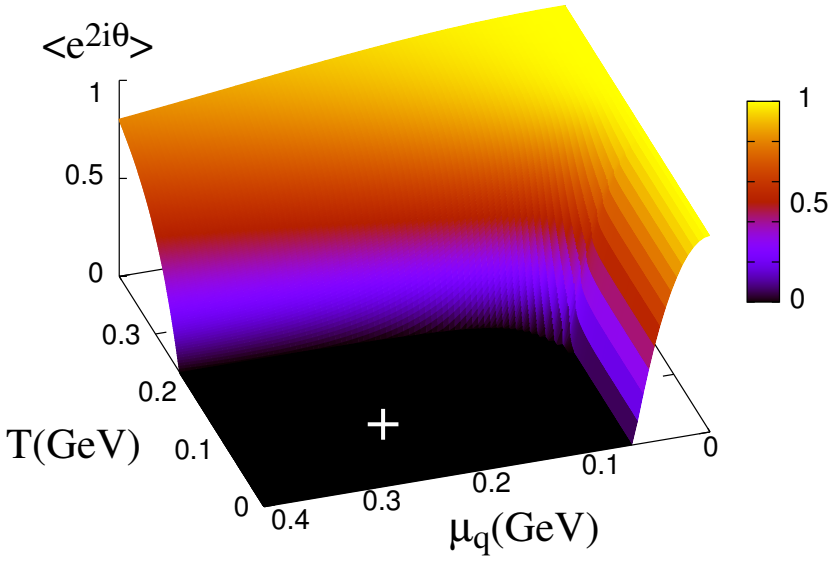

Figure 4.5: The average phase factor $\langle e^{2i\theta} \rangle$ in the μ_{q}-T plane.

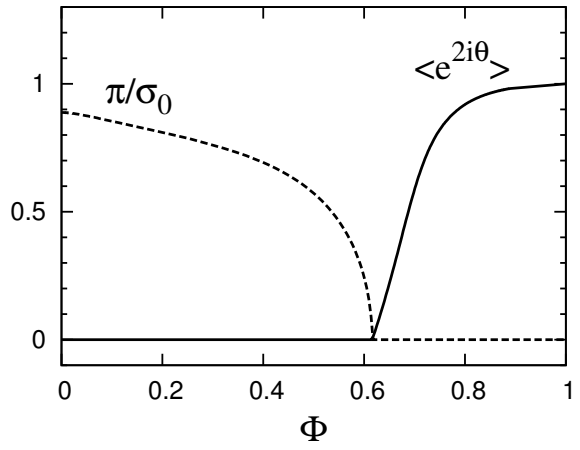

Figure 4.6: The Polyakov loop Φ dependence of the pion condensate π and the average phase factor $\langle e^{2i\theta} \rangle$ at $\mu_{\mathrm{q}} = 100$MeV. Here, the pion condensate is scaled by the chiral condensate at vacuum. The solid and dashed lines represent the pion condensate and average phase factor, respectively.

factor is always zero, while π is finite. Above Φ_c, inversely, the average phase factor is finite, while π is always zero. Thus, there is a negative correlation between the average phase factor and the pion condensate. In contrast, there exists a positive correlation between the average phase factor and the Polyakov loop; the average phase factor is zero at small Φ such as $\Phi < \Phi_c$, but at large Φ such as $\Phi > \Phi_c$ the average phase factor is finite and an increasing function of Φ. In the $\Phi = 1$ limit, the average phase factor tends to 1.

4.7 Summary

We have investigated the sign problem by using the PNJL model. The integrand of the partition function with finite chemical potential μ_q oscillates hardly, so that the importance sampling breaks down. The sign problem appears even in the mean field (MF) approximation. The MF approximation is not defined uniquely, actually the two types of the MF approximations are possible in the PNJL model. The difference between the two MF approximations mainly appears at the expectation value of the Polyakov loop. The difference is however tiny and the two MF approximations give qualitatively same results. The phase factor of the partition function is a good indicator for the severeness of the sign problem. We have evaluated the average phase factor by using the PNJL model. We have calculated the average phase factor in three type of approximations: the MF, the MF with the static fluctuations (MF+SF), and the MF with the dynamical mesonic fluctuations (MF+DF). The MF+DF calculation reproduces the lattice QCD (LQCD) result for the average phase factor. The average phase factor is dominated by the mesonic fluctuations in the MF+DF calculation. The fluctuation with the massless mode makes the sign problem worst when the pion condensate takes place in the phase-quenched theory. The worst region is the region of μ_q bigger than half the pion mass. The critical end point (CEP) exists in the worst region in the present calculation. This implies that the location of the CEP cannot be determined by LQCD directly. In the next chapter, we propose one possibility to approach the finite μ_q region and even the CEP. This approach is based on the first-principle LQCD and the PNJL model.

Chapter 5

Imaginary Chemical Potential

Lattice QCD (LQCD) has the sign problem at real quark chemical potential $\mu_{\rm q}$, but not at imaginary $\mu_{\rm q}$. This brings up the possibility of studying QCD at real $\mu_{\rm q}$ by analytic continuation of LQCD data from imaginary $\mu_{\rm q}$. In this chapter, we review properties of QCD at imaginary $\mu_{\rm q}$. We point out importance of the imaginary $\mu_{\rm q}$ region to check the reliability of effective models. We show that the PNJL model reproduces LQCD data qualitatively at imaginary $\mu_{\rm q}$. This chapter is mainly based on our papers [32].

5.1 Relation between real and imaginary $\mu_{\rm q}$

The QCD partition function Z has charge-conjugate symmetry: $\mu_{\rm q} \to -\mu_{\rm q}$, then Z is a function of $\mu_{\rm q}^2$. The real and imaginary $\mu_{\rm q}$ regions correspond to the regions with $\mu_{\rm q}^2 > 0$ and $\mu_{\rm q}^2 < 0$, respectively. The LQCD results show the derivatives of Z with respect to $\mu_{\rm q}^2$ have no singularity at $\mu_{\rm q}^2 = 0$. Therefore we can make an analytic continuation of LQCD data from imaginary $\mu_{\rm q}$ to real $\mu_{\rm q}$. So far LQCD has provided some observables such as the transition line at imaginary $\mu_{\rm q}$ [34; 35; 36; 37]. The observables $\mathcal{O}$ are transformed into the real $\mu_{\rm q}$ region by a polynomial function

$$\mathcal{O}(\mu_{\rm q}^2) = \sum_n c_n \mu_{\rm q}^{2n}, \tag{5.1}$$

where the coefficients c_n are fitted to reproduce the LQCD data at imaginary $\mu_{\rm q}$. Furthermore the partition function with imaginary $\mu_{\rm q}$ has a mathematically definite relation to that with real $\mu_{\rm q}$. The canonical partition function $Z_{\rm C}(N_{\rm q})$ with real quark-number $N_{\rm q}$ is the Fourier transform of the grand-canonical one $Z_{\rm GC}(\theta_{\rm q})$ with imaginary $\mu_{\rm q} = i\theta_{\rm q}/\beta$ [33],

$$Z_{\rm C}(N_{\rm q}) = {\rm Tr}\left(e^{-\beta\hat{H}}\delta(\hat{n}_{\rm q} - N_{\rm q})\right) = \int_0^{2\pi} \frac{d\theta_{\rm q}}{2\pi} e^{-i\theta_{\rm q}N_{\rm q}} Z_{\rm GC}(\theta_{\rm q}). \tag{5.2}$$

Thus, the partition function at imaginary $\mu_{\rm q}$ includes all dynamics at real $N_{\rm q}$ and hence at real $\mu_{\rm q}$. Figure 5.1 shows a schematic picture of the phase diagram in both the real and imaginary $\mu_{\rm q}$ regions. The $\mu_{\rm q}^2 > 0$ and $\mu_{\rm q}^2 < 0$ regions correspond to the real and imaginary $\mu_{\rm q}$ regions. The crossover transition line continues smoothly from imaginary $\mu_{\rm q}$ to real $\mu_{\rm q}$. This makes it possible to make the analytic continuation of $\mathcal{O}$ from imaginary $\mu_{\rm q}$ to real $\mu_{\rm q}$. Moreover the thermodynamics at real $\mu_{\rm q}$ is obtained directly through the Fourier transformation from imaginary $\mu_{\rm q}$.

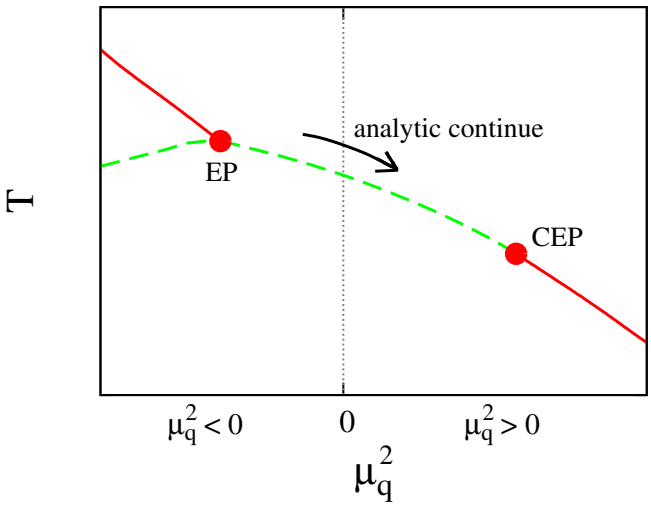

Figure 5.1: Schematic picture of the QCD phase diagram in the $\mu_{\rm q}^2$-T plane. The $\mu_{\rm q}^2 < 0$ and $\mu_{\rm q}^2 > 0$ regions corresponds to the imaginary and real $\mu_{\rm q}$ regions, respectively. The solid (dashed) line represents the first-order (crossover) transition line. CEP and EP are the end points of the first-order transition lines at real and imaginary $\mu_{\rm q}$, respectively.

5.2 Purpose

The first-principle LQCD simulations have become feasible for thermal systems at zero μ_q [38; 39]. As for real μ_q, however, LQCD has the sign problem and hence the results are still far from perfection. Several approaches have been proposed to circumvent the difficulty. One approach is the analytic continuation from imaginary μ_q to real μ_q. When physical quantities are available with LQCD at imaginary μ_q, we can extrapolate them to real μ_q, until there appears a discontinuity. Actually, such an extrapolation was made for the phase transition curve by assuming some analytic functions for the curve [34; 35; 36; 37]. This direct extrapolation may work for small real μ_q, but its accuracy is quite unknown for large real μ_q. This problem may be circumvented by the effective model that can evaluate the partition function at both real and imaginary μ_q and reproduce results of LQCD at imaginary μ_q, if such an effective theory is found. The imaginary μ_q region is thus a good test ground of the model reliability. So far many effective models have been proposed as an approach complementary to LQCD simulations. Figure 5.2 summarizes the model predictions for the location of the critical endpoint of the chiral phase transition at real μ_q [40]. The results spread out very widely despite of the fact that the inputs are almost the same in all the models. In each calculation, the parameters are determined from the physical quantities, e.g., the pion mass and the decay constant, at $T = \mu_q = 0$[1]. Nevertheless, the extrapolation to finite μ_q is not unique. It is then highly nontrivial whether the models predict properly physical quantities at finite μ_q. This should be tested directly from QCD. Fortunately, this is possible at imaginary μ_q, since LQCD is feasible there. Furthermore as shown in (5.2), in principle the partition function at imaginary μ_q includes all dynamics at real μ_q through the Fourier transformation. If an effective model is successful in reproducing LQCD results at imaginary μ_q, this implies not only that the model is reliable for both the real and imaginary μ_q regions but also that the LQCD results can be reasonably extrapolated to the real μ_q region by using the model. In order to proceed this strategy, we have to construct an effective model that reproduces

[1] In the PNJL model, the LQCD data in the pure gauge at $T \neq 0$ is also used as the input parameters. However the input includes no μ_q-information.

LQCD results at imaginary $\mu_{\rm q}$. The PNJL model is a good candidate. We review properties of QCD at imaginary $\mu_{\rm q}$ and show that the PNJL model reproduces them qualitatively.

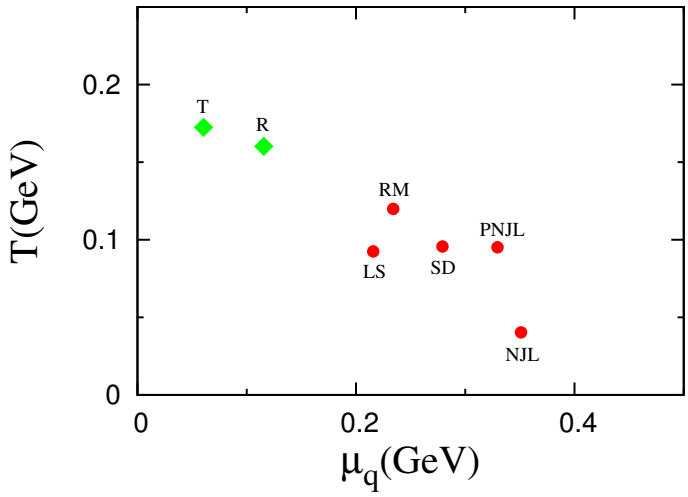

Figure 5.2: Predictions for location of the critical endpoint [40]. Red points are predictions of the NJL [41], the PNJL [25], the linear sigma (LS) [43], the random matrix (RM) models [42] and the Schwinger-Dyson calculation (SD) [44]. Green points are LQCD predictions based on the Taylor expansion (T) [45] and the reweighting (R) [46] methods.

5.3 Roberge-Weiss periodicity

Symmetries are essential to understand QCD. Here we show an important symmetry at imaginary $\mu_{\rm q}$ [33], which governs the $\mu_{\rm q}$ dependence of the quantities there. We start with the QCD partition function Z at imaginary $\mu_{\rm q} = i\theta_{\rm q}/\beta$ for real $\theta_{\rm q}$,

$$Z(\theta_{\rm q}) = {\rm Tr}\left(e^{-\beta\hat{H}+i\theta_{\rm q}\hat{N}_{\rm q}}\right) = \int \mathcal{D}X \exp\left(-\int d^4x \left[\bar{q}(\gamma D - \frac{i\theta_{\rm q}}{\beta}\gamma_4)q + \frac{1}{4g^2}F^2\right]\right), \quad (5.3)$$

where $\hat{H}$ and $\hat{N}_{\rm q}$ are the Hamiltonian and the quark-number operator, respectively, and $\mathcal{D}X = \mathcal{D}\bar{q}\mathcal{D}q\mathcal{D}A$. It is clear from (5.3) that $Z(\theta_{\rm q})$ has a periodicity

2π for quarks and $2\pi/3$ for color-singlet hadrons where $N_{\rm q} = 0 \mod 3$. The periodicity of $Z(\theta_{\rm q})$ is thus related to the confinement of quarks. In other words, since the effect of the imaginary $\mu_{\rm q}$ is the same as a temporal Abelian gauge field coupled to the quark-number, a baryon with the quark-number 3 picks up a phase $\exp(-3i\theta_{\rm q})$ when it runs around the temporal cylinder $\tau \in [0, \beta]$. Thus the physics is unchanged when $\theta_{\rm q} \to \theta_{\rm q} + 2\pi/3$ and $Z(\theta_{\rm q})$ has periodicity $2\pi/3$. Similarly, we can consider that the system with quarks has periodicity 2π. This statement is, however, too naive. The point is that the $\mathbb{Z}_3$ symmetry of the action implies that $Z(\theta_{\rm q})$ must have a periodicity $2\pi/3$. To see this we note that the $\theta_{\rm q}$ dependence of the partition function can be eliminated from the action and transferred to the boundary conditions via the change of variables, $q \to e^{i\tau\theta/\beta}q$:

$$Z(\theta_{\rm q}) = \int \mathcal{D}X \exp\left(-\int d^4x \left[\bar{q}\gamma Dq + \frac{1}{4g^2}F^2\right]\right), \tag{5.4}$$

with the boundary condition, $q(\beta) = -e^{i\theta_{\rm q}}q(0)$. The periodicity of $Z(\theta_{\rm q})$ is proven by performing the $\mathbb{Z}_3$ transformation,

$$q \to Uq, \quad A_\nu \to U\left[A_\nu + i\partial_\nu\right]U^{-1}, \tag{5.5}$$

where $U(x,\tau)$ are center elements of $SU(3)$ with the boundary condition $U(x,\beta) = e^{2\pi ik/3}U(x,0)$ for integer k. Under this transformation, the partition function $Z(\theta_{\rm q})$ is invariant, but the boundary condition is changed into $q(\beta) = -e^{i(\theta_{\rm q}-2\pi k/3)}q(0)$. We thus conclude that

$$Z(\theta_{\rm q}) = Z(\theta_{\rm q} + 2\pi k/3), \qquad k \in \mathbb{Z}. \tag{5.6}$$

This periodicity is called the Roberge-Weiss (RW) periodicity [33]. This means that QCD is invariant under a combination of the $\mathbb{Z}_3$ transformation and $\theta_{\rm q} \to \theta_{\rm q} + 2\pi k/3$. This combination is called the extended $\mathbb{Z}_3$ transformation. Thus, the QCD partition function has the extended $\mathbb{Z}_3$ symmetry. The extended $\mathbb{Z}_3$ symmetry appears as the RW periodicity at imaginary $\mu_{\rm q}$, and the periodicity governs the dynamics there as shown later.

5.4 Roberge-Weiss transition

Although the QCD partition function has the periodicity $2\pi/3$ in both the confinement and the deconfinement phases, there is the difference between the two phases in its $\theta_{\rm q}$ dependence. This was studied by evaluating the thermodynamic potential $\Omega(\theta_{\rm q}) = -\frac{T}{V}\ln\left[Z(\theta_{\rm q})\right]$ for the two phases [33]. In the confinement phase, the potential is described only by hadrons, thus it seems to be an analytic function of $3\theta_{\rm q}$. This is ensured by evaluating the potential in the strong-coupling limit. In the deconfinement phase, the potential is evaluated perturbatively. The one-loop potential for $N_{\rm f}$ massless flavors at imaginary $\mu_{\rm q} = i\theta_{\rm q}/\beta$ is obtained as

$$\Omega^{(1)}(\theta_{\rm q}) = -2N_{\rm f}\frac{1}{\beta}\sum_j \int \frac{d^3\mathbf{p}}{(2\pi)^3}\left[\ln(1-e^{-\beta\mathbf{p}+i(\theta_{\rm q}-\bar{\phi}_j)}) + \ln(1-e^{-\beta\mathbf{p}-i(\theta_{\rm q}-\bar{\phi}_j)})\right] \quad (5.7)$$

in the Polyakov gauge. The temporal gauge field $\bar{\phi}_j$ satisfies the condition $\sum_j \bar{\phi}_j = 0 \mod 2\pi$. After integrating the momentum out, we can arrive at the one-loop potential with $\theta_{\rm q}$:

$$\Omega^{(1)}(\theta_{\rm q}) = -\frac{\pi^2}{12}N_{\rm f}T^4\sum_j\left[1-\left\{\left(\frac{\theta_{\rm q}-\bar{\phi}_j}{\pi}-1\right)_{\mod 2}-1\right\}^2\right]^2. \quad (5.8)$$

In addition of this quark potential, there is a gluonic potential with the $\mathbb{Z}_3$ symmetry. The gluonic potential has equivalent minima whenever all the ϕ_j are equal to each other and $\bar{\phi}_j = 2\pi k/3$ for integer k. In the presence of quarks, the $\mathbb{Z}_3$ symmetry is explicitly broken, thus only one state in the $\mathbb{Z}_3$ symmetric ones is chosen as a global minimum. For $\theta_{\rm q} = 0$, the potential has a global minimum at $\bar{\phi}_j = 0$ and local minima at the $\mathbb{Z}_3$ images. The location of this global minimum is unchanged for small $\theta_{\rm q}$. For $\theta_{\rm q} = 2\pi k/3$, the global minimum is no longer at $\bar{\phi}_j = 0$, thus it has moved to $\bar{\phi}_j = -2\pi k/3$ since the quark potential $\Omega^{(1)}(\theta_{\rm q})$ depends only on the sum, $\bar{\phi}_j + \theta_{\rm q}$. Figure 5.3 shows $\theta_{\rm q}$ dependence of $\Omega_f(\theta)$ for $\phi_j = 2\pi k/3$. The $\theta_{\rm q}$ dependence of the thermodynamic potential at vacuum is chosen as the curve with the smallest value of $\Omega^{(1)}(\theta)$ at each $\theta_{\rm q}$. The potential is discontinuous as a function of $\theta_{\rm q}$ with a cusp at $\theta_{\rm q} = (2k+1)\pi/3$. This implies that a first-order phase transition occurs there in the deconfinement phase. This

phase transition is called the Roberge-Weiss (RW) transition [33]. Each phase is classified by the expectation value of the gauge field ϕ.

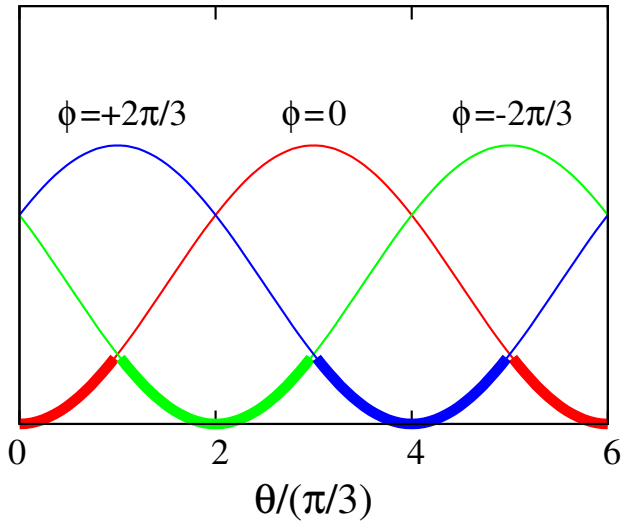

Figure 5.3: $\theta_{\rm q}$ dependence of the one-loop potential $\Omega^{(1)}$ with $\bar{\phi}_j = 2\pi k/3$. The red, green, and blue lines represent the $k = 0,\ 1$ and -1 cases, respectively. The potential at vacuum shows the bold line.

5.5 The PNJL model at imaginary $\mu_{\rm q}$

The RW periodicity and the RW phase transition are important properties of QCD at imaginary $\mu_{\rm q}$. These properties appear as a result of the fact that the QCD partition function has the extended $\mathbb{Z}_3$ symmetry. In this section, we show that the PNJL model has the extended $\mathbb{Z}_3$ symmetry and then reproduces both the RW periodicity and the RW phase transition. The model reproduces the first-principle LQCD results qualitatively. The model is thus suitable for investigating the phase structure at imaginary $\mu_{\rm q}$.

5.5.1 Extended $\mathbb{Z}_3$ symmetry

First we show that the PNJL model has the extended $\mathbb{Z}_3$ symmetry. The thermodynamic potential $\Omega_{\rm PNJL}$ in the mean field (MF) approximation at imaginary

$\mu_{\rm q} = i\theta_{\rm q}/\beta$ is obtained as

$$\Omega_{\rm PNJL} = -2N_{\rm f}\int\frac{d^3\mathbf{p}}{(2\pi)^3}\left[3E_{\rm q} + \frac{1}{\beta}\left\{\ln\mathcal{F}_{\rm q}(\theta_{\rm q}) + \ln\mathcal{F}_{\bar{\rm q}}(\theta_{\rm q})\right\}\right] + G_{\rm s}\sigma^2 + U_\Phi, \tag{5.9}$$

with

$$\mathcal{F}_{\rm q}(\theta_{\rm q}) = 1 + 3\Phi e^{-\beta E_{\rm q}+i\theta_{\rm q}} + 3\Phi^* e^{-2\beta E_{\rm q}+2i\theta_{\rm q}} + e^{-3\beta E_{\rm q}+3i\theta_{\rm q}}, \tag{5.10}$$

$$\mathcal{F}_{\bar{\rm q}}(\theta_{\rm q}) = 1 + 3\Phi^* e^{-\beta E_{\rm q}-i\theta_{\rm q}} + 3\Phi e^{-2\beta E_{\rm q}-2i\theta_{\rm q}} + e^{-3\beta E_{\rm q}-3i\theta_{\rm q}}. \tag{5.11}$$

For real $\mu_{\rm q}$, the expectation values of the Polyakov loop Φ and its conjugate Φ^* are real and differ from each other as shown in Chapter 4. For imaginary $\mu_{\rm q}$, however, the expectation values are complex conjugate of each other since the statistical weight is real there. $\mathcal{F}_{\bar{\rm q}}$ is thus the complex conjugate of $\mathcal{F}_{\rm q}$. The Polyakov potential U_Φ is invariant under the $\mathbb{Z}_3$ transformation, $\Phi \to e^{-2\pi i/3}\Phi$, $\Phi^* \to e^{2\pi i/3}\Phi^*$, but the thermodynamic potential $\Omega_{\rm PNJL}$ is not invariant due to presence of the quark parts, $\mathcal{F}_{\rm q}$ and $\mathcal{F}_{\bar{\rm q}}$. Instead of the $\mathbb{Z}_3$ symmetry, however, $\Omega_{\rm PNJL}$ is invariant under the extended $\mathbb{Z}_3$ transformation,

$$\theta_{\rm q} \to \theta_{\rm q} + 2\pi/3, \quad \Phi \to e^{-2\pi i/3}\Phi, \quad \Phi^* \to e^{2\pi i/3}\Phi^*. \tag{5.12}$$

It is convenient to introduce the modified Polyakov loop $\Psi = e^{i\theta_{\rm q}}\Phi$ and $\Psi^* = e^{-i\theta_{\rm q}}\Phi^*$ which is invariant under the transformation (5.12). Using this quantities, $\mathcal{F}_{\rm q}$ is rewritten into

$$\mathcal{F}_{\rm q}(\theta_{\rm q}) = 1 + 3\Psi e^{-\beta E_{\rm q}} + 3\Psi^* e^{-2\beta E_{\rm q}+3i\theta_{\rm q}} + e^{-3\beta E_{\rm q}+3i\theta_{\rm q}}. \tag{5.13}$$

Obviously $\mathcal{F}_{\rm q}$ and the complex conjugate $\mathcal{F}_{\bar{\rm q}}$ are invariant under the extended $\mathbb{Z}_3$ transformation. Therefore Ω is also invariant under the transformation.

5.5.2 $\theta_{\rm q}$ reflection symmetry

In addition of the extended $\mathbb{Z}_3$ symmetry, charge-conjugation symmetry characterizes $\theta_{\rm q}$ dependence of physical quantities. Under charge-conjugation, $\theta_{\rm q} \to -\theta_{\rm q}$, the thermodynamic potential $\Omega_{\rm PNJL}$ is invariant, but the Polyakov loop and

its conjugate change as $\Phi \to \Phi^*$, $\Phi^* \to \Phi$. This indicates that $\Psi(-\theta_{\rm q}) = \Psi^*(\theta_{\rm q})$ and $\Psi^*(-\theta_{\rm q}) = \Psi(\theta_{\rm q})$. Therefore the real part, $\mathrm{Re}\,(\Psi) = (\Psi + \Psi^*)/2$, and the imaginary part, $\mathrm{Im}\,(\Psi) = (\Psi - \Psi^*)/2$, of the modified Polyakov loop are $\theta_{\rm q}$-even and -odd, respectively. Similarly, the absolute value $|\Psi|$ and the phase ψ are $\theta_{\rm q}$-even and -odd, respectively. Furthermore the chiral condensate $\sigma = \partial\Omega_{\rm PNJL}/\partial m_0$ and the quark-number density $\rho_{\rm q} = -\partial\Omega_{\rm PNJL}/\partial\mu_{\rm q} = i\beta(\partial\Omega_{\rm PNJL}/\partial\theta_{\rm q})$, which is pure imaginary, are $\theta_{\rm q}$-even and -odd, respectively. The $\theta_{\rm q}$-even $X(\theta_{\rm q})$ and the $\theta_{\rm q}$-odd quantities $Y(\theta_{\rm q})$ satisfy,

$$X(\pi/3 + \theta_{\rm q}) = X(\pi/3 - \theta_{\rm q}), \quad Y(\pi/3 + \theta_{\rm q}) = -Y(\pi/3 - \theta_{\rm q}). \tag{5.14}$$

These relations indicate that the $\theta_{\rm q}$-even (odd) quantities have cusps (jumps) at $\theta_{\rm q} = \pi/3$ when $\partial X/\partial\theta_{\rm q}$ (Y) are finite there. Such a singularity comes out in the high temperature region, as shown in Sec. IV with numerical calculations. This means that the RW phase transition at $\theta_{\rm q} = \pi/3$ is second-order for $\theta_{\rm q}$-even quantities and first-order for the $\theta_{\rm q}$-odd ones.

5.5.3 The potential at high or low T limit

Before proceeding to the numerical results, it is useful to explore properties of the thermodynamic potential in some limits. The modified Polyakov loops Ψ and Ψ^* are also invariant under a continuous transformation,

$$\theta_{\rm q} \to \theta_{\rm q} + \alpha, \quad \Phi \to e^{-i\alpha}\Phi, \quad \Phi^* \to e^{i\alpha}\Phi^*, \tag{5.15}$$

for any real parameter α. However, the thermodynamic potential $\Omega_{\rm PNJL}$ is not invariant owing to the existence of the factor $e^{\pm 3i\theta_{\rm q}}$. If $\Omega_{\rm PNJL}$ was invariant under the transformation (5.15), the continuous symmetry would lead to a simple relation $\Psi(\theta_{\rm q}+\alpha) = \Psi(\theta_{\rm q})$, that is, $\Phi(\theta_{\rm q}+\alpha) = e^{-i\alpha}\Phi(\theta_{\rm q})$. For low temperature: $\beta E_{\rm q} \ll 1$, the thermodynamic potential is reduced to

$$\Omega_{\rm PNJL} \sim \Omega_0 - 2N_{\rm f}\frac{1}{\beta}\int \frac{d^3\mathbf{p}}{(2\pi)^3} \ln\left(1 + 3\Psi e^{-\beta E_{\rm q}}\right)\left(1 + 3\Psi^* e^{-\beta E_{\rm q}}\right), \tag{5.16}$$

where Ω_0 is the potential at $T = \theta_q = 0$. This has no explicit θ_q dependence[1]. Therefore, at low temperature, $\Omega_{\rm PNJL}$ is approximately invariant under the transformation (5.15) and Φ can rotate smoothly as θ_q varies. At high temperature, however, effects of the explicit θ_q dependence are not negligible and hence $\Omega_{\rm PNJL}$ has no the approximate symmetry. It is thus obvious that the RW phase transition at high T originates in the factor $e^{\pm 3i\theta_q}$ of the potential. At high temperature, the continuous symmetry under the transformation (5.15) is broken into a discrete symmetry, i.e., the extended $\mathbb{Z}_3$ symmetry, through the factor $e^{\pm 3i\theta_q}$. In the limit of $\Phi = \Phi^* = 1$, that realizes high T, the quark part $\Omega^q_{\rm PNJL}$ of the potential (5.9) without the Polyakov potential U_Φ coincides with the potential $\Omega_{\rm NJL}$ of the NJL model,

$$\Omega^q_{\rm PNJL}(\Phi = \Phi^* = 1) = \Omega_{\rm NJL}. \tag{5.17}$$

In the limit of $\Phi = \Phi^* = 0$, that realizes low T, meanwhile,

$$\Omega_{\rm PNJL}(\Phi = \Phi^* = 0) = \frac{\Omega_{\rm NJL}(\theta_q) + \Omega_{\rm NJL}(\theta_q + 2\pi/3) + \Omega_{\rm NJL}(\theta_q - 2\pi/3)}{3}. \tag{5.18}$$

In this limit, the thermodynamic potential of the PNJL model coincides with the $\mathbb{Z}_3$ symmetrized potential of that of the NJL model. In the zero temperature limit, particularly, the potential of the PNJL model is reduced to that of the NJL model. Therefore, in both the high and the low temperature region, the PNJL and NJL models give similar results for the chiral symmetry. However, the difference between the two models is significant in the intermediate-temperature region. Actually, the PNJL model shifts the critical endpoint to higher T and lower μ_q at real μ_q.

[1] The partition function $Z_{\rm GC}(\theta_q)$ with a finite value of θ_q is equivalent to $Z_{\rm GC}(0)$ with the boundary condition $q(\beta) = -e^{i\theta_q} q(0)$ for the quark field q. In the low-T limit where a period β of the imaginary time becomes infinite, the value of $Z_{\rm GC}(\theta_q)$ does not depend on how to take the boundary condition and then has no θ_q dependence.

5.5.4 Comparison of the PNJL model to others

Many effective models have been proposed so far. The models have predicted different phase diagrams at real $\mu_{\rm q}$ as discussed in Sec. 5.2. Among the models, the PNJL model is only a effective model that describes the RW periodicity and the RW phase transition at imaginary $\mu_{\rm q}$. This implies that the PNJL model is most reliable at finite $\mu_{\rm q}$. The NJL model respects the chiral symmetry but it does not preserve the extended $\mathbb{Z}_3$ symmetry. On the contrary, the three-dimensional three-state Potts model respects the extended $\mathbb{Z}_3$ symmetry and then has the RW periodicity, but it does not possess the chiral symmetry since the model is a paradigm of QCD in the large quark-mass limit. In LQCD, the quark chemical potential $\mu_{\rm q}$ is introduced just like the fourth component of imaginary constant vector field, i.e., $e^{a\mu_{\rm q}}U_4$ or $e^{-a\mu_{\rm q}}U_4^\dagger$, where a and $U_4(=e^{-iaA_4})$ are the lattice spacing and the fourth component of the gauge field on the lattice, respectively. In this case, the RW periodicity is naturally satisfied. Thus the PNJL model has both the chiral and the extended $\mathbb{Z}_3$ symmetry, just as QCD.

5.6 $\theta_{\rm q}$ dependence of some quantities

In this section, we show that the PNJL model reproduces the LQCD results qualitatively. Most LQCD calculations have been done so far in the degenerated 4 flavor staggered fermions, but it does not matter for the qualitative comparison of the PNJL model with LQCD data, particularly for $\theta_{\rm q}$ or T dependences.

5.6.1 Thermodynamic potential

The thermodynamic potential is a most fundamental quantity to describe the thermodynamics. As shown in the previous section, the potential has the RW periodicity and it is $\theta_{\rm q}$-even. Figure 5.4 (a) shows the thermodynamic potential $\Omega_{\rm PNJL}$ of the PNJL model as a function of $\theta_{\rm q}$ in two cases of $T=T_{\rm c}$ and $1.1T_{\rm c}$ where $T_{\rm c}=173$ MeV is the critical temperature of the deconfinement transition at $\theta_{\rm q}=0$. The potential $\Omega_{\rm PNJL}$ is RW periodic and $\theta_{\rm q}$-even as expected. $\Omega_{\rm PNJL}$ is smooth everywhere for low temperature of $T=T_{\rm c}$, but it has a cusp at $\theta_{\rm q}=(2k+1)\pi/3$ for high temperature of $T=1.1T_{\rm c}$. This means that the first-order

RW phase transition occurs there. The critical temperature $T_{\rm RW}$ of the endpoint of the RW transition exists in $T_{\rm c} < T_{\rm RW} < 1.1T_{\rm c}$. Figure 5.4 (b) shows the corresponding LQCD result [34] for the same temperatures. The PNJL results are consistent with the LQCD ones for $\theta_{\rm q}$ and T dependences of the thermodynamic potential.

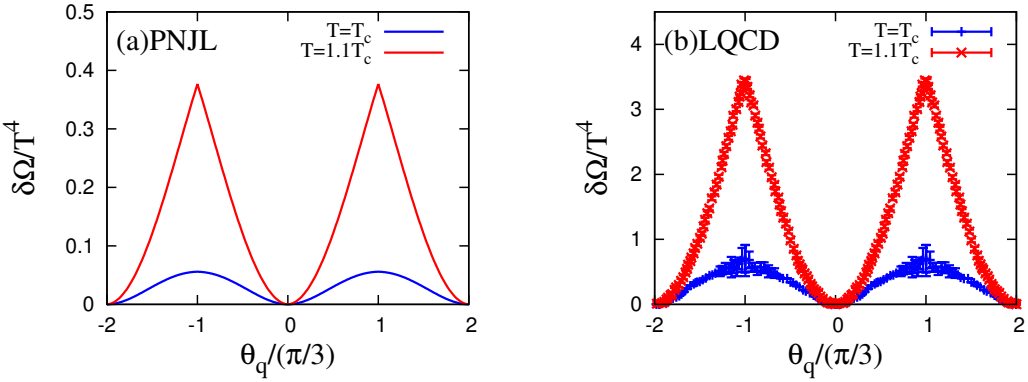

Figure 5.4: $\theta_{\rm q}$ dependence of the thermodynamic potential $\delta\Omega = \Omega(\theta_{\rm q}) - \Omega(\theta_{\rm q} = 0)$ in (a) the PNJL model and (b) LQCD [34]. The red (blue) line corresponds to the case of $T = T_{\rm c}$ ($1.1T_{\rm c}$).

5.6.2 Polyakov loop

The RW transition is a phase transition from one phase of the $\mathbb{Z}_3$ vacua to another. These phases are classified by the expectation value of the temporal gauge field, that is, the phase of the Polyakov loop. Figure 5.5 (a) and (b) show results of the PNJL model for the absolute value $|\Phi|$ and the phase ϕ of the Polyakov loop Φ at $T = T_{\rm c}$ and $1.1T_{\rm c}$, respectively. The Polyakov loop does not have the RW periodicity and it is changed as $\Phi \to e^{-2\pi i/3}\Phi$ and $\Phi^* \to e^{2\pi i/3}\Phi^*$ under the $\mathbb{Z}_3$ transformation, i.e., $\theta_{\rm q} \to \theta_{\rm q} + 2\pi/3$. The modified Polyakov loop $\Psi = e^{i\theta_{\rm q}}\Phi$ and its conjugate Ψ^* are introduced as the extended $\mathbb{Z}_3$ invariant quantities. The absolute value and the phase of Ψ are $\theta_{\rm q}$-even and -odd, respectively. The absolute value of the Polyakov loop is the same as that of the modified one, so that it is RW-periodic and $\theta_{\rm q}$-even as shown in panel (a). The phase ϕ of the Polyakov loop is related to that ψ of the modified Polyakov loop as $\psi = \phi + \theta_{\rm q}$. When $\theta_{\rm q}$

is changed as $\theta_q \to \theta_q + 2\pi/3$, the phase ϕ is changed as $\phi \to \phi - 2\pi/3$ because of the RW periodicity of ψ. The absolute value and the phase of the Polyakov loop are smooth everywhere for low temperature of $T = T_c$, but the former (latter) has a cusp (discontinuity) at $\theta_q = (2k+1)\pi/3$ for high temperature of $T = 1.1T_c$. These θ_q dependence is a consequence of the relation (5.14). The corresponding LQCD results [37] are shown in the panel (c) and (d). The PNJL results well reproduce the LQCD ones for θ_q and T dependences of the Polyakov loop.

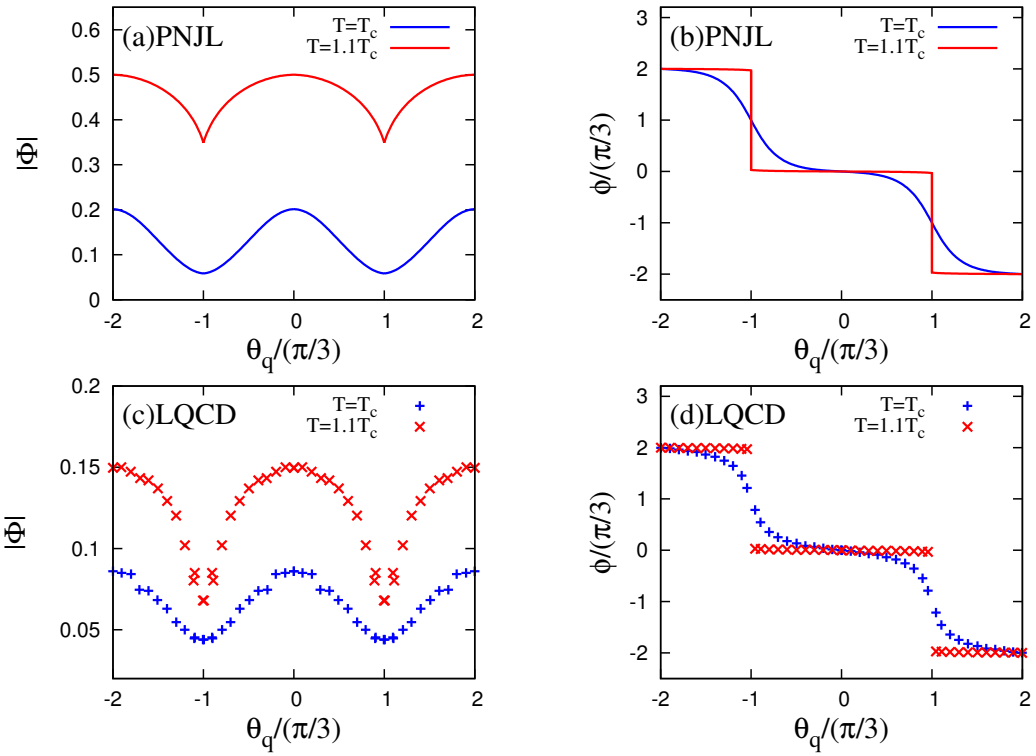

Figure 5.5: θ_q dependence of the Polyakov loop Φ. The panel (a) and (b) show the PNJL results for the absolute value $|\Phi|$ and the phase ϕ, respectively. The panel (c) and (d) does the LQCD results [37] for $|\Phi|$ and ϕ, respectively. The red (blue) line corresponds to the case of $T = T_c$ ($1.1T_c$).

5.6.3 Chiral condensate

The chiral condensate is an order parameter of the chiral phase transition. It is important to see how the chiral transition is affected by imaginary μ_q. Figure 5.6

shows the chiral condensate $\sigma = \partial\Omega_{\rm PNJL}/\partial m_0$ as a function of $\theta_{\rm q}$ at $T = T_{\rm c}$ and $1.1T_{\rm c}$. Panels (a) and (b) correspond to results of the PNJL model and LQCD [35], respectively. The chiral condensate has the RW periodicity and it is $\theta_{\rm q}$-even. The chiral condensate is smooth everywhere for low temperature of $T = T_{\rm c}$, but it has a cusp at $\theta_{\rm q} = (2k+1)\pi/3$ for high temperature of $T = 1.1T_{\rm c}$. The chiral condensate increases with $\theta_{\rm q}$. This means that the chiral phase transition moves to higher temperature as $\theta_{\rm q}$ increases. The PNJL results are consistent with LQCD ones for $\theta_{\rm q}$ and T dependences of the chiral condensate.

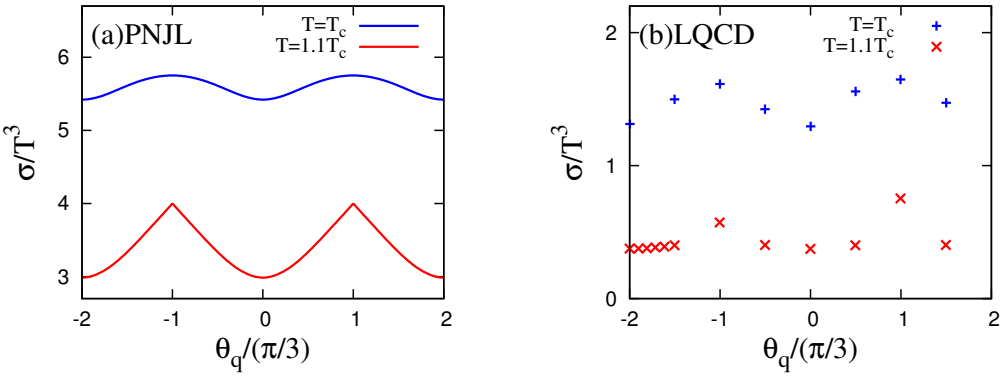

Figure 5.6: $\theta_{\rm q}$ dependence of the chiral condensate σ in (a) the PNJL model and (b) LQCD [35]. The red (blue) line corresponds to the case of $T = T_{\rm c}$ ($1.1T_{\rm c}$).

5.6.4 Quark-number density

Figure 5.7 shows the quark-number density, $\rho_{\rm q} = -\partial\Omega_{\rm PNJL}/\partial\mu_{\rm q} = i\beta(\partial\Omega_{\rm PNJL}/\partial\theta_{\rm q})$, which is purely imaginary, as a function of $\theta_{\rm q}$ at $T = T_{\rm c}$ and $1.1T_{\rm c}$. Panels (a) and (b) correspond to results of the PNJL model and LQCD [35], respectively. The quark-number density has the RW periodicity and it is $\theta_{\rm q}$-odd. The number density is smooth everywhere for low temperature of $T = T_{\rm c}$, but it has a discontinuity at $\theta_{\rm q} = (2k+1)\pi/3$ for high temperature of $T = 1.1T_{\rm c}$. The $\theta_{\rm q}$ dependence of the quark-number density is similar to that of the imaginary part of the modified Polyakov loop. This is natural because the quark-number density $\langle\bar{q}\gamma_4 q\rangle$ is the fourth component of the vector current, while the latter is related to the fourth component of the vector field. Particularly in the limit of $\beta E_{\rm q} \gg 1$,

the quark-number density is reduced to

$$\rho_{\rm q} = -\frac{\partial \Omega_{\rm PNJL}}{\partial \mu_{\rm q}} = 6N_{\rm f}\int \frac{d^3\mathbf{p}}{(2\pi)^3}(\Psi - \Psi^*)e^{-\beta E_{\rm q}} \propto i{\rm Im}(\Psi). \tag{5.19}$$

The quark-number density is thus proportional to the imaginary part of the modified Polyakov loop. The PNJL results are consistent with LQCD ones for $\theta_{\rm q}$ and T dependences of the quark-number density.

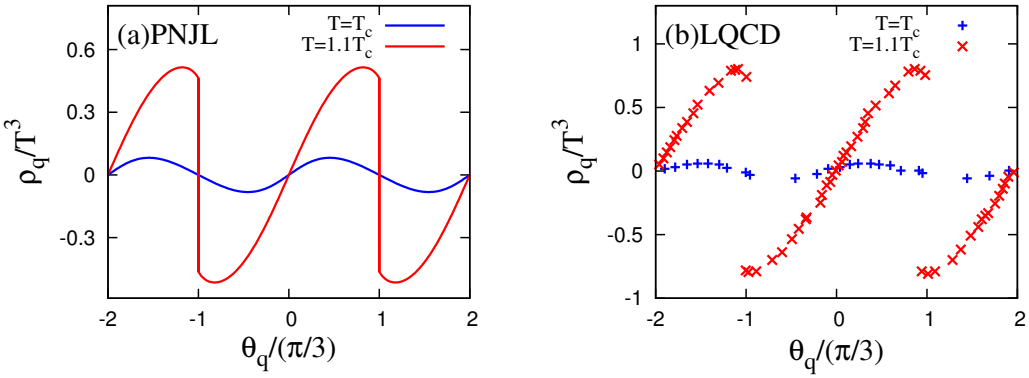

Figure 5.7: $\theta_{\rm q}$ dependence of the quark-number density $\rho_{\rm q}$ in (a) the PNJL model and (b) LQCD [35]. The red (blue) line corresponds to the case of $T = T_{\rm c}$ ($1.1T_{\rm c}$).

5.6.5 Meson masses

In the PNJL model, the model parameters of the quark sector are normally fitted to the meson properties. The parameters are quite sensitive to the meson masses. Furthermore the meson masses do not have an ambiguity of the renormalization, so that the meson masses are suitable for qualitative comparison of the model to LQCD. However the meson masses have not been calculated by LQCD yet. The pi and sigma meson masses, M_π and M_σ, are obtained as the zeros of the two-point mesonic correlation functions Γ_{ij} in the momentum space,

$$\Gamma_{jj}(q^2 = M_{\phi_j}^2) = \frac{\delta^2\Omega(\theta_{\rm q})}{\delta\phi_j(q)\delta\phi_j(-q)} = 0 \qquad \text{for} \quad \phi = (\pi,\ \sigma), \tag{5.20}$$

where the σ and π mesons do not couple to each other because of the parity conservation. The meson fields have no explicit θ_q dependence since they do not carry the quark-number, so that the two-point function and the meson masses have the RW periodicity and they are θ_q-even just as the thermodynamic potential $\Omega(\theta_q)$. Figure 5.8 (a) and (b) show the σ and π meson masses as a function θ_q at $T = T_c$ and $1.1T_c$. The meson masses are smooth everywhere for low temperature of $T = T_c$, but they have cusps at $\theta_q = (2k+1)\pi/3$ for high temperature of $T = 1.1T_c$. The mass difference between σ and π mesons as the chiral partner is a reflection of the chiral symmetry; namely the symmetry is restored (broken) when the difference is small (large). Panel (c) shows θ_q dependence of the meson

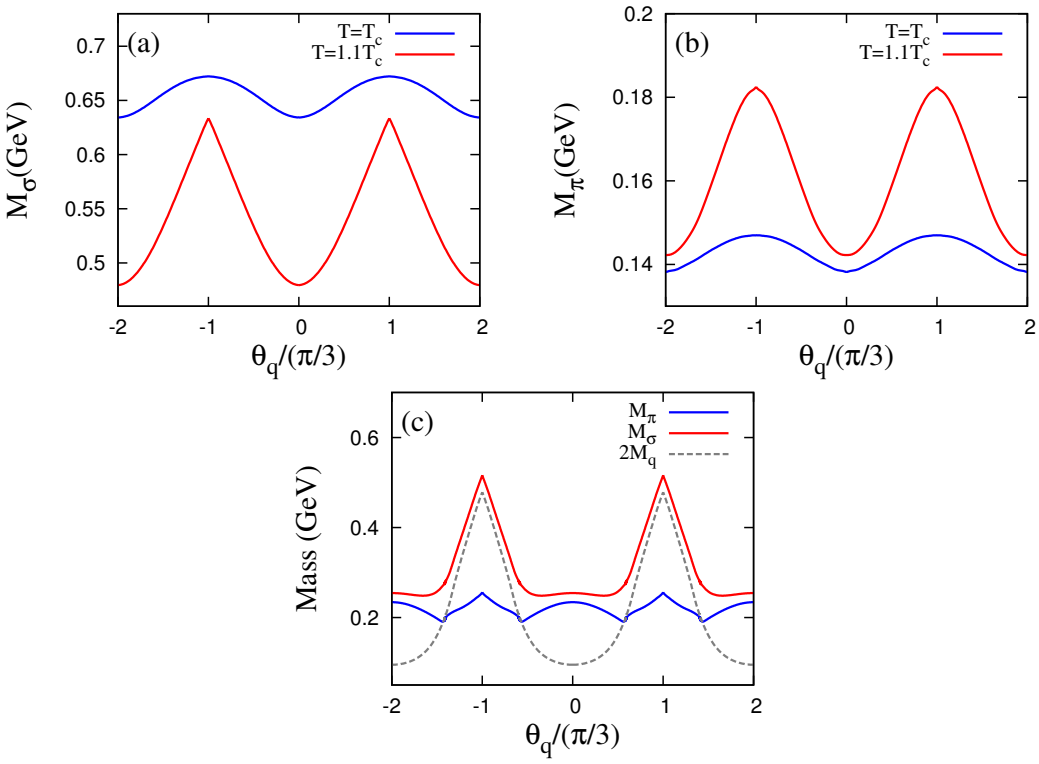

Figure 5.8: θ_q dependence of (a) the sigma meson mass M_σ and (b) the pi meson mass M_π calculated with the PNJL model. The red (blue) line corresponds to the case of $T = T_c$ ($1.1T_c$). Panel (c) represents M_σ (red), M_π (blue) and twice the dynamical quark mass $2M_q$ (gray) at $T = 1.3T_c$.

masses and twice the dynamical quark mass M_q at $T = 1.3T_c$. As shown in Fig.

5.6, the chiral symmetry is broken as θ_q increases. The mass difference between σ and π mesons is large in the chiral symmetry broken phase of $M_\pi \leq 2M_q$, but small in the restored phase of $M_\pi > 2M_q$. The meson masses thus have different θ_q-dependence between the two phases.

5.7 Phase diagram

When the RW phase transition occurs, θ_q-odd quantities such as the quark-number density ρ_q have discontinuities at $\theta_q = (2k+1)\pi/3$ as shown in Fig. 5.7. This is because θ_q-odd quantities have the relation (5.14). For $\theta_q = (2k+1)\pi/3$, such a quantity is zero below the critical temperature T_{RW} of the RW phase transition, but it is finite above T_{RW}. The θ_q-odd quantity is regarded as an order parameter of charge-conjugation. Figure 5.9 (a) and (b) show T depen-

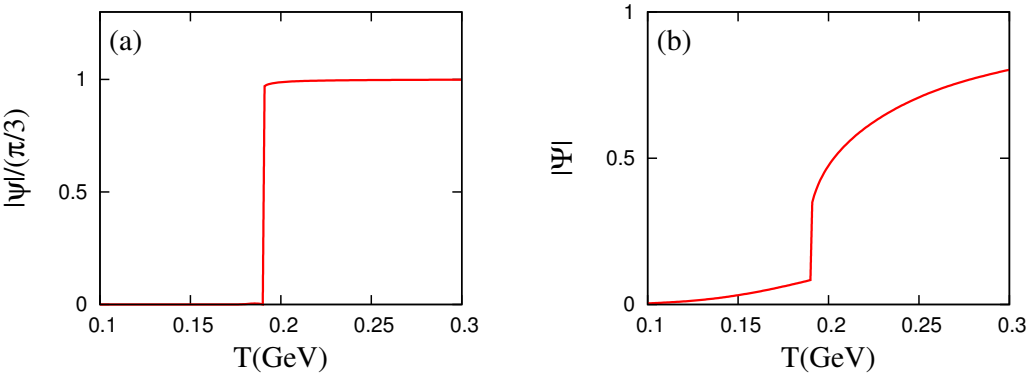

Figure 5.9: T dependence of (a) the phase $|\psi|$ and (b) the absolute value $|\Psi|$ of the modified Polyakov loop at $\theta_q = \pi/3$.

dences of the phase ψ and the absolute value $|\Psi|$ of the modified Polyakov loop at $\theta_q = \pi/3$, respectively. The phase (absolute value) is a θ_q-odd (θ_q-even) quantity. The phase ψ is zero at $T \leq T_{RW}$, while it is finite at $T > T_{RW}$. Thus, charge-conjugation symmetry is spontaneously broken above T_{RW}, although it is preserved below T_{RW}. The phase is discontinuous at $T = T_{RW}$, indicating that the RW transition is first-order at the endpoint. The absolute value $|\Psi|$ is also discontinuous there. This is induced by the discontinuity of the phase ψ. The

absolute value is not zero at $T < T_{\mathrm{RW}}$ since it is not an exact order parameter of the RW phase transition. Figure 5.10 shows the absolute value $|\Psi|$ in the θ_{q}-T

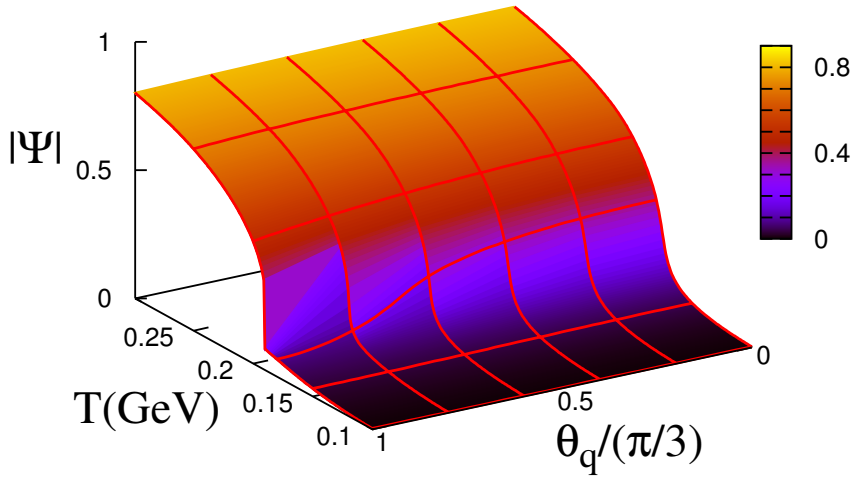

Figure 5.10: The absolute value of the modified Polyakov loop in the θ_{q}-T plane.

plane. The first-order RW phase transition at $\theta_{\mathrm{q}} = \pi/3$ becomes crossover as θ_{q} decreases from $\pi/3$ to 0. The crossover deconfinement transition at $\theta_{\mathrm{q}} = 0$, shown by a rapid change of $|\Psi|$ with an increase of T, is thus a remnant of the first-order RW phase transition at $\theta_{\mathrm{q}} = \pi/3$. Figure 5.11 shows the phase diagram in the θ_{q}-T plane. The phase diagram is symmetric with respect to each of lines $\theta_{\mathrm{q}} = k\pi/3$. The red and green curves represent the deconfinement and chiral phase transitions of crossover, respectively. The pseudocritical temperatures for the chiral and deconfinement transitions are determined by the peak positions of the susceptibilities of σ and $|\Psi|$[1], respectively. The blue vertical line represents the RW phase transition. Point E is the endpoint of the RW transitions. The deconfinement transition line starting from the RW endpoint decreases as θ_{q}decreases from $\pi/3$ to 0. The critical temperature of the chiral phase transition

[1]The susceptibilities $\chi_{\phi_i\phi_j}$ for $\phi = (\sigma,\ |\Psi|,\ \psi)$ are the inverse curvatures that are the derivatives with respect to ϕ_i and ϕ_j. The precise definition is shown in (3.29).

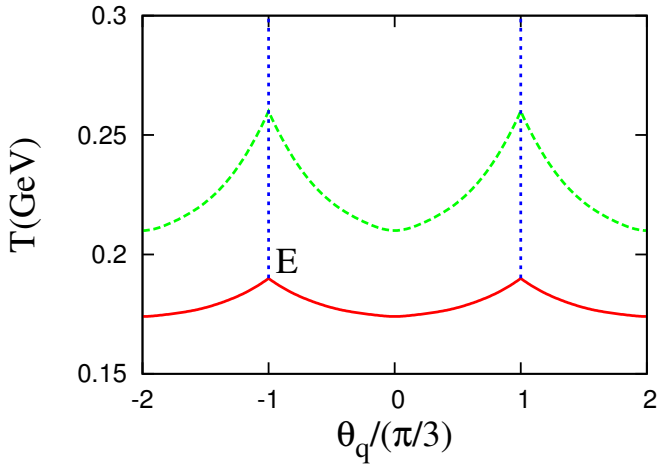

Figure 5.11: The phase diagram at imaginary μ_q. The red, green and blue lines represent the crossover deconfinement, the crossover chiral and the first-order RW phase transitions, respectively. Point E is the endpoint of the RW phase transition.

is higher by about 20 MeV than that of the deconfinement transition, and the difference is getting larger gradually as θ_q increases from 0 to $\pi/3$. Meanwhile, the LQCD simulation suggests that the two critical temperatures are identical for all θ_q [34; 35; 36; 37]. The inconsistency of the PNJL model to LQCD is addressed in Chapter 7.

5.8 Analytic continuation to real μ_q

Finally, we investigate the phase diagram in both the real and imaginary μ_q regions. In the PNJL model, physical quantities are calculable directly in the regions. Figure 5.12 shows the phase diagram in the μ_q^2-T plane. The $\mu_q^2 < 0$ and $\mu_q^2 > 0$ regions correspond to the imaginary and real μ_q regions, respectively. The solid (dashed) curve represents the first-order (crossover) chiral phase transition, while the dotted curve does the crossover deconfinement phase transition. The dot-dashed curve does the first-order RW transition. The chiral and deconfinement transition curves differ from each other. The two transition curves continue smoothly from imaginary μ_q to real μ_q, as expected. In LQCD [34; 35; 36; 37], the

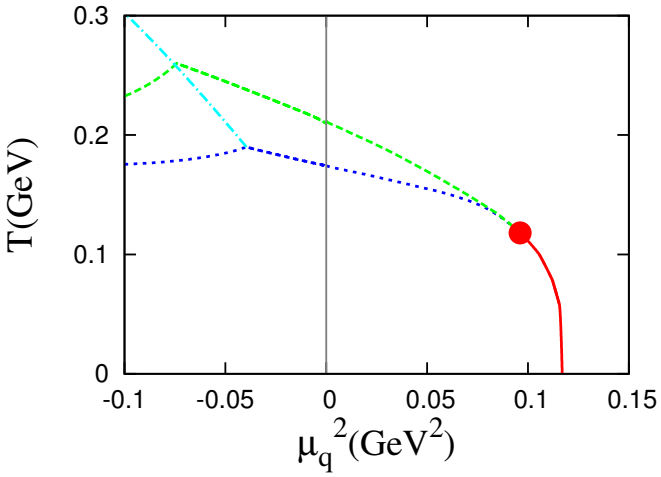

Figure 5.12: The phase diagram in the μ_q^2-T plane. The red (green) and blue lines represent the first-order (crossover) chiral and the crossover deconfinement phase transitions, respectively, while the right-blue line does the first-order RW phase transition.

extrapolation from imaginary μ_q to real μ_q has been made for the chiral transition curve by assuming some fitting functions where the coefficients are determined so as to reproduce the LQCD data at imaginary μ_q [34; 35; 36; 37]. We test the validity of the extrapolations for the chiral transition curve in the PNJL model. The extrapolation is made by a simple function

$$T_c = \sum_{n=0}^{n_{\max}} a_n \mu_q^{2n}, \tag{5.21}$$

where the coefficients are adjusted to the PNJL result at imaginary μ_q. In Fig. 5.13, four dashed curves labeled by 1-4 represent results of the simple extrapolation with $n_{\max}$ = 1-4, respectively. The dashed curve with $n_{\max} = 4$ still deviates from the PNJL curve in the real μ_q region. Thus, the PNJL curve includes higher-order terms with $n_{\max} \geq 5$ that the simple extrapolation cannot follow accurately. Furthermore, the simple extrapolation cannot predict the position of the critical endpoint. In general, for θ_q-even quantities $\mathcal{O}$ with the RW periodicity, the analytic continuation from imaginary μ_q to real μ_q is made by

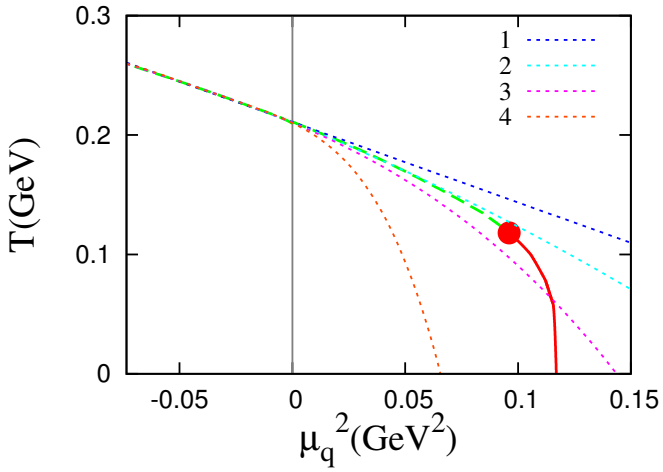

Figure 5.13: Extrapolation of the chiral phase transition curve from imaginary $\mu_{\rm q}$ to real $\mu_{\rm q}$. Dashed curves labeled 1-4 correspond to four cases with the truncations $n_{\rm max}$ = 1-4 in (5.21), respectively.

the Fourier expansion:

$$\mathcal{O}_{\rm im} = \sum_k a_k(T)\cos(3k\theta_{\rm q}) \quad \rightarrow \quad \mathcal{O}_{\rm re} = \sum_k a_k(T)\cosh(3k\mu_{\rm q}/T). \tag{5.22}$$

Note that the trigonometric functions at imaginary $\mu_{\rm q}$ become the hyperbolic ones at real $\mu_{\rm q}$. For real $\mu_{\rm q}$, the terms with higher order k more contribute in the series. It is very difficult to estimate the coefficients with higher order terms from the LQCD data because such a coefficient is extremely small. The same situation is true for the $\theta_{\rm q}$-odd quantities. This is why such an extrapolation is difficult.

5.9 Remarks

We remark some topics related with imaginary $\mu_{\rm q}$. One is an analogy of the mechanism of the RW phase transition to the Dashen mechanism in the so-called $\theta_{\rm t}$ vacuum. Another is a problem in predicting the phase diagram at real $\mu_{\rm q}$. The vector-type interaction strongly affects the location of the critical endpoint at real $\mu_{\rm q}$, but the strength of the interaction was unknown so far. It is possible

to determine the strength by comparing the PNJL result with the LQCD data at imaginary $\mu_{\rm q}$.

5.9.1 Analogy to the Dashen mechanism

When the RW phase transition occurs, $\theta_{\rm q}$-odd quantities are finite at $\theta_{\rm q} = (2k+1)\pi/3$, so that charge-conjugation symmetry is spontaneously broken there. This RW mechanism is analogous to the Dashen mechanism [47] in the so-called $\theta_{\rm t}$ vacuum. The QCD action is allowed to have a topological term

$$i\theta_{\rm t} \int d^4x \ \frac{1}{64\pi^2} \epsilon^{\mu\nu\rho\sigma} F^a_{\mu\nu} F^a_{\rho\sigma} = i\theta_{\rm t} N_{\rm t} \tag{5.23}$$

of the topological charge $N_{\rm t}$, where $F^a_{\mu\nu}$ is the field strength of gluon. This topological term is odd under parity P. For imaginary $\mu_{\rm q} = i\theta_{\rm q}/\beta$, the QCD action has a term

$$\mu_{\rm q} \int d^4x \ \bar{q}\gamma_4 q = i\theta_{\rm q} N_{\rm q}, \tag{5.24}$$

where $N_{\rm q}$ is the quark-number. The term, which is odd under charge-conjugation C, has a mathematical structure similar to the topological term $\mathcal{L}_{\rm t}$. For both the terms, the parameters, θ_i (i = t, q), can vary between $-\pi$ and π, where $\theta_i = -\pi$ is identical with $\theta_i = \pi$. Since the term with $\theta_{\rm t}$ ($\theta_{\rm q}$) is P-odd (C-odd), P (C) is an exact symmetry when $\theta_{\rm t}$ ($\theta_{\rm q}$) is equal to 0 and $\pm\pi$. For $\theta_{\rm t} = \pi$, P is spontaneously broken, as Dashen [47] and Witten [48] pointed out. This is the so-called Dashen phenomenon. Thus, the spontaneous C breaking at $\theta_{\rm q} = \pi$ is analogous to the P breaking at $\theta_{\rm t} = \pi$. Note that $\theta_{\rm q} = (2k+1)\pi/3$ has the same property as $\theta_{\rm q} = \pi$ because of the RW periodicity. As discussed in Sec. 5.4, there exist three $\mathbb{Z}_3$ vacua for higher temperature. As $\theta_{\rm q}$ increases from $-\pi$ to π, the three vacua emerge one by one. As a consequence of this mechanism, three first-order phase transitions appear at $\theta_{\rm q} = \pm\pi/3$ and π. At $\theta_{\rm q} = \pm\pi/3$ and π, thus, a mechanism similar to the Dashen phenomena at $\theta_{\rm t} = \pi$ takes place. The transitions at $\theta_{\rm q} = \pm\pi/3$ and π are called the RW transition. The C breaking at $\theta_{\rm q} = \pi/3$ occurs when T is high, while the P breaking at $\theta_{\rm t} = \pi$ takes place when T is small. The PNJL model can describe both the RW and the Dashen

mechanism.

5.9.2 Vector-type interaction

The PNJL model is allowed to have a vector-type interaction

$$G_{\mathrm{v}}(\bar{q}\gamma_{\nu}q)^2, \tag{5.25}$$

since it does not break the chiral symmetry. We assume the homogeneous vacuum, so that only the temporal condensate, which corresponds to the quark-number density $\rho_{\mathrm{q}} = \langle \bar{q}\gamma_4 q \rangle$, can occur. When the vector-type interaction is added to the PNJL Lagrangian, the meson potential U_{M} and the quark chemical potential μ_{q} in the thermodynamic potential are modified as

$$U_{\mathrm{M}} = G_{\mathrm{s}}\sigma^2 \to \tilde{U}_{\mathrm{M}} = G_{\mathrm{s}}\sigma^2 + G_{\mathrm{v}}\rho_{\mathrm{q}}^2, \quad \mu_{\mathrm{q}} \to \tilde{\mu}_{\mathrm{q}} = \mu_{\mathrm{q}} - 2G_{\mathrm{v}}\rho_{\mathrm{q}}, \tag{5.26}$$

in the mean field approximation. Figure 5.14 shows the location of the critical

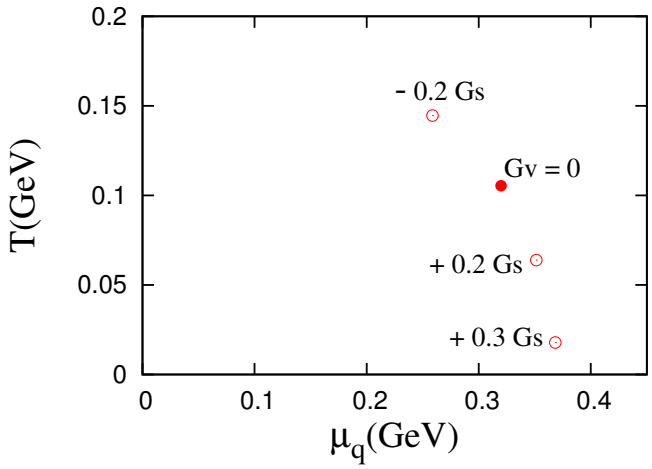

Figure 5.14: Dependence of the location of the critical endpoint on the strength G_{v} of the vector-type interaction. The strength G_{v} is normalized by the strength G_{s} of the scalar-type interaction.

endpoint of the first-order chiral phase transition at real μ_{q} for several values of the strength G_{v} of the vector-type interaction. The location is quite sensi-

tive to the values of $G_{\rm v}$. The vector-type interaction moves largely the critical endpoint toward smaller T and larger $\mu_{\rm q}$. The vector-type interaction is important to account for the saturation property of nuclear matter, since the repulsive force mediated by vector mesons is necessary for the saturation. Thus, it is phenomenologically essential to determine the strength of $G_{\rm v}$ in particularly at the finite quark-number density region corresponding to the nuclear saturation density. The strength cannot be determined from physical quantities at zero $\mu_{\rm q}$ because the interaction affects physical quantities only at finite $\mu_{\rm q}$. We propose a possibility to determine the strength of vector-type interaction from the imaginary $\mu_{\rm q}$ region. Figure 5.15 represents (a) the chiral condensate σ, (b) the

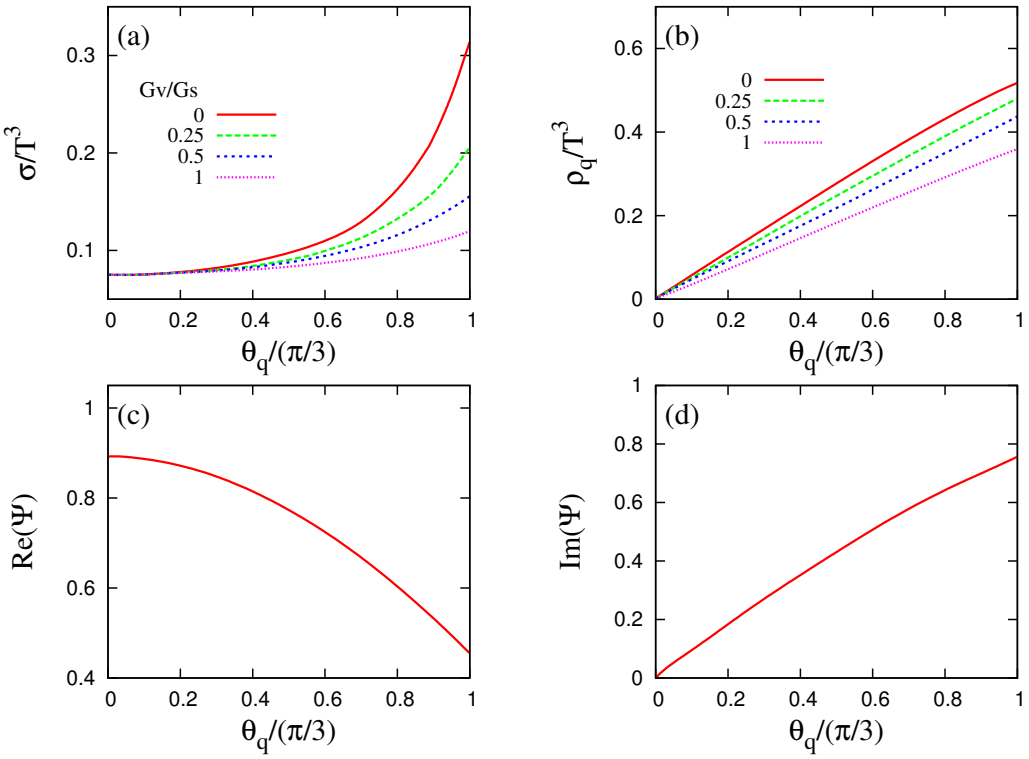

Figure 5.15: Impact of the vector-type interaction on (a) the chiral condensate, (b) the quark-number density, (c) the real and (d) the imaginary part of the modified Polyakov loop at $T = 1.5T_{\rm c}$. The red, green, blue and pink curves are results for $G_{\rm v}/G_{\rm s} = 0$, 0.25, 0.5 and 1, respectively. In the panel (c) and (d), the four cases yield the same result.

quark-number density $\rho_{\rm q}$, (c) the real and (d) the imaginary part of the modified Polyakov loop Ψ for various values of $G_{\rm v}$. Here we consider the case of $T = 1.5T_{\rm c}$, since the effect of the vector-type interaction is more conspicuous at higher temperatures. The vector-type interaction suppresses the effective chemical potential $\tilde{\mu}_{\rm q}$ as shown in (5.26). The suppression yields significant effects on the quark condensates, σ and $\rho_{\rm q}$. In contrast, such an effect is not seen for the Polyakov loop because it is mainly determined by the Polyakov potential. If precise LQCD data on σ and $\rho_{\rm q}$ becomes available in future, we can determine the strength $G_{\rm v}$ from the data by using the PNJL model.

5.10 Summary

We have investigated the imaginary quark chemical potential $\mu_{\rm q}$ region by using the PNJL model. Lattice QCD (LQCD) is free from the sign problem at imaginary $\mu_{\rm q}$ so that LQCD calculations have been done in this region. The QCD partition function is a function of $\mu_{\rm q}^2$ and the physical quantities can be analytically continued from imaginary $\mu_{\rm q}$ to real $\mu_{\rm q}$. When the LQCD quantities are available at imaginary $\mu_{\rm q}$, we can extrapolate them to real $\mu_{\rm q}$. So far the extrapolation was done directly by assuming some analytic function, but there are many ambiguities in the assumption. Here we propose the extrapolation by using an effective model that can evaluate the partition function at both real and imaginary $\mu_{\rm q}$ and reproduce results of LQCD at imaginary $\mu_{\rm q}$. Many effective models have been proposed so far and each model has predicted each phase diagram at real $\mu_{\rm q}$. It is then highly nontrivial whether the models predict properly dynamics of QCD at finite $\mu_{\rm q}$. Fortunately, the model reliability can be tested directly from QCD at imaginary $\mu_{\rm q}$, since LQCD is feasible there. We show that the PNJL model reproduces the LQCD results qualitatively. The success of the PNJL model comes from the fact that the model has the extended $\mathbb{Z}_3$ symmetry. As a consequence of the extended $\mathbb{Z}_3$ symmetry, the partition functions of QCD and the PNJL model have the Roberge-Weiss (RW) periodicity, which characterizes observables at imaginary $\mu_{\rm q}$. Furthermore the PNJL model reproduces the RW phase transition at high temperature. Above the critical temperature $T_{\rm RW}$ of the RW phase transition, three $\mathbb{Z}_3$ vacua emerge alternatively in variation of

$\theta_{\rm q}$ and a phase transition occurs at the boundary, that is at $\theta_{\rm q} = (2k+1)\pi/3$ for integer k. For $\theta_{\rm q} = (2k+1)\pi/3$, $\theta_{\rm q}$-odd quantities, which are order parameters of charge-conjugation, have finite values and charge-conjugation symmetry is spontaneously broken above $T_{\rm RW}$. This is the mechanism of the RW phase transition and the mechanism is analogous to the Dashen mechanism in the $\theta_{\rm t}$ vacuum. The RW phase transition is of first-order at the endpoint $T_{\rm RW}$. As a consequence of the transition, the absolute value of the Polyakov loop has a singular behavior at the endpoint $T_{\rm RW}$. The singular behavior induces a rapid change of the Polyakov loop even at $\theta_{\rm q} = 0$. Thus, the crossover deconfinement transition at $\theta_{\rm q} = 0$ is a remnant of the first-order RW phase transition at $\theta_{\rm q} = \pi/3$. As another important result, the strength of the vector-type interaction can be determined by comparing the PNJL model results with LQCD data at imaginary $\mu_{\rm q}$, if the precise data becomes available in future. The determination is quite important since the location of the critical endpoint of the chiral phase transition at real $\mu_{\rm q}$ is quite sensitive to the strength. In this chapter, we have compared the PNJL model results with LQCD ones only qualitatively. In the chapter 7, we improve the present model in order to reproduce the LQCD results quantitatively.

Chapter 6

Isospin Chemical Potential

In the previous chapter, we proposed an analytic continuation from imaginary chemical potential to real one by using an effective model such as the PNJL model. The validity of the method is confirmable in the isospin chemical potential $\mu_{\rm iso}$. Lattice QCD (LQCD) does not have the sign problem at real and imaginary $\mu_{\rm iso}$ so that it is possible to check the validity by comparing the model results with LQCD data directly. Furthermore the isospin chemical potential region is also relevant to the real world such as neutron stars and relativistic heavy-ion collisions. This chapter is mainly based on our papers [49].

6.1 Purpose

The study of QCD at finite temperature and quark-number density has many phenomenological interests related to the physics of heavy-ion experiments and compact astrophysical objects. One of the aims of the study QCD is how the transition between hadronic and quark-gluon degrees of freedom occurs as a function of conserved charge. In QCD, isospin is such a conserved charge like the baryon number, and it is natural to inquire what happens in QCD as a function of isospin density or isospin chemical potential $\mu_{\rm iso}$. The isospin chemical potential is also relevant to the real world. Nature provides us with nonzero $\mu_{\rm iso}$ systems in the form of isospin-asymmetric matter such as neutron stars. The relativistic heavy-ion collisions produce hadronic matter at high temperature and finite

baryon-number density. In the collisions, the isospin density is nonzero generally. Hence it is interesting to study QCD with finite isospin density. As discussed in Chapter 4, the first-principle lattice QCD (LQCD) has the sign problem when the quark chemical potential $\mu_{\rm q}$ is real. The integrand of the partition function with real $\mu_{\rm q}$ becomes complex because of the property of the Dirac operator $\mathcal{D} = \gamma_\nu D_\nu + m - \mu_{\rm q}\gamma_4$ in the integrand,

$$\det \mathcal{D}^\dagger(\mu_{\rm q}) = \det(\gamma_5 \mathcal{D}(-\mu_{\rm q}^*)\gamma_5) = \det \mathcal{D}(-\mu_{\rm q}^*), \tag{6.1}$$

and hence the importance sampling in the Monte Carlo calculation breaks down. For real isospin chemical potential $\mu_{\rm iso}$, the chemical potential μ_u for u-quark is opposite to that μ_d for d-quark, $\mu_u = -\mu_d = \mu_{\rm iso}$, so that the Dirac determinant of u-quark is the complex conjugate of that of d-quark and consequently the product is positive [50]. As discussed in Chapter 4, the theory with real $\mu_{\rm iso}$ corresponds to the phase-quenched one with real $\mu_{\rm q}$ where the phase of the Dirac determinant is eliminated [51]. For imaginary $\mu_{\rm iso}$, the Dirac determinant is positive in the same reason as imaginary $\mu_{\rm q}$ as shown in the relation (6.1). Therefore LQCD does not have the sign problem in both real and imaginary $\mu_{\rm iso}$. As shown in Chapter 5, one approach to the real $\mu_{\rm q}$ region is the analytic continuation from imaginary $\mu_{\rm q}$ to real $\mu_{\rm q}$. The same analytic continuation can be done from imaginary $\mu_{\rm iso}$ to real $\mu_{\rm iso}$. LQCD calculation can be done in both the real and imaginary $\mu_{\rm iso}$ regions [52], and we can check the validity of the analytic continuation by comparing with LQCD data directly. In Chapter 5, we propose the analytic continuation by using an effective model that can evaluate the partition function at both real and imaginary $\mu_{\rm q}$ and reproduce LQCD results at imaginary $\mu_{\rm q}$. The PNJL model is a realistic effective model that can do this. The model reproduces LQCD data at imaginary $\mu_{\rm q}$ as shown in Chapter 5. For the purpose to check the validity, we explore the isospin chemical potential region by using the PNJL model. First we consider the case that both $\mu_{\rm iso}$ and $\mu_{\rm q}$ are purely imaginary where there is no sign problem. In this region, LQCD has calculated $\mu_{\rm q}$ and $\mu_{\rm iso}$ dependences of the thermodynamic potential and its first derivatives with respect to $\mu_{\rm q}$ and $\mu_{\rm iso}$, that is the quark-number and isospin densities [31]. We show that the PNJL model reproduces LQCD results qualitatively in the region. We proceed

some quantitative comparison of the PNJL model with LQCD. Second we explore the real $\mu_{\rm iso}$ region. We review properties of QCD at real $\mu_{\rm iso}$ and show that the PNJL model reproduces them qualitatively.

6.2 Pion at isospin chemical potential

The isospin chemical potential causes asymmetry between u- and d-quarks, so that the isovector mesons, i.e., the charged pions $\pi_\pm$, are affected by the chemical potential. Here we discuss the pion properties at isospin chemical potential $\mu_{\rm iso}$ following Ref. [50].

6.2.1 QCD inequalities

When the Dirac determinant is positive, some rigorous results on its low-energy behavior can be obtained from QCD inequalities [53]. At vacuum, the inequalities rely on the following property of the Dirac operator $\mathcal{D} = \gamma_\nu D_\nu + m$:

$$\gamma_5 \mathcal{D} \gamma_5 = \mathcal{D}^\dagger. \tag{6.2}$$

which, in particular, implies the positivity $\det \mathcal{D} \geq 0$. For the correlator of a generic meson $M = \bar{q}\Gamma q$, we can write, using (6.2) and the Schwartz inequality:

$$\begin{aligned} \left\langle M(x) M^\dagger(0) \right\rangle &= -\left\langle {\rm Tr} S(x,0) \Gamma S(0,x) \bar{\Gamma} \right\rangle \\ &= \left\langle {\rm Tr} S(x,0) \Gamma i\gamma_5 S^\dagger(x,0) i\gamma_5 \bar{\Gamma} \right\rangle \leq \left\langle {\rm Tr} S(x,0) S^\dagger(x,0) \right\rangle \end{aligned} \tag{6.3}$$

where $S = \mathcal{D}^{-1}$ and $\bar{\Gamma} = \gamma_4 \Gamma^\dagger \gamma_4$. The inequality is saturated for mesons with $\Gamma = i\gamma_5 \tau_i$, since $\mathcal{D}$ commutes with isospin τ_i. The pseudoscalar correlators are thus larger than others. The meson correlator $\left\langle M(x) M^\dagger(0) \right\rangle$ has a relation to the meson mass M_Γ, $\left\langle M(x) M^\dagger(0) \right\rangle \propto e^{-M_\Gamma x}$, so that the pseudoscalar mesons are lighter than others. At finite isospin chemical potential, $\mu_{\rm iso} \neq 0$, the Dirac determinant is modified as $\mathcal{D} = \gamma_\nu D_\nu + m - \mu_{\rm iso} \gamma_4 \tau_3$. For the degenerated two-flavor of $m_u = m_d$, the determinant is still positivity, where the u- and d-quarks play the role of mutually conjugate quarks as shown in (4.2). The Dirac operator

does not satisfy the relation (6.2), but it does a similar relation,

$$\tau_1\gamma_5\mathcal{D}\gamma_5\tau_1 = \tau_2\gamma_5\mathcal{D}\gamma_5\tau_2 = \mathcal{D}^\dagger. \tag{6.4}$$

which ensures that $\det\mathcal{D} \geq 0$. Repeating the derivation of the QCD inequalities, and using (6.4), we obtain that the lightest meson, or the condensate, must be in channels $\bar{q}i\gamma_5\tau_{1,2}q$, that is a linear combination of $\pi_+ = \bar{u}\gamma_5 d$ and $\pi_- = \bar{d}\gamma_5 u$ states.

6.2.2 Chiral perturbation theory

When $\mu_{\rm iso}$ is small compared to the chiral scale (the ρ meson mass), we can use the chiral perturbation theory. For zero quark mass and zero $\mu_{\rm iso}$, pions are massless Nambu-Goldstone bosons of the spontaneously broken $SU(2)_{\rm L}\times SU(2)_{\rm R}$ chiral symmetry. If the quarks have small equal masses, the symmetry is only $SU(2)_{\rm V}$. The isospin chemical potential further breaks $SU(2)_{\rm V}$ down to $U(1)_{\rm I_3}$, where $U(1)_{\rm I_3}$ is the isospin subgroup and quark is transformed under the subgroup as $q \to e^{-i\alpha\tau_3}q$. Its effect can be included in $\mu_{\rm iso}$ by promoting $SU(2)_{\rm L}\times SU(2)_{\rm R}$ to a local gauge symmetry and viewing $\mu_{\rm iso}$ as the temporal component of gauge field. The chiral Lagrangian for pion field $\Sigma \in SU(2)$ with finite $\mu_{\rm iso}$ is [50]

$$\mathcal{L}_{\rm eff} = \frac{f_\pi^2}{4}{\rm Tr}\nabla_\nu\Sigma\nabla_\nu\Sigma^\dagger - \frac{M_\pi^2 f_\pi^2}{2}{\rm ReTr}\Sigma \tag{6.5}$$

with flavor covariant derivatives

$$\nabla_4\Sigma = \partial_4\Sigma - \mu_{\rm iso}\left(\tau_3\Sigma - \Sigma\tau_3\right), \quad \nabla_i\Sigma = \partial_i\Sigma, \quad i = 1,2,3 \tag{6.6}$$

where M_π and f_π are the pion mass and its decay constant at vacuum, respectively. It is straightforward to determine vacuum alignment of Σ as a function of $\mu_{\rm iso}$. From (6.5), we find the potential energy for Σ,

$$\mathcal{V}_{\rm eff}(\Sigma) = \frac{(f_\pi\mu_{\rm iso})^2}{2}{\rm Tr}(\tau_3\Sigma\tau_3\Sigma^\dagger - 1) - \frac{(f_\pi M_\pi)^2}{2}{\rm ReTr}\Sigma. \tag{6.7}$$

The first term in (6.7) favors directions of τ_1 and τ_2, while the second term prefers the vacuum direction τ_0. The vacuum expectation value $\overline{\Sigma}$ is described by

$$\overline{\Sigma} = \tau_0 \cos\alpha + i(\tau_1 \cos\phi + \tau_2 \sin\phi)\sin\alpha. \tag{6.8}$$

The tilt angle α is determined by minimizing the potential $\mathcal{V}_{\rm eff}$

$$\mathcal{V}_{\rm eff} = 2(f_\pi \mu_{\rm iso})^2 \left[(\cos\alpha - a)^2 - 1 - a^2\right] \tag{6.9}$$

with $a = (M_\pi/2\mu_{\rm iso})^2$. The energy is degenerated with respect to angle ϕ, respecting the $U(1)_{\rm I_3}$ symmetry in the Lagrangian (6.5). When $\mu_{\rm iso} < M_\pi/2$, the potential has a minimum at $\alpha = 0$, and the $U(1)_{\rm I_3}$ symmetry is not broken. When $\mu_{\rm iso} > M_\pi/2$, while the potential has a minimum at $\cos\alpha = (M_\pi/2\mu_{\rm iso})^2$, so that the charged pion condensation occurs and the $U(1)_{\rm I_3}$ symmetry is spontaneously broken there. This result is easy to understand. The lowest lying pion state π_+ costs a positive energy $M_\pi - 2\mu_{\rm iso}$ to excite, thus at zero temperature no pion is excited. For $\mu_{\rm iso} > M_\pi/2$, the energy to excite a π_+ meson, $M_\pi - 2\mu_{\rm iso}$, is negative, thus it is energetically favorable to excite a large number of them. Since pions are bosons, the result is a Bose-Einstein condensate of π_+. For imaginary $\mu_{\rm iso} = i\nu$ [49], the potential is obtained as

$$\mathcal{V}_{\rm eff} = -2(f_\pi \nu)^2 \left[(\cos\alpha + b)^2 - 1 - b^2\right] \tag{6.10}$$

with $b = (M_\pi/2\nu)^2$, which always has a minimum at $\alpha = 0$. The charged pion condensation thus does not occur at imaginary $\mu_{\rm iso}$. This result is also easy to understand. For real $\mu_{\rm iso}$, the Bose-Einstein distribution function of pion has an infrared divergence at $\mu_{\rm iso} \geq M_\pi/2$. This induces the pion condensate as a Bose-Einstein condensate. For imaginary $\mu_{\rm iso}$, such a divergence never happens and then no pion condensation occurs.

6.3 Imaginary isospin chemical potential

LQCD does not have the sign problem in the case that both $\mu_{\rm iso}$ and $\mu_{\rm q}$ are purely imaginary, i.e., $\mu_{\rm q} = i\theta_{\rm q}/\beta$ and $\mu_{\rm iso} = i\theta_{\rm iso}/\beta$ for real $\theta_{\rm q}$ and $\theta_{\rm iso}$. In the imaginary

$\mu_{\rm q}$ region, the QCD partition function has the Roberge-Weiss (RW) periodicity in $\theta_{\rm q}$ and its phase transition as discussed in Chapter 5. The properties are preserved even for finite $\mu_{\rm iso}$. The partition function also has a periodicity of 2π in $\theta_{\rm iso}$ because the isospin is good quantum whenever the charged pion condensate does not occur. Therefore the partition function has higher discrete symmetries at imaginary $\mu_{\rm iso}$ and $\mu_{\rm q}$. The PNJL model possesses all the symmetries, and then the model reproduces LQCD data [31] qualitatively. Furthermore the PNJL model reproduces LQCD data quantitatively by including the hadronic excitations.

6.3.1 Properties of the partition function

When QCD vacuum keeps the $U(1)_{\rm V}$ and $U(1)_{\rm I_3}$ symmetries, the quark-number $N_{\rm q} = V\langle\bar{q}\gamma_4 q\rangle$ and the isospin $N_{\rm iso} = V\langle\bar{q}\gamma_4\tau_3 q\rangle$ are both integer. The partition function Z depends on $\theta_{\rm q}$ and $\theta_{\rm iso}$ only through the form, $\exp(i\theta_{\rm q}N_{\rm q} + i\theta_{\rm iso}N_{\rm iso})$. The partition function $Z(\theta_{\rm q}, \theta_{\rm iso})$ has thus the periodicity

$$Z(\theta_{\rm q}, \theta_{\rm iso}) = Z(\theta_{\rm q} + 2\pi, \theta_{\rm iso}) = Z(\theta_{\rm q}, \theta_{\rm iso} + 2\pi). \tag{6.11}$$

The partition function also preserves the RW periodicity

$$Z(\theta_{\rm q}, \theta_{\rm iso}) = Z(\theta_{\rm q} + 2\pi k/3, \theta_{\rm iso}) \quad \text{for} \quad k \in \mathbb{Z}, \tag{6.12}$$

which has been shown by repeating the derivation of the RW periodicity in Sec. 5.3. The relation (6.11) is not satisfied when there is the charged pion condensate $\langle\bar{q}i\gamma_5\tau_{1,2}q\rangle$ that breaks the $U(1)_{\rm I_3}$ symmetry, i.e., $N_{\rm iso}$ is no longer integer there. The pion condensate however does not occur at imaginary $\mu_{\rm iso}$ as shown in (6.10), so that u- and d-quarks are decoupled to each other. The partition function $Z_u(\theta_u)$ for u-quark and that $Z_d(\theta_d)$ for d-quark have the periodicity of 2π respectively, and the total partition function $Z(\theta_{\rm q}, \theta_{\rm iso})$ satisfies

$$\begin{aligned} Z(\theta_{\rm q} + \pi, \theta_{\rm iso}) &= Z_u(\theta_{\rm q} + \theta_{\rm iso} + \pi) + Z_d(\theta_{\rm q} - \theta_{\rm iso} + \pi) \\ &= Z_u(\theta_{\rm q} + \theta_{\rm iso} + \pi) + Z_d(\theta_{\rm q} - \theta_{\rm iso} - \pi) = Z(\theta_{\rm q}, \theta_{\rm iso} + \pi). \end{aligned} \tag{6.13}$$

Combining the relation (6.13) and the RW periodicity (6.12), we can thus obtain

$$Z(\theta_{\mathrm{q}}, \theta_{\mathrm{iso}} + \pi) = Z(\theta_{\mathrm{q}} + \pi/3, \theta_{\mathrm{iso}}). \tag{6.14}$$

Furthermore, in the isospin symmetric case, $m_u = m_d$, the partition function is invariant under the interchange $u \leftrightarrow d$, which means

$$Z(\theta_{\mathrm{q}}, \theta_{\mathrm{iso}}) = Z(\theta_{\mathrm{q}}, -\theta_{\mathrm{iso}}). \tag{6.15}$$

The partition function is also invariant under charge conjugation,

$$Z(\theta_{\mathrm{q}}, \theta_{\mathrm{iso}}) = Z(-\theta_{\mathrm{q}}, -\theta_{\mathrm{iso}}). \tag{6.16}$$

Combining with the relation (6.15) and (6.16), we can obtain

$$Z(\theta_{\mathrm{q}}, \theta_{\mathrm{iso}}) = Z(-\theta_{\mathrm{q}}, \theta_{\mathrm{iso}}). \tag{6.17}$$

The partition function is thus θ_{q}-even and θ_{iso}-even. Particularly for $\theta_{\mathrm{iso}} = \pi/2$, the partition function Z has a periodicity of $\pi/3$ in θ_{q}, because taking $\theta_{\mathrm{iso}} = \pi/2$ in (6.14) combined with the θ_{iso}-evenness leads to

$$Z(\theta_{\mathrm{q}}, \pi/2) = Z(\theta_{\mathrm{q}} + \pi/3, \pi/2). \tag{6.18}$$

Similarly for $\theta_{\mathrm{q}} = \pi/6$, Z has a periodicity of π in θ_{iso}, because taking $\theta_{\mathrm{q}} = \pi/6$ in (6.14) combined with θ_{q}-evenness leads to

$$Z(\pi/6, \theta_{\mathrm{iso}}) = Z(\pi/6, \theta_{\mathrm{iso}} + \pi). \tag{6.19}$$

6.3.2 PNJL model

The two-flavor PNJL Lagrangian with the quark chemical potential μ_{q} and the isospin chemical potential μ_{iso} is

$$\mathcal{L} = \bar{q}(\gamma_\nu D_\nu - \gamma_4(\mu_{\mathrm{q}} + \mu_{\mathrm{iso}}\tau_3) + m_0)q - G_{\mathrm{s}}[(\bar{q}q)^2 + (\bar{q}i\gamma_5\vec{\tau}q)^2] + U_\Phi, \tag{6.20}$$

where $D_\nu = \partial_\nu + iA_4\delta_{4\nu}$ and $A_4 = \phi_3\lambda_3 + \phi_8\lambda_8$ under the Polyakov gauge. For $m_0 = \mu_{\rm iso} = 0$, the PNJL Lagrangian has the $SU(2)_{\rm L} \times SU(2)_{\rm R} \times U(1)_{\rm V}$ symmetry. For $m_0 \neq 0$ and $\mu_{\rm iso} \neq 0$, it is reduced to $U(1)_{\rm I_3} \times U(1)_{\rm V}$. The spontaneous breakings of the chiral and the $U(1)_{\rm I_3}$ symmetry are described by the chiral condensate $\sigma = \langle\bar{q}q\rangle$ and the charged pion condensate $\pi = \langle\bar{q}i\gamma_5\tau_1 q\rangle$, respectively, where the τ_1 direction is taken as the $U(1)_{\rm I_3}$ symmetry breaking. In the mean field approximation, the thermodynamic potential $\Omega_{\rm PNJL}$ is obtained as

$$\Omega_{\rm PNJL} = -2\sum_{\rm f=\pm}\int\frac{d^3{\rm p}}{(2\pi)^3}\left[3E_{\rm f} + \frac{1}{\beta}\left(\ln\mathcal{F}_{\rm f} + \ln\mathcal{F}_{\bar{\rm f}}\right)\right] + U_{\rm M} + U_\Phi, \tag{6.21}$$

with

$$\mathcal{F}_{\rm f} = 1 + 3\Phi e^{-\beta(E_{\rm f}-\mu_{\rm q})} + 3\Phi^* e^{-2\beta(E_{\rm f}-\mu_{\rm q})} + e^{-3\beta(E_{\rm f}-\mu_{\rm q})}, \tag{6.22}$$

$$\mathcal{F}_{\bar{\rm f}} = 1 + 3\Phi^* e^{-\beta(E_{\rm f}+\mu_{\rm q})} + 3\Phi e^{-2\beta(E_{\rm f}+\mu_{\rm q})} + e^{-3\beta(E_{\rm f}+\mu_{\rm q})}, \tag{6.23}$$

where $U_{\rm M} = G_{\rm s}(\sigma^2+\pi^2)$ and $E_\pm = \sqrt{(E_{\rm q}\pm\mu_{\rm iso})^2 + N^2}$ with $E_{\rm q} = \sqrt{{\rm p}^2 + M_{\rm q}^2}$, $M_{\rm q} = m_0 - 2G_{\rm s}\sigma$, $N = -2G_{\rm s}\pi$. The terms with ${\rm f} = +(-)$ represent the potential of u-quark (d-quark). If the pion condensate occurred $\pi \neq 0$, the potential $\Omega_{\rm PNJL}$ would not have periodicities in (6.11)-(6.19) at imaginary $\mu_{\rm iso}$. However for imaginary $\mu_{\rm q} = i\theta_{\rm q}/\beta$ and $\mu_{\rm iso} = i\theta_{\rm iso}/\beta$, since the pion condensate does not occur, the potential is reduced to a simpler form

$$\Omega_{\rm PNJL} = -2\sum_{\rm f=\pm}\int\frac{d^3{\rm p}}{(2\pi)^3}\left[3E_{\rm q} + \frac{1}{\beta}\left(\ln\mathcal{F}_{\rm f} + \ln\mathcal{F}_{\bar{\rm f}}\right)\right] + G_{\rm s}\sigma^2 + U_\Phi, \tag{6.24}$$

with

$$\mathcal{F}_{\rm f} = 1 + 3\Phi e^{-\beta E_{\rm q} + i\theta_{\rm f}} + 3\Phi^* e^{-2\beta E_{\rm q} + 2i\theta_{\rm f}} + e^{-3\beta E_{\rm q} + 3i\theta_{\rm f}}, \tag{6.25}$$

and $\theta_\pm = \theta_{\rm q} \pm \theta_{\rm iso}$. For imaginary $\mu_{\rm q}$, the expectation values of the Polyakov loop Φ and its conjugate Φ^* are complex conjugate to each other as shown in Sec. 5.5.1, so that $\mathcal{F}_{\bar{\rm f}}$ is complex conjugate to $\mathcal{F}_{\rm f}$. Following the discussion in Sec. 5.5.1, we show that the thermodynamic potential $\Omega_{\rm PNJL}$ is invariant under the

extended $\mathbb{Z}_3$ transformation

$$\theta_{\rm q} \to \theta_{\rm q} + 2\pi/3, \quad \Phi \to e^{-2\pi i/3}\Phi, \qquad \Phi^* \to e^{2\pi i/3}\Phi^*. \tag{6.26}$$

Using the modified Polyakov loop $\Psi = e^{i\theta_{\rm q}}\Phi$, which is invariant under the transformation (6.26), we can rewritten $\mathcal{F}_{\rm f}$ into

$$\mathcal{F}_{\rm f} = 1 + 3\Psi e^{-\beta E_{\rm q} + i\theta_{\rm iso}} + 3\Psi^* e^{-2\beta E_{\rm q} + 3i\theta_{\rm q} + 2i\theta_{\rm iso}} + e^{-3\beta E_{\rm q} + 3i\theta_{\rm q} + 3i\theta_{\rm iso}}. \tag{6.27}$$

Thus, the potential $\Omega_{\rm PNJL}$ is invariant under the extended $\mathbb{Z}_3$ transformation. Furthermore the potential is $\theta_{\rm iso}$-even and $\theta_{\rm q}$-even. Therefore the thermodynamic potential of the PNJL model has the same properties as that of QCD in (6.11)-(6.19). Particularly for $\theta_{\rm iso} = \pi/2$, T dependence of the potential is quite weak because the u-quark loop contribution to the thermal part of the potential is nearly canceled by the d-quark loop contribution. For $\theta_{\rm iso} = \pi/2$, the thermal part $\Omega^{\rm th}_{\rm PNJL}$ of $\Omega_{\rm PNJL}$ is rewritten into

$$\begin{aligned}
\Omega^{\rm th}_{\rm PNJL} &= -\frac{2}{\beta}\int \frac{d^3\mathbf{p}}{(2\pi)^3}\left[{\rm tr_c}\ln\left(1 + Le^{-\beta E_{\rm q} + i\theta_{\rm q} + i\pi/2}\right)\left(1 + Le^{-\beta E_{\rm q} + i\theta_{\rm q} - i\pi/2}\right) + {\rm h.c.}\right] \\
&= -\frac{2}{\beta}\int \frac{d^3\mathbf{p}}{(2\pi)^3}\left[{\rm tr_c}\ln\left(1 + L^2 e^{-2\beta E_{\rm q} + 2i\theta_{\rm q}}\right) + {\rm h.c.}\right],
\end{aligned} \tag{6.28}$$

where $L = e^{-i\beta A_4}$ is the Polyakov line and h.c. represents the Hermitian conjugate of the first term. The potential at $\theta_{\rm iso} = \pi/2$ thus becomes that at $\theta_{\rm iso} = 0$ under a transformation,

$$\ln\left(1 + L^2 e^{-2\beta E_{\rm q} + 2i\theta_{\rm q}}\right) \xrightarrow{T\to 2T,\ 2\theta_{\rm q}\to\theta_{\rm q}} \ln\left(1 + Le^{-\beta E_{\rm q} + i\theta_{\rm q}}\right). \tag{6.29}$$

This means that $\Omega_{\rm PNJL}$ has weak T and $\theta_{\rm q}$ dependences, and then the period in $\theta_{\rm q}$ is reduced from $2\pi/3$ to $\pi/3$.

6.3.3 $\theta_{\rm q}$ dependence

As discussed in Chapter 5, for $\theta_{\rm iso} = 0$ the RW phase transition occurs at $\theta_{\rm q} = (2k+1)\pi/3$ and $T \geq T_{\rm RW}$, where $T_{\rm RW}$ is the critical temperature of the endpoint

of the RW phase transition. $\theta_{\rm q}$-odd quantities such as the quark-number density $\rho_{\rm q} = -\partial\Omega_{\rm PNJL}/\partial\mu_{\rm q} = i\beta(\partial\Omega_{\rm PNJL}/\partial\theta_{\rm q})$ have finite values at $\theta_{\rm q} = (2k+1)\pi/3$ and $T \geq T_{\rm RW}$, so that they have a discontinuity there. It is important to show how the RW phase transition is affected by $\theta_{\rm iso}$. Figure 6.1 presents $\theta_{\rm q}$ dependence of the thermodynamic potential $\Omega_{\rm PNJL}$, the quark-number density $\rho_{\rm q}$ and the isospin density $\rho_{\rm iso} = -\partial\Omega_{\rm PNJL}/\partial\mu_{\rm iso} = i\beta(\partial\Omega_{\rm PNJL}/\partial\theta_{\rm iso})$ for three cases of $\theta_{\rm iso} = 0, \pi/2$ and π. Here temperature is taken to $T = 175$ and 250MeV that are below and above $T_{\rm RW}$, respectively. The potential $\Omega_{\rm PNJL}$ is real, $\theta_{\rm q}$-even and $\theta_{\rm iso}$-even, so that $\rho_{\rm q}$ and $\rho_{\rm iso}$ are purely imaginary. $\rho_{\rm q}$ is $\theta_{\rm q}$-odd and $\theta_{\rm iso}$-even, while $\rho_{\rm iso}$ is $\theta_{\rm q}$-even and $\theta_{\rm iso}$-odd. All the quantities have the RW periodicity. In the case of $\theta_{\rm iso} = 0$, for $T < T_{\rm RW}$, $\Omega_{\rm PNJL}$ and $\rho_{\rm q}$ are smooth everywhere, but not for $T \geq T_{\rm RW}$; the former (latter) has a cusp (discontinuity) at $\theta_{\rm q} = (2k+1)\pi/3$. This means that the RW phase transition occurs at $T \geq T_{\rm RW}$. Meanwhile, $\rho_{\rm iso}$ is zero for the two temperatures. It is found from (6.14) that the dot-dashed curves for $\theta_{\rm iso} = \pi$ are obtained by shifting the corresponding solid curves for $\theta_{\rm iso} = 0$ by $\pi/3$ in the $\theta_{\rm q}$ direction. For $\theta_{\rm iso} = \pi/2$, $\Omega_{\rm PNJL}$ is almost constant and $\rho_{\rm q}$ is then nearly zero, as expected from (6.28); precisely, they have a periodicity of $\pi/3$, but the $\theta_{\rm q}$ dependence is quite weak. In the insets of panels (a-2) and (b-2) where $\Omega_{\rm PNJL}$ and $\rho_{\rm q}$ are magnified for $\theta_{\rm iso} = \pi/2$. The quantities have a periodicity of $\pi/3$ in $\theta_{\rm q}$. The RW phase transition thus occurs at $\theta_{\rm q} = k\pi/3$. In contrast, the $\theta_{\rm iso}$-odd quantities such as $\rho_{\rm iso}$ have an anti-periodicity of π in $\theta_{\rm q}$,

$$\rho_{\rm iso}(\theta_{\rm q}, \pi/2) = -\rho_{\rm iso}(\theta_{\rm q}, \pi/2). \tag{6.30}$$

Figure 6.2 (a) presents $\theta_{\rm q}$ dependence of $\Omega_{\rm PNJL}$ for several cases of $\theta_{\rm iso} \in [0, \pi/2]$. The result shows that the RW phase transition occurs at $\theta_{\rm q} = (2k+1)\pi/3$ for $0 \leq \theta_{\rm iso} \leq \pi/2$. Figure 6.2 (b) represents the location of the RW phase transition in $\theta_{\rm q}$-$\theta_{\rm iso}$ plane for $T > T_{\rm RW}$. The RW phase transition occurs at $\theta_{\rm q} = (2k+1)\pi/3$ for $-\pi/2 \leq \theta_{\rm iso} \leq \pi/2$ because of the $\theta_{\rm iso}$-evenness of $\Omega_{\rm PNJL}$. Meanwhile the transition occurs at $\theta_{\rm q} = 2k\pi/3$ for $\pi/2 \leq \theta_{\rm iso} \leq 3\pi/2$ because of the relation (6.14).

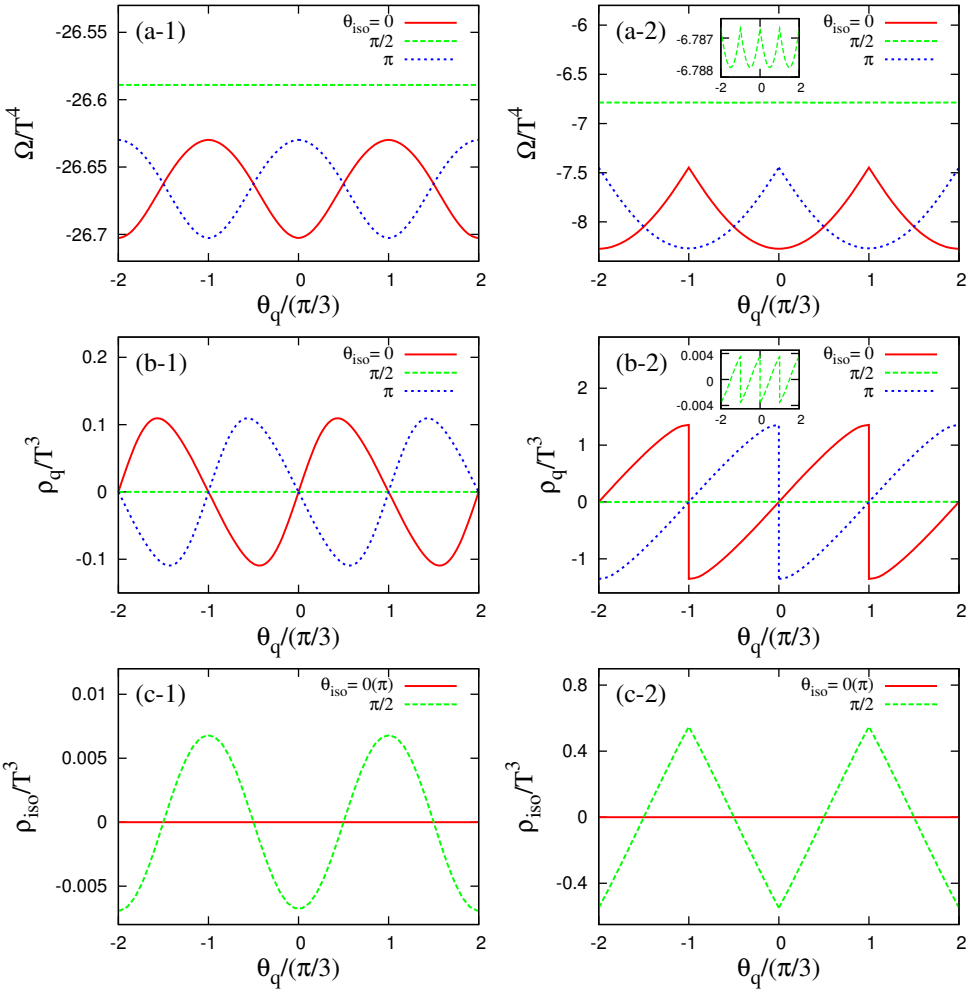

Figure 6.1: $\theta_{\rm q}$ dependence of (a-1) the thermodynamic potential $\Omega_{\rm PNJL}$, (b-1) the quark-number density $\rho_{\rm q}$ and (c-1) the isospin density $\rho_{\rm iso}$ at $T = 175$ MeV. Panels (a-2), (b-2) and (c-2) represent the same quantities as panels (a-1), (b-1) and (c-1) but for $T = 250$MeV. The solid, dashed and dotted curves correspond to three cases of $\theta_{\rm iso} = 0,\ \pi/2$ and π, respectively. In panels (c-1) and (c-2), the solid and dotted lines agree with the x axis. In the insets of panel (a-2) and (b-2), the y axis is magnified only for $\theta_{\rm iso} = \pi/2$.

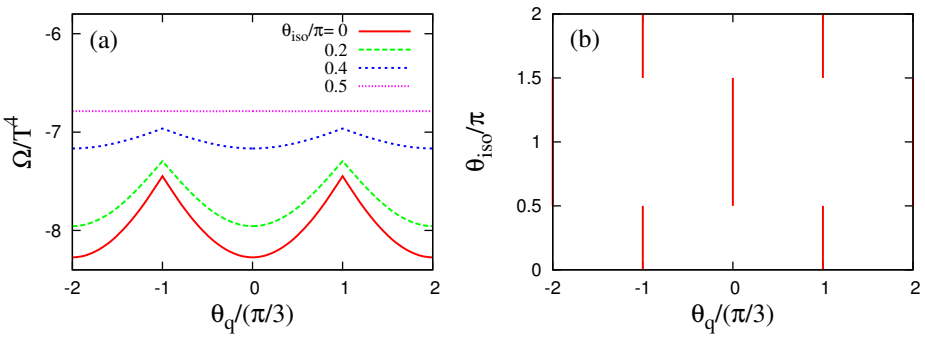

Figure 6.2: (a) $\theta_{\rm q}$ dependence of $\Omega_{\rm PNJL}$ for $\theta_{\rm iso}/\pi = 0$ (solid), 0.2 (dashed), 0.4 (dotted), and 0.5 (dot-dashed). (b) Phase diagram in $\theta_{\rm q}$-$\theta_{\rm iso}$ plane. The solid lines represent the RW phase transition. For both the panels, $T = 250$ MeV is taken.

6.3.4 $\theta_{\rm iso}$ dependence

Next, $\theta_{\rm iso}$ dependence of $\Omega_{\rm PNJL}$, $\rho_{\rm q}$ and $\rho_{\rm iso}$ is investigated. Since $\Omega_{\rm PNJL}$ is $\theta_{\rm iso}$-even with a periodicity of 2π,

$$\Omega_{\rm PNJL}(\theta_{\rm q}, \pi - \theta_{\rm iso}) = \Omega_{\rm PNJL}(\theta_{\rm q}, \theta_{\rm iso} - \pi) = \Omega_{\rm PNJL}(\theta_{\rm q}, \pi + \theta_{\rm iso}). \tag{6.31}$$

This means that $\theta_{\rm iso}$ dependence of $\Omega_{\rm PNJL}$ is symmetric with respect to the axis $\theta_{\rm iso} = \pi$. The quark-number density $\rho_{\rm q}$ is also $\theta_{\rm iso}$-even and hence has the same symmetry. In contrast, $\theta_{\rm iso}$-odd quantities such as $\rho_{\rm iso}$ are asymmetric with respect to the axis $\theta_{\rm iso} = \pi$:

$$\rho_{\rm iso}(\theta_{\rm q}, \pi - \theta_{\rm iso}) = -\rho_{\rm iso}(\theta_{\rm q}, \pi + \theta_{\rm iso}). \tag{6.32}$$

For $\theta_{\rm q} = \pi/6$, $\Omega_{\rm PNJL}$ has a periodicity of π in $\theta_{\rm iso}$, as expected from (6.19). The quark-number density $\rho_{\rm q}$ has then the same symmetry as $\Omega_{\rm PNJL}$ since it is $\theta_{\rm iso}$-even. In contrast, $\theta_{\rm iso}$-odd quantities such as $\rho_{\rm iso}$ have an anti-periodicity of π in $\theta_{\rm iso}$:

$$\rho_{\rm iso}(\pi/6, \theta_{\rm iso}) = -\rho_{\rm iso}(\pi/6, \theta_{\rm iso} + \pi). \tag{6.33}$$

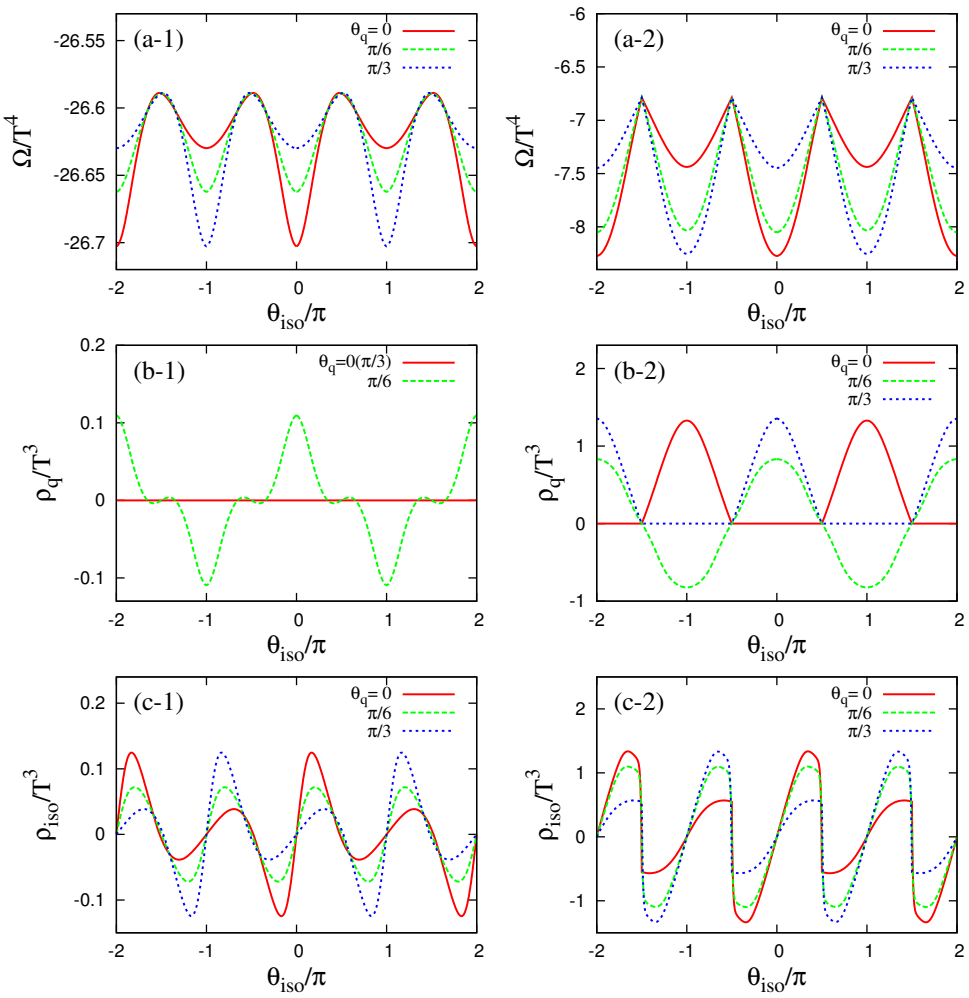

Figure 6.3: $\theta_{\rm iso}$ dependence of (a-1) the thermodynamic potential $\Omega_{\rm PNJL}$, (b-1) the quark-number density $\rho_{\rm q}$ and (c-1) the isospin density $\rho_{\rm iso}$ at $T = 175$MeV. Panels (a-2), (b-2) and (c-2) represent the same quantities as panels (a-1), (b-1) and (c-1) but for $T = 250$MeV. Three cases of $\theta_{\rm q} = 0, \pi/6$ and $\pi/3$ are taken. In panel (b), the solid for $\theta_{\rm q} = 0$ and the dotted line for $\theta_{\rm q} = \pi/3$ agree with the x axis.

Figure 6.3 presents $\theta_{\rm iso}$ dependence of $\Omega_{\rm PNJL}$, $\rho_{\rm q}$ and $\rho_{\rm iso}$ at $\theta_{\rm q} = 0, \pi/6$ and $\pi/3$ for the same temperature as Fig. 6.1. The quantities $\Omega_{\rm PNJL}$ and $\rho_{\rm q}$ are symmetric with respect to the axis $\theta_{\rm iso} = \pi$, while $\rho_{\rm iso}$ is asymmetric with respect to the axis. All the quantities have a periodicity of 2π in $\theta_{\rm iso}$ for all $\theta_{\rm q}$. For $\theta_{\rm q} = \pi/6$, $\Omega_{\rm PNJL}$ and $\rho_{\rm q}$ have a periodicity of π in $\theta_{\rm iso}$, while $\rho_{\rm iso}$ has an anti-periodicity of π in $\theta_{\rm iso}$. For $\theta_{\rm iso}$-even quantities, $\Omega_{\rm PNJL}$ and $\rho_{\rm q}$, all curves almost meet at $\theta_{\rm iso} = \pi/2$ and $3\pi/2$. In all the panels, the dotted curve for the case of $\theta_{\rm q} = \pi/3$ is obtained by shifting the solid one for the case of $\theta_{\rm q} = 0$ by π in the $\theta_{\rm iso}$ direction. For $T < T_{\rm RW}$, they are smooth everywhere in $\theta_{\rm iso}$. For $T \geq T_{\rm RW}$, however the $\theta_{\rm iso}$-even quantities such as $\Omega_{\rm PNJL}$ and $\rho_{\rm q}$ have cusps at $\theta_{\rm q} = (2k+1)\pi/2$, while the $\theta_{\rm iso}$-odd quantities such as $\rho_{\rm iso}$ have discontinuities there. These singular behaviors represent the boundary of the RW phase transition. For $\theta_{\rm q} = \pi/3$, $\rho_{\rm q}$ has a finite value at $-\pi/2 < \theta_{\rm iso} < \pi/2$. This means that the RW phase transition occurs there and $\rho_{\rm q}$ has a discontinuity there in the $\theta_{\rm q}$ direction. The RW phase transition also occurs at $\pi/2 < \theta_{\rm iso} < 3\pi/2$ for $\theta_{\rm q} = 0$ because of the relation (6.14).

6.3.5 Thermodynamics in the $\theta_{\rm q}$-$\theta_{\rm iso}$ plane

Figure 6.4 presents $\Omega_{\rm PNJL}$, $\rho_{\rm q}$ and $\rho_{\rm iso}$ in the $\theta_{\rm q}$-$\theta_{\rm iso}$ plane at $T = 175$ (left panel) and 250 MeV (right panel). The symmetries (6.11)-(6.19) are seen as a bird's eye view. This result is consistent with LQCD ones [31] as shown in Fig. 6.5. If the pion condensate were nonzero, the symmetries would break down as discussed in Sec. 6.4.1. Hence, the fact that LQCD has the symmetries means that the pion condensation does not occur also in the LQCD simulation.

6.3.6 Comparison of PNJL model with LQCD

LQCD has calculated the quark-number density $\rho_{\rm q}$ and the isospin density $\rho_{\rm iso}$ in the $\theta_{\rm q}$-$\theta_{\rm iso}$ plane, where the lattice size is $16^3 \times 4$ and the forth-rooted staggered fermion is taken [31]. Figure 6.5 shows LQCD results for the quark-number density $\rho_{\rm q}$ at (a) $T = 0.9T_{\rm c}$ and (b) $1.25T_{\rm c}$, and also for the isospin density $\rho_{\rm iso}$ at (c) $T = 0.9T_{\rm c}$ and (d) $1.25T_{\rm c}$, respectively. Note that the LQCD data at $T = 1.25T_{\rm c}$ is plotted in the region of $\theta_{\rm q}/\pi < 0.3$ and $\theta_{\rm iso}/\pi < 0.3$ and hence

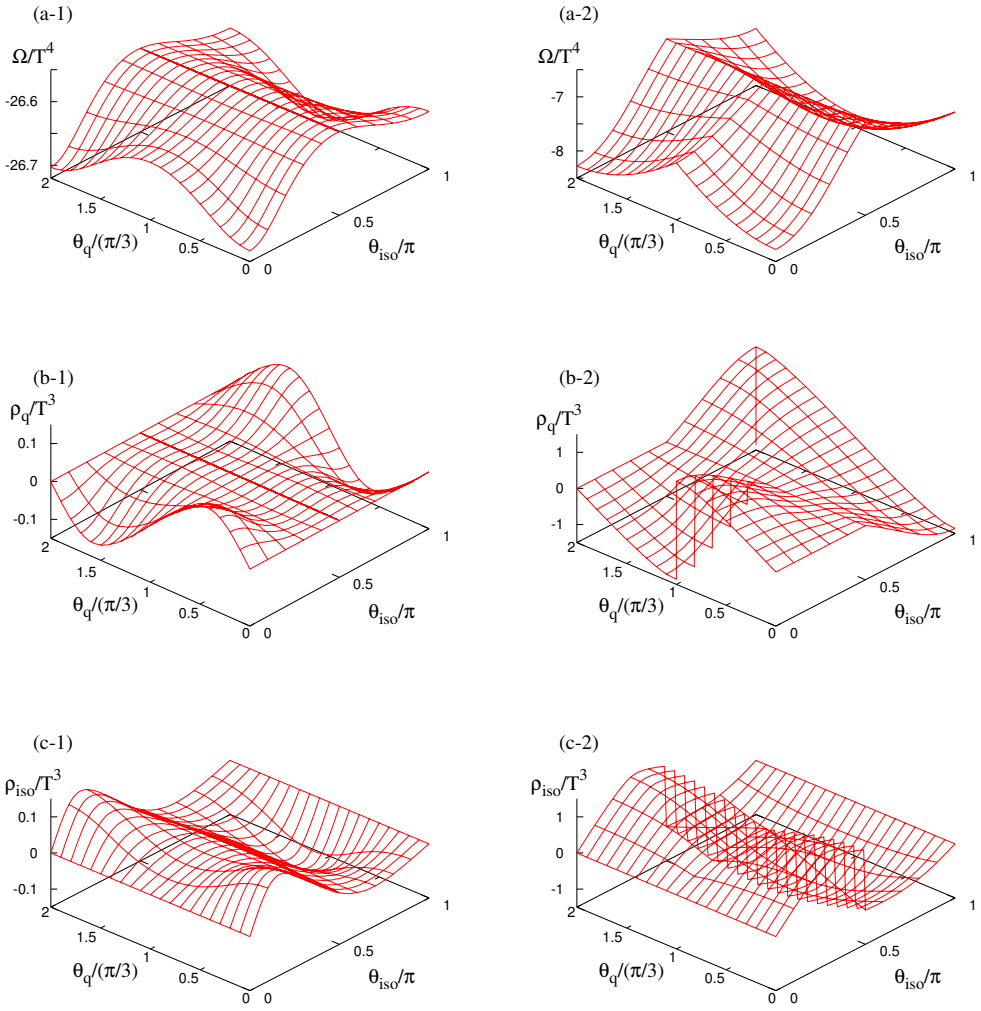

Figure 6.4: (a-1) the thermodynamic potential $\Omega_{\rm PNJL}$, the quark-number density$\rho_{\rm q}$ and the isospin density $\rho_{\rm iso}$ in the $\theta_{\rm q}$-$\theta_{\rm iso}$ plane at $T = 175$ MeV. Panels (a-2), (b-2) and (c-2) are the same quantities as (a-1), (b-1) and (c-1) at $T = 250$ MeV, respectively.

the RW phase transition is not seen. Figure 6.4 shows the PNJL results that are qualitatively consistent with the LQCD results. For $T \leq T_c$, the LQCD data in

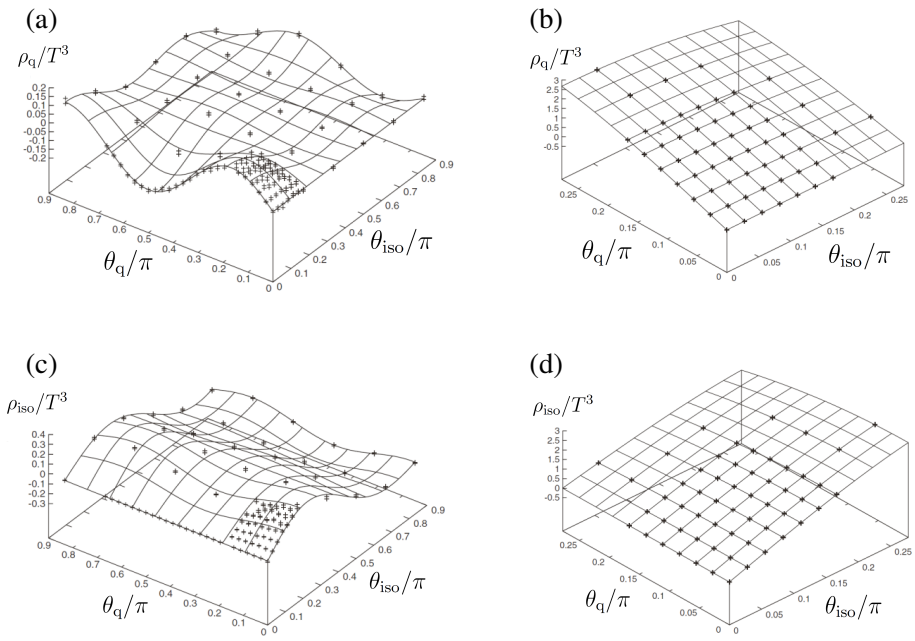

Figure 6.5: LQCD results for the quark-number density ρ_q at (a) $T = 0.9T_c$ and (b) $1.25T_c$, for the isospin density ρ_{iso} at (a) $T = 0.9T_c$ and (b) $1.25T_c$, respectively. The LQCD data is taken from Ref. [31].

Ref. [31] are fitted by a trigonometric function of the thermodynamic potential Ω:

$$\Omega/T^4 = -\sum_{N_q,N_{iso}} C_{N_q,N_{iso}}(T)\cos(3N_q\theta_q)\cos(N_{iso}\theta_{iso}) \times 10^{-3} \tag{6.34}$$

with the quark-number N_q and the isospin-number N_{iso}. The resultant values are summarized in Table 6.1. The quark-number density ρ_q and the isospin density ρ_{iso} are obtained by differentiating Ω with respect to θ_q and θ_{iso}, respectively. The parameters $C_{N_q,N_{iso}}$ are fitted to the LQCD data on ρ_q and ρ_{iso} in the θ_q-θ_{iso} plane. Figure 6.6 presents ρ_q/T^3 and ρ_{iso}/T^3 at $T = T_c$. The solid (dashed) lines stand for the PNJL (LQCD) results. In panels (a) and (b) where ρ_q/T^3 is

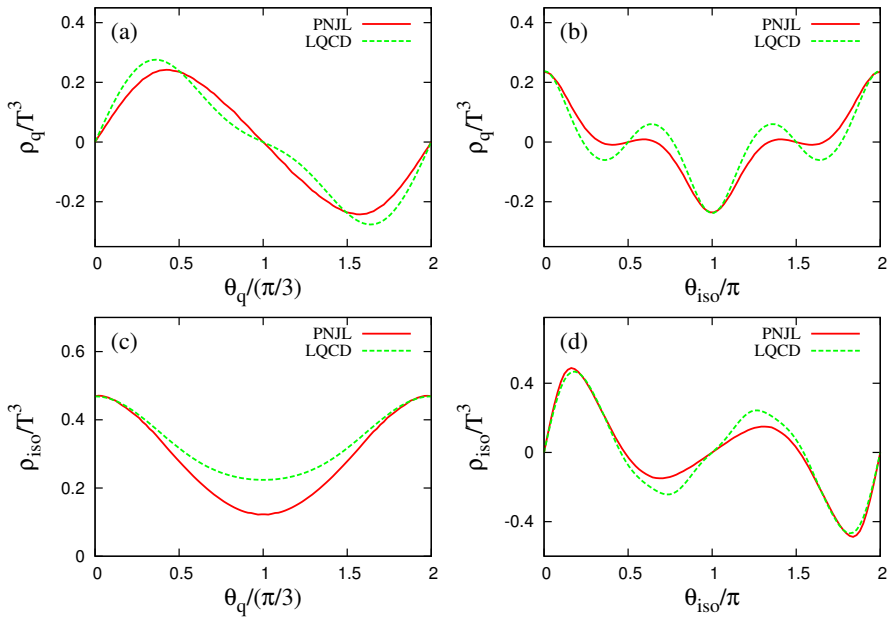

Figure 6.6: Comparison of the PNJL model with LQCD for $\rho_{\rm q}$ and $\rho_{\rm iso}$ at $T = T_{\rm c}$; (a) $\theta_{\rm q}$ dependence of $\rho_{\rm q}/T^3$ at $\theta_{\rm iso} = 0$, (b) $\theta_{\rm iso}$ dependence of $\rho_{\rm q}/T^3$ at $\theta_{\rm q} = \pi/6$, (c) $\theta_{\rm q}$ dependence of $\rho_{\rm iso}/T^3$ at $\theta_{\rm iso} = \pi/5$ and (d) $\theta_{\rm iso}$ dependence of $\rho_{\rm iso}/T^3$ at $\theta_{\rm q} = 0$. The solid (dotted) lines denote the PNJL (LQCD) results. The PNJL result is multiplied by 2.1 to fit the LQCD one at $(\theta_{\rm q}, \theta_{\rm iso}) = (\pi/6, 0)$ in panels (a) and (b) and by 3.8 to fit the HRG result at $(\theta_{\rm q}, \theta_{\rm iso}) = (0, \pi/5)$ in panels (c) and (d).

$C_{0,2}$	$C_{0,4}$	$C_{1,1}$	$C_{1,3}$	$C_{1,5}$	$C_{1,7}$	$C_{2,2}$	$C_{2,4}$
160.7	11	34.4	39.3	4.2	1.5	3.1	10

Table 6.1: Summary of the parameter set $C_{N_{\rm q},N_{\rm iso}}$ in fitting function (6.34) to LQCD data at $T = T_{\rm c}$ [31]. Note that the parameter has the constraint $N_{\rm q} \equiv N_{\rm iso}$ mod 2.

plotted, the PNJL result is adjusted to the LQCD one at $(\theta_{\rm q}, \theta_{\rm iso}) = (\pi/6, 0)$ by multiplying the PNJL result by 2.1. In panels (c) and (d) where $\rho_{\rm iso}/T^3$ is drawn, the PNJL result is fitted to the LQCD one at $(\theta_{\rm q}, \theta_{\rm iso}) = (0, \pi/5)$ by multiplying the PNJL result by 3.8. Oscillatory patterns of the LQCD results are reasonably reproduced by the PNJL model for $T \leq T_{\rm c}$. The success of the PNJL model for the oscillatory pattern may indicate that the pattern is essentially controlled by discrete symmetries (6.11)-(6.19). For the magnitudes, meanwhile, the PNJL model underestimates the LQCD results. Here we consider a possible origin of the discrepancy. In Fig. 6.7(a), $\rho_{\rm q}$ is plotted as a function of T for $\theta_{\rm q} = \pi/6$ and $\theta_{\rm iso} = 0$. At $T = 1.25T_{\rm c}$, LQCD data (open-circle symbol) is larger than the Stefan-Boltzmann high-T limit (thin-dotted curve), while the PNJL result (solid curve) is smaller than the limit at the same T. The PNJL model is considered to be reliable above $T_{\rm c}$ since quarks and gluons are dominant in the deconfinement phase. For real $\mu_{\rm q}$, actually the PNJL prediction on $\rho_{\rm q}$ is consistent with LQCD data evaluated by the Taylor expansion at $T > T_{\rm c}$[1]. We then normalize the LQCD data so that the data at $T = 1.25T_{\rm c}$ can agree with the PNJL result at $T = 1.25T_{\rm c}$. The normalized data are shown by filled-circle symbols. At $T = 0.951T_{\rm c}$ and $T_{\rm c}$, the PNJL result is smaller than the normalized data by a factor of about 2. This discrepancy is understandable as shown follow. Below $T_{\rm c}$, in general, hadronic excitations are important, but such an effect is not included in the mean field calculation of the PNJL model. The hadronic excitations are considered as free gas. This approximation is good for $T < T_{\rm c}$ where hadrons have no decay modes. In this approximation, the thermodynamic potential $\Omega_{\rm q+h}$

[1] We address this point in Sec. 7.3.

with hadronic excitations is

$$\Omega_{\rm q+h} = \Omega_{\rm q} + \Omega_{\rm m} + \Omega_{\rm b}. \tag{6.35}$$

The potential $\Omega_{\rm q}$ for quark is the same as $\Omega_{\rm PNJL}$ of the PNJL model in (6.24). The potential $\Omega_{\rm b}$ for baryons and that $\Omega_{\rm m}$ for the mesons are

$$\Omega_{\rm b} = -\frac{4}{\beta}\int \frac{d^3\mathbf{p}}{(2\pi)^3} \ln\left(1+e^{-\beta(E_{\rm b}-\mu_{\rm b})}\right)\left(1+e^{-\beta(E_{\rm b}-\mu_{\rm b})}\right), \tag{6.36}$$

$$\Omega_{\rm m} = -\sum_{{\rm m}=\pi_\pm,\pi_0} \frac{1}{\beta}\int \frac{d^3\mathbf{p}}{(2\pi)^3} \ln\left(1-e^{-\beta(E_{\rm m}-\mu_{\rm m})}\right), \tag{6.37}$$

where $E_{\rm b} = \sqrt{\mathbf{p}^2+M_{\rm b}^2}$, $E_{\rm m} = \sqrt{\mathbf{p}^2+M_{\rm m}^2}$ and $\mu_{\rm b} = 3\mu_{\rm q}$. The meson chemical potentials $\mu_{\rm m}$ are taken to $2\mu_{\rm iso}$, $-2\mu_{\rm iso}$ and 0 for π_+, π_- and π_0, respectively. Here we consider nucleons with the physical masses $M_{\rm b} = 940$MeV as baryons and pions with the mass $M_\pi = 280$MeV (the same value as the LQCD calculation [31]) as mesons. $\rho_{\rm q}$ and $\rho_{\rm iso}$ are obtained by differentiating $\Omega_{\rm q+h}$ with respect to $\mu_{\rm q}$ and $\mu_{\rm iso}$, respectively. The new $\rho_{\rm q}$ is plotted by the dashed line up to $T_{\rm c}$. This line agrees with the normalized LQCD data at $T = 0.951T_{\rm c}$ and $T_{\rm c}$. The same

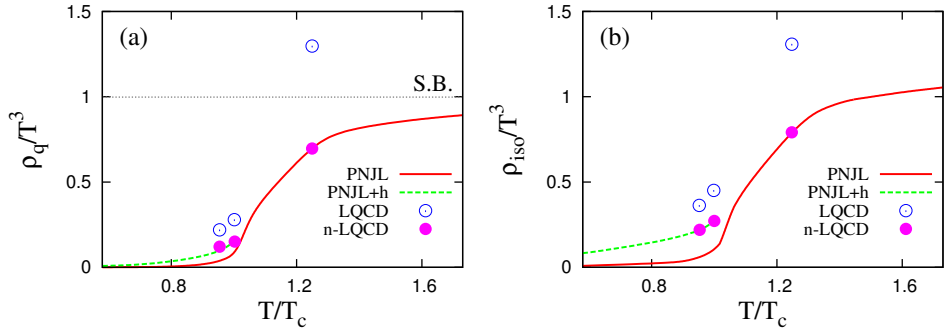

Figure 6.7: T dependence of (a) $\rho_{\rm q}$ at $(\theta_{\rm q}, \theta_{\rm iso}) = (\pi/6, 0)$ and (b) $\rho_{\rm iso}$ at $(\theta_{\rm q}, \theta_{\rm iso}) = (0, \pi/5)$. LQCD data are taken from [31]. The original values of LQCD data are plotted by open-circle symbols. The LQCD data are normalized so as to reproduce the PNJL result at $T = 1.25T_{\rm c}$. The normalized LQCD (n-LQCD) data are shown by filled-circle symbols. The dashed line is the result of the PNJL model with the hadronic excitations. The dot-dashed line represents $\rho_{\rm q}$ in the Stefan-Boltzmann limit.

analysis is possible for $\rho_{\rm iso}$. Figure 6.7(b) presents $\rho_{\rm iso}$ as a function of T for $\theta_{\rm q} = 0$ and $\theta_{\rm iso} = \pi/5$. At $T = 1.25T_{\rm c}$, LQCD data (open-circle symbol) is larger than the PNJL result by a factor of 1.5. Hence the data are normalized so that the data at $T = 1.25T_{\rm c}$ can reproduce the corresponding PNJL result as shown by filled-circle symbols. At $T = 0.951T_{\rm c}$ and $T_{\rm c}$, the PNJL result (solid curve) underestimates the normalized LQCD data. By considering the hadronic excitations, the new PNJL result (dashed curve) agrees with LQCD data.

6.3.7 Phase diagram in $\theta_{\rm iso}$-T plane

Figure 6.8 presents T dependence of the absolute value $|\Phi|$ of the Polyakov loop (dashed curve) and the chiral condensate σ (solid curve) at $\theta_{\rm q} = 0$. The bold (thin) curve shows the case of $\mu_{\rm iso} = \pi/2$ (0). For $\theta_{\rm iso} = 0$, both the chiral and the deconfinement transition are crossover. The pseudo-critical temperatures are $T_{\rm c}^{\sigma} = 216$MeV for the chiral transition and $T_{\rm c}^{\Phi} = 173$MeV for the deconfinement transition in the PNJL model, while $T_{\rm c}^{\sigma} \approx T_{\rm c}^{\Phi} = 173 \pm 8$MeV in LQCD [52]. Thus, the correlation between the two transitions is weaker in the PNJL model than in LQCD. For $\theta_{\rm iso} = \pi/2$, the deconfinement phase transition becomes first

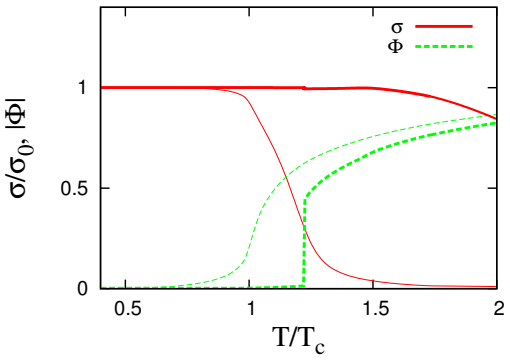

Figure 6.8: T dependence of $|\Phi|$ (dashed) and σ (solid) normalized by that σ_0 at vacuum. The bold (thin) curves correspond to the case of $\theta_{\rm iso} = \pi/2$ (0).

order, while the chiral condensate hardly depends on T. As shown in (6.28), the u-quark loop contribution to Ω is nearly canceled out by the d-quark one for $\theta_{\rm iso} = \pi/2$. As a consequence of this cancellation in Ω, σ has a weak T dependence, while T dependence of Φ is controlled by the pure gauge part, that

is the Polyakov potential U_Φ in (6.20). Eventually, T_c^Φ is much smaller than T_c^σ. Since 2-flavor LQCD data are not available at $\theta_{\rm iso} = \pi/2$, it is not clear whether the large difference is realistic. However, it should be noted that, in the 8-flavor case, LQCD data [52] shows that the chiral and deconfinement transitions occur the same temperature $T_c^\sigma \approx T_c^\Phi$ and they are first order. This inconsistency of the PNJL results with the LQCD data is originated in the fact that the correlation between the two order parameters, σ and Φ, is weak in the PNJL model. This problem of the PNJL model is addressed in the next chapter. Figure 6.9 shows

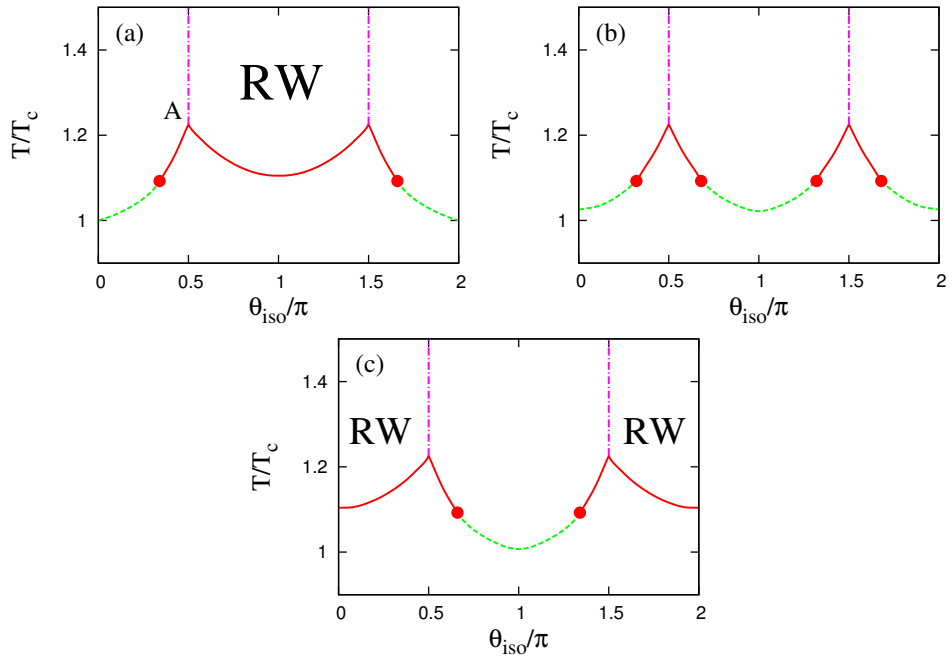

Figure 6.9: Phase diagram of the deconfinement phase transition in $\theta_{\rm iso}$-T plane. Panels (a), (b) and (c) are the cases of $\theta_{\rm q} = 0, \pi/6$ and $\pi/3$ respectively. The first-order (crossover) transition is denoted by the solid (dashed) curves. The area labeled by "RW" between the two dot-dashed lines represents the region in which the RW phase transition occurs. Point A is located at $(T_{\rm A}, \theta_{\rm A}) = (212{\rm MeV}, 0.494\pi)$.

the phase diagram of the deconfinement phase transition in the $\theta_{\rm iso}$-T plane, where panels (a), (b) and (c) correspond to three cases of $\theta_{\rm q} = 0, \pi/6$ and $\pi/3$, respectively. The solid curves denote the first-order phase transition, while the dashed lines stand for the crossover transition. Near $\theta_{\rm iso} = (2k+1)\pi/2$, the

deconfinement phase transition are first-order in all the cases. Near $\theta_{\rm iso} = k\pi$, the deconfinement phase transition is first-order at $\theta_{\rm q} = 0$, but crossover at $\theta_{\rm q} = \pi/6$ and $\pi/3$. The critical endpoint of the first-order transition represented by the red-circle symbol moves to $\theta_{\rm iso} = 0$ when $\theta_{\rm q}$ increases from 0 to $\pi/3$. The RW phase transition occurs in the area labeled by "RW" between the two dot-dashed lines. The dot-dashed line is a boundary of the area. It is a nearly-vertical line starting from point A and is expressed as $\theta_{\rm iso} = \pi/2 - \Delta(T)$ where $\Delta(T)$ slightly depends on T as $\Delta(T) = 0.16(T/T_{\rm c}) - 0.23$ for $T \geq 1.23T_{\rm c}$. Point A is located at $(T_{\rm A}, \theta_{\rm A}) = (1.23T_{\rm c}, 0.494\pi)$ in the 2-flavor PNJL model, while 8-flavor LQCD data [31] show $(T_{\rm A}, \theta_{\rm A}) = (1.2T_{\rm c}, 0.48\pi)$. The PNJL result is thus consistent with the LQCD data.

6.4 Real isospin chemical potential

In this section, we investigate the real isospin chemical potential $\mu_{\rm iso}$ region. The physical motivation to study QCD in this region is related to the physics of compact stars, isospin asymmetric nuclear matter and heavy-ion collisions at intermediate energies. For real $\mu_{\rm iso}$, the charged pion condensate occurs at high $\mu_{\rm iso}$ as shown in Sec. 6.3.2 by using the chiral perturbation theory. LQCD calculation shows that there is a phase transition from the normal phase to the pion superfluidity at a critical isospin chemical potential which is about half the pion mass at vacuum [51]. The QCD phase structure at real $\mu_{\rm iso}$ is also investigated in many low energy effective models such as the chiral perturbation theory [54], the NJL model [55] and the PNJL model [56]. Here we review properties of the phase transition at real $\mu_{\rm iso}$ by using the PNJL model.

6.4.1 Chiral and Pion Condensates

The thermodynamic potential $\Omega_{\rm PNJL}$ of the PNJL model is obtained in (6.21) in the mean field approximation. First we analytically show in the PNJL model that the critical isospin chemical potential for pion superfluidity is exactly half the pion mass at vacuum, i.e., $\mu_{\rm iso} > M_\pi/2$. The PNJL model is reduced to the NJL model at $T = 0$ and the gap equations for the chiral and pion condensates

are obtained as

$$\frac{\partial\Omega_{\rm PNJL}}{\partial\sigma} = 2G_{\rm s}\left[\sigma + 6M_{\rm q}\int\frac{d^3\mathbf{p}}{(2\pi)^3}\frac{1}{E}\left(\frac{E-\mu_{\rm iso}}{E_-}+\frac{E+\mu_{\rm iso}}{E_+}\right)\right] = 0, \quad (6.38)$$

$$\frac{\partial\Omega_{\rm PNJL}}{\partial\pi} = 2G_{\rm s}\pi\left[1 - 12G_{\rm s}\int\frac{d^3\mathbf{p}}{(2\pi)^3}\left(\frac{1}{E_-}+\frac{1}{E_+}\right)\right] = 0. \quad (6.39)$$

where $E_\pm = \sqrt{(E_{\rm q}\pm\mu_{\rm iso})^2 + N^2}$ with $N = 2G_{\rm s}\pi$. It is clear that $\pi = 0$ is always a solution of the gap equation (6.39) and σ is $\mu_{\rm q}$- and $\mu_{\rm iso}$-independent for $\pi = 0$. At the critical isospin chemical potential $\mu_{\rm iso}^{\rm c}$ where the pion condensate occurs, the solution $\pi = 0$ should satisfies the equation

$$1 - 24G_{\rm s}\int\frac{d^3\mathbf{p}}{(2\pi)^3}\frac{1}{E_{\rm q}^2 - (\mu_{\rm iso}^{\rm c})^2} = 0. \quad (6.40)$$

Meanwhile the pion mass at vacuum satisfies the condition

$$\left.\frac{\partial^2\Omega_{\rm PNJL}}{\partial\pi(q)\partial\pi(-q)}\right|_{q=M_\pi} = 1 - 24G_{\rm s}\int\frac{d^3\mathbf{p}}{(2\pi)^3}\frac{1}{E_{\rm q}^2 - M_\pi^2/4} = 0. \quad (6.41)$$

Therefore when the isospin chemical potential $\mu_{\rm iso}$ exceeds half the pion mass M_π at vacuum, the pion condensate occurs and the phase transition is second order. Figure 6.10 (a) shows the chiral σ (solid curve) and the pion condensates π (dashed curve) as a function of $\mu_{\rm iso}$ at $T = \mu_{\rm q} = 0$. The pion condensate occurs at $\mu_{\rm iso} > M_\pi/2$ and the phase transition is second order as expected. The chiral and pion condensates do not change at $\mu_{\rm iso} < M_\pi/2$. The former (latter) decreases (increases) as $\mu_{\rm iso}$ increases at $\mu_{\rm iso} > M_\pi/2$. Figure 6.10 (b) shows the isospin density $\rho_{\rm iso}$ as a function of $\mu_{\rm iso}$ at $T = \mu_{\rm q} = 0$. The isospin density is scaled by the normal nuclear density $\rho_0 = 0.17$ fm^{-3}. The isospin density $\rho_{\rm iso}$ at $T = \mu_{\rm q} = 0$ is

$$\rho_{\rm iso} = -\frac{\partial\Omega_{\rm PNJL}}{\partial\mu_{\rm iso}} = 3\int\frac{d^3\mathbf{p}}{(2\pi)^3}\left[\frac{E_{\rm q}+\mu_{\rm iso}}{E_+} - \frac{E_{\rm q}-\mu_{\rm iso}}{E_-}\right] \quad (6.42)$$

At $\mu_{\rm iso} < M_\pi/2$, the ground state does not change and the isospin density is zero. At $\mu_{\rm iso} > M_\pi/2$, $\rho_{\rm iso}$ increases monotonously with $\mu_{\rm iso}$. This nonzero net isospin density is due to the Bose-Einstein condensation of the charged pion. Figure 6.11

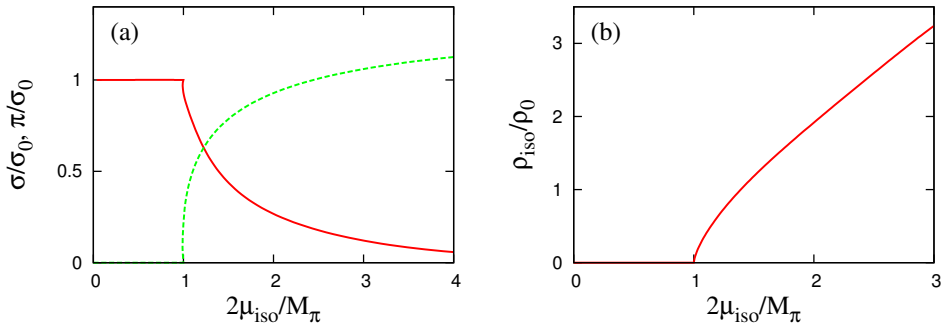

Figure 6.10: (a) The chiral σ (solid) and pion condensates π (dashed), normalized by the chiral condensate σ_0 at vacuum, as function of $\mu_{\rm iso}$ at $T = \mu_{\rm q} = 0$. (b) The isospin density $\rho_{\rm iso}$, normalized by the normal nuclear density ρ_0, as a function of $\mu_{\rm iso}$ at $T = \mu_{\rm q} = 0$.

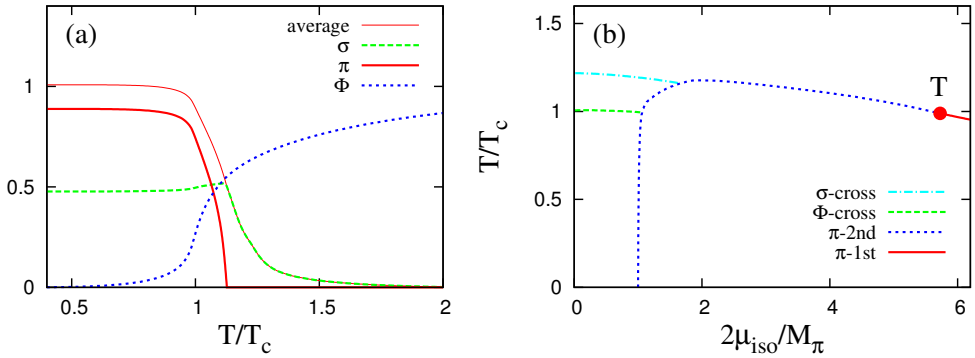

Figure 6.11: (a) The chiral σ (dashed) and pion condensates π (solid), normalized by the chiral condensate σ_0 at vacuum, as functions of T at $\mu_{\rm iso}$=100 MeV and $\mu_{\rm q} = 0$. The thin-solid and dotted lines represent the averaged condensate $\sqrt{\sigma^2+\pi^2}/\sigma_0$ and the Polyakov loop Φ. (b) Phase diagram in the $\mu_{\rm iso}$-T plane at $\mu_{\rm q} = 0$. The solid (dotted) curve represents a first-order (second-order) pion-superfluidity phase transition. Point T is the tricritical point. The dashed (dot-dashed) line means a deconfinement (chiral) crossover transition.

(a) shows the chiral and pion condensates as a function of T at $\mu_{\rm iso} = 100$MeV. For $\mu_{\rm iso} > M_\pi/2$, the pion condensate occurs at low temperature, then drops down due to the temperature effect, and finally disappears at a critical temperature $T_{\rm c}(\mu_{\rm iso})$. As the case for the BCS theory of superconductivity, the critical temperature $T_{\rm c}(\mu_{\rm iso})$ and the pseudo-gap $|N| = |2G_{\rm s}\pi|$ for the pion condensate at $T = 0$ satisfy the linear relation

$$T_{\rm c}(\mu_{\rm iso}) \sim \frac{\sqrt{3}}{\pi}|N|(T = 0, \mu_{\rm iso}). \tag{6.43}$$

For low temperature, the relative strength of the two condensates, σ and π, depends on $\mu_{\rm iso}$, $\sigma > \pi$ at small $\mu_{\rm iso}$ and $\sigma < \pi$ at large $\mu_{\rm iso}$. The averaged condensate $\sqrt{\sigma^2 + \pi^2}$ (the thin-solid curve), however, has a weak dependence on $\mu_{\rm iso}$ for $\mu_{\rm iso} < 2M_\pi$.

6.4.2 Phase diagram

Figure 6.11 (b) shows the phase diagram at real $\mu_{\rm iso}$. The solid (dotted) curve shows the first-order (second-order) pion-superfluidity phase transition. Point T located at $(\mu_{\rm iso}, T) = (0.32\ \text{GeV}, 0.169\ \text{GeV})$ is the tricritical point. The dashed (dot-dashed) line stands for a deconfinement (chiral) crossover transition. There is a sizable difference between the two crossover transitions in the PNJL model, whereas they agree with each other in LQCD. Thus, the correlation between the two transitions is weaker in the PNJL model than in LQCD also for real $\mu_{\rm iso}$.

6.5 Summary

We have investigated the isospin chemical potential $\mu_{\rm iso}$ region by using the PNJL model. Lattice QCD (LQCD) is free from the sign problem at real and imaginary $\mu_{\rm iso}$ and hence LQCD data are available there. So the PNJL model can be tested at real and imaginary $\mu_{\rm iso}$ by comparing of the model with LQCD results. First we have considered the case that both $\mu_{\rm iso}$ and $\mu_{\rm q}$ are purely imaginary. At imaginary $\mu_{\rm iso}$, the charged pion condensate does not occurs and hence QCD has the isospin symmetry. This situation is true even if the imaginary $\mu_{\rm q}$ is added.

At imaginary $\mu_{\rm q}$, QCD has the extended $\mathbb{Z}_3$ symmetry, i.e., the Roberge-Weiss periodicity. As a consequence, at imaginary $\mu_{\rm iso} = i\theta_{\rm iso}/\beta$ and $\mu_{\rm q} = i\theta_{\rm q}/\beta$, the QCD partition function has higher symmetries as (6.11)-(6.19). The PNJL model possesses all the symmetries. As a consequence of this property, the PNJL results are qualitatively consistent with LQCD results. Furthermore we made quantitative comparison of the PNJL model with LQCD data. As for the quark-number and isospin densities, the PNJL result in the mean field approximation underestimates the LQCD result because the hadronic excitations are neglected in the approximation. By considering the hadronic excitations as a free-gas approximation, the PNJL result with the hadronic excitations reproduces the LQCD results at low temperature. Thus the PNJL model is useful at imaginary $\mu_{\rm iso}$ and $\mu_{\rm q}$. The PNJL model predicts the phase diagram in the $\theta_{\rm q}$-$\theta_{\rm iso}$-T space. The RW phase transition occurs at $\theta_{\rm q} = (2k+1)\pi/3$ when $-\pi/2 < \theta_{\rm iso} < \pi/2$, while at $\theta_{\rm q} = 2\pi k/3$ when $\pi/2 < \theta_{\rm iso} < 3\pi/2$. The chiral and deconfinement transitions occur at different temperatures in the PNJL model, while the two transitions occur at the same temperature in LQCD. Thus the correlation between the two transitions is weaker in the PNJL model than in LQCD. Second we have considered the real $\mu_{\rm iso}$ region. At real $\mu_{\rm iso}$, the charged pion condensate occurs when $\mu_{\rm iso}$ is larger than half the pion mass M_π at vacuum. The phase transition is seen in LQCD. The PNJL model reproduces the pion-superfluidity phase transition at $\mu_{\rm iso} > M_\pi/2$. The chiral and deconfinement transitions also occur at different temperatures in the PNJL model, whereas the two transitions take place at the same temperature in LQCD. Throughout all the analyses in the regions of imaginary $\mu_{\rm q}$, imaginary $\mu_{\rm iso}$ and real $\mu_{\rm iso}$, the PNJL model reproduces LQCD results qualitatively. However, there is a sizable difference between the PNJL results and the LQCD data for the coincidence of the chiral and deconfinement transitions. Two transitions coincide with each other in LQCD, but in the PNJL model. In the next chapter, we address this problem.

Chapter 7

Entanglement PNJL model

We extend the PNJL model by introducing an effective four-quark vertex depending on the Polyakov loop. The effective vertex generates entanglement interactions between the Polyakov loop and the chiral condensate. The new model is consistent with lattice QCD data at imaginary quark chemical potential and real and imaginary isospin chemical potentials, particularly on strong correlation between the chiral and deconfinement transitions. We investigate the influence of the entanglement interactions on the location of the critical endpoint at real quark chemical potential. This chapter is based on our papers [57].

7.1 Purpose

An important query on the thermodynamics of quantum chromodynamics (QCD) is whether the chiral-symmetry restoration and the confinement-to-deconfinement transition take place simultaneously or not. If the two transitions do not coincide, phases such as the constituent quark phase [58] or the quarkyonic phase [59] may appear. If the chiral and deconfinement transitions are first-order, discontinuities appear simultaneously in their order parameters, that is, the chiral condensate σ and the Polyakov loop Φ [60]. Furthermore, if a nontrivial critical endpoint (CEP) exists at finite temperature (T) and quark chemical potential $\mu_{\rm q}$, susceptibilities of σ, Φ and other quantities diverge simultaneously [61]. This indicates a coincidence of second-order phase transitions. At zero $\mu_{\rm q}$, the chiral and de-

confinement transitions are found to be crossover [38; 39; 62]. Hence, there is no a priori reason why the two transitions coincide exactly. Actually, in lattice QCD (LQCD) simulations at zero $\mu_{\rm q}$, there is a debate as to whether the transitions really coincide or not [63]. LQCD simulations are far from perfection at real $\mu_{\rm q}$ because of the sign problem. Fortunately, LQCD data are available at imaginary $\mu_{\rm q}$ and real and imaginary isospin chemical potential $\mu_{\rm iso}$, since LQCD has no sign problem there. The LQCD data show that chiral and deconfinement crossover transitions coincide within the numerical accuracy [38; 39]. Since there is no general reason for coincidence between crossover transitions, it is natural to think that the chiral and deconfinement crossover transitions nearly coincide as a result of strong correlation (entanglement) between σ and Φ. An approach complementary to first-principle LQCD with the sign problem is to build an effective model consistent with LQCD data and apply the model to the real $\mu_{\rm q}$ region. The PNJL model is designed to treat both the chiral-symmetry restoration and the deconfinement transition [64]. The model well reproduces LQCD results qualitatively at imaginary $\mu_{\rm q}$, real and imaginary $\mu_{\rm iso}$ as shown in Chapters 5 and 6. In the PNJL model, however the correlation between σ and Φ is weak, so that the chiral and deconfinement crossover transitions do not coincide. This fact indicates that a true correlation between σ and Φ is stronger than that in the PNJL model appearing through the covariant derivative between quark and gauge fields. Actually, recent analyses [65] based on the exact renormalization-group equation [66] indicate that entanglement interactions between σ and Φ appear in addition to the original entanglement through the covariant derivative. In this chapter, we extend the PNJL model by introducing an effective four-quark vertex depending on Φ. The effective vertex generates entanglement interactions between σ and Φ. The new model is consistent with all LQCD data at imaginary $\mu_{\rm q}$ and real and imaginary $\mu_{\rm iso}$. Furthermore the model is consistent with LQCD data evaluated by the Taylor expansion at small real $\mu_{\rm q}$. We also analyze the influence of the entanglement interactions on the location of the critical endpoint (CEP) in the real $\mu_{\rm q}$ region.

7.2 Entanglement PNJL model

We start with the standard two-flavor PNJL Lagrangian

$$\mathcal{L} = \bar{q}(\gamma_\nu D_\nu + m_0)q - G_{\rm s}[(\bar{q}q)^2 + (\bar{q}i\gamma_5\vec{\tau}q)^2] + U_\Phi, \tag{7.1}$$

where q denotes the quark field, m_0 denotes the current quark mass, and $D_\nu = \partial_\nu + iA_4\delta_{4\nu}$. In the NJL sector, $G_{\rm s}$ denotes the coupling constant of the scalar-type four-quark interaction. The PNJL model succeeds to reproduce LQCD data qualitatively in the regions with no sign problem, i.e., imaginary $\mu_{\rm q}$, real and imaginary $\mu_{\rm iso}$ regions as shown in Chapters 5 and 6. Particularly, for imaginary $\mu_{\rm q} = i\theta_{\rm q}/\beta$, the success comes from the fact that the PNJL model has the extended $\mathbb{Z}_3$ symmetry,

$$\theta_{\rm q} \to \theta_{\rm q} + 2\pi/3, \quad \Phi \to e^{-2\pi i/3}\Phi, \quad \Phi^* \to e^{2\pi i/3}\Phi^*. \tag{7.2}$$

The partition function $Z(\theta_{\rm q})$ has the extended $\mathbb{Z}_3$ symmetry, and hence quantities invariant under the extended $\mathbb{Z}_3$ transformation have the Roberge-Weiss (RW) periodicity. At the present stage, the PNJL model is only a realistic effective model that possesses both extended $\mathbb{Z}_3$ symmetry and chiral symmetry. Furthermore, the PNJL model can reproduce the RW phase transition that occurs at $\theta_{\rm q} = \pi/3 \mod 2\pi/3$ when T is larger than some critical temperature $T_{\rm RW}$. This property makes it possible to compare PNJL results with LQCD data quantitatively at imaginary $\mu_{\rm q}$. However, the PNJL model is inconsistent with LQCD in which the chiral and deconfinement crossover transitions do not coincide with each other in all the regions with no sign problem. For example, at $\mu_{\rm q} = \mu_{\rm iso} = 0$, the critical temperature T_Φ (T_σ) of the deconfinement (chiral) transition is 173 (216) MeV. The relative difference $\Delta = |T_\sigma - T_\Phi|/T_\sigma$ is about 20 %, while LQCD simulations [67] show that $T_\sigma \simeq T_\Phi \simeq 173 \pm 8$ MeV there. The sizable difference indicates that the entanglement between the chiral and deconfinement transitions is weak in the PNJL model. In order to solve this problem, we propose an effective coupling depending on the Polyakov loop, $G_{\rm s}(\Phi)$. The origin of the four-quark vertex $G_{\rm s}$ is the one-gluon exchange between two quarks and its higher-order interactions. If the gluon field A_ν has a vacuum expectation

value $\langle A_4 \rangle$ in its temporal component, A_ν is coupled to $\langle A_4 \rangle$ which is related to the Polyakov loop $\Phi[A_4]$; see Fig. 7.1 for the diagrammatic description. Hence, $G_{\rm s}$ is changed into an effective vertex $G_{\rm s}(\Phi)$ depending on Φ [65]. It is expected that the Φ dependence of $G_{\rm s}(\Phi)$ is determined in the future by an exact method such as the exact renormalization-group equation [66]. In this chapter, however, we simply assume the following $G_{\rm s}(\Phi)$ that preserves the extended $\mathbb{Z}_3$ symmetry and charge-conjugation symmetry:

$$G_{\rm s}(\Phi) = G_{\rm s}[1 - \alpha_1 \Phi\Phi^* - \alpha_2(\Phi^3 + \Phi^{*3})]. \tag{7.3}$$

This model thus has entanglement interactions between σ and Φ in addition to the covariant derivative in the original PNJL model. The PNJL model with the entanglement vertex $G_{\rm s}(\Phi)$ is referred to as entanglement-PNJL (EPNJL) model. The strengths, α_1 and α_2, of the entangle vertex are determined from LQCD data

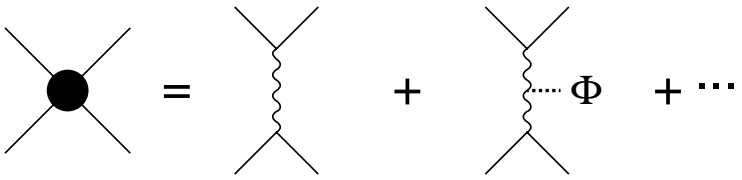

Figure 7.1: The diagrammatic description of the effective vertex $G_{\rm s}(\Phi)$.

at imaginary $\mu_{\rm q}$, and the validity of the model setting is confirmed for real and imaginary $\mu_{\rm iso}$, small real $\mu_{\rm q}$ by comparing the model results with LQCD data. The EPNJL model is consistent with LQCD data in all the regions with no sign problem.

7.3 Comparison with LQCD

In this section, we consider the three regions where LQCD data are available, i.e., the imaginary $\mu_{\rm q}$, real and imaginary $\mu_{\rm iso}$ regions. In the EPNJL model, we take the parameter $(\alpha_1, \alpha_2) = (0.2, 0.2)$ in the entangle vertex and rescale T_0 from 212 MeV to 190 MeV so as to reproduce LQCD data at imaginary $\mu_{\rm q}$, while the other parameters keep the same values as the original PNJL model. The

model can reproduce two phenomena simultaneously; one is the strong correlation between the deconfinement and chiral transitions and the other is the quark-mass dependence of the order of the Roberge-Weiss endpoint predicted by LQCD very recently [68]. The coincidence and the m_0 dependence are preserved in the parameter region $\alpha_1, \alpha_2 \approx 0.20 \pm 0.05$.

7.3.1 Imaginary quark chemical potential

First, we consider the thermal system with no chemical potential. Figure 7.2 shows the chiral condensate normalized by the value σ_0 at vacuum and the Polyakov loop Φ as a function of T. The dotted curves represent the PNJL results. LQCD data [67] are also plotted by plus (+) and cross (×) symbols for σ and Φ, respectively. The LQCD data has 10% error since LQCD calculations have the error in determining T_c [67]. For Φ the PNJL result reasonably agrees with the LQCD data. For σ, however, the PNJL result considerably overshoots the LQCD data. The EPNJL model is consistent with the LQCD data for both the chiral condensate and the Polyakov loop. Figure 7.3 represents chiral and Polyakov-loop susceptibilities, χ_σ and χ_Φ, as a function of T. For the PNJL model presented in Panel (a), the peak position of χ_σ, i.e., the critical temperature T_σ of the chiral transition, is much larger than the peak position of χ_Φ, that is, the critical temperature T_Φ of the deconfinement transition: $T_\sigma \gg T_\Phi$. For the EPNJL model presented in Panel (b), the two transitions coincide with each other, $T_\sigma = T_\Phi$. The entanglement vertex $G_s(\Phi)$ thus makes the correlation between the chiral restoration and the deconfinement transition stronger, as expected. Next, we consider the thermal system with imaginary $\mu_q = i\theta_q/\beta$. The formalism of the PNJL model at imaginary μ_q is shown in Chapter 5. The thermodynamic potential of the EPNJL model is obtained with G_s replaced by $G_s(\Phi)$ in the potential (5.9) of the PNJL model. Figure 7.4 presents T dependence of σ and the absolute value of Φ at $\theta_q = \pi/3$. In the PNJL model, the deconfinement transition at $T = 190$ MeV is first-order, while the chiral transition is crossover at $T = 265$MeV; σ has a small jump at $T = 190$ MeV, but it is just a discontinuity induced by the first-order deconfinement transition in $|\Phi|$. In the EPNJL model, the deconfinement transition at $T = 185$ MeV is very

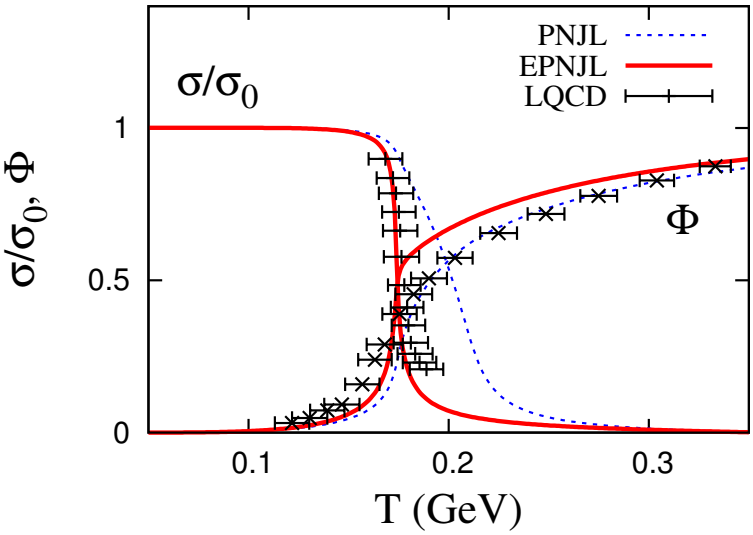

Figure 7.2: T dependence of the chiral condensate and the Polyakov loop at $\theta_q = 0$. The curves that decrease (increase) as T increases represent the chiral condensate (Polyakov loop). The solid (dashed) curves are the results of the EPNJL (PNJL) model. Here, the chiral condensate is normalized by the value σ_0 at vacuum. LQCD data (+) on σ and those ($\times$) on Φ are taken from Ref. [67].

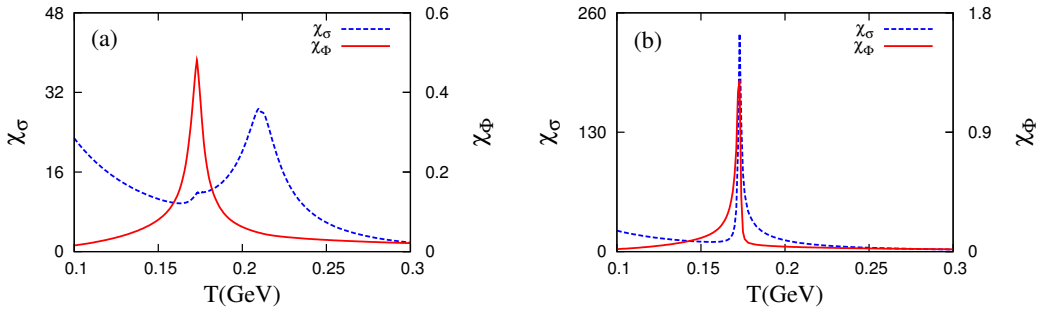

Figure 7.3: T dependence of the susceptibilities of the chiral condensate (dashed curve) and the Polyakov loop (solid curve) at $\theta_q = 0$. Panels (a) and (b) correspond to the PNJL and EPNJL models, respectively.

weak first-order. $|\Phi|$ has a small jump there although it is not explicitly seen in Fig. 7.4. Figure 7.5 represents χ_σ and χ_Φ as a function of T. Panel (a)

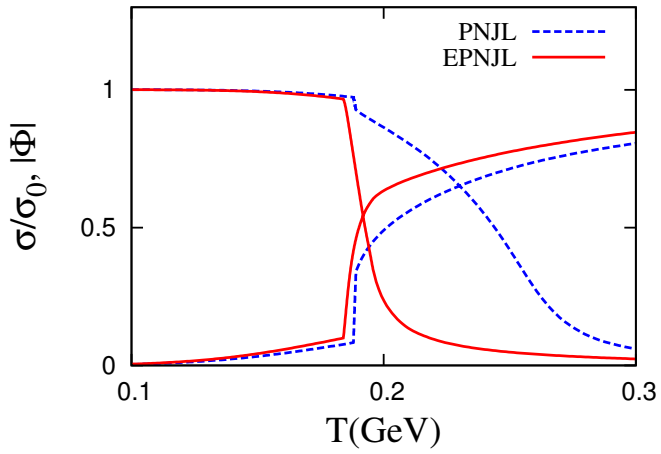

Figure 7.4: T dependence of the chiral condensate and the Polyakov loop at $\theta_q = \pi/3$. The meaning of the curves is the same as in Fig. 7.2.

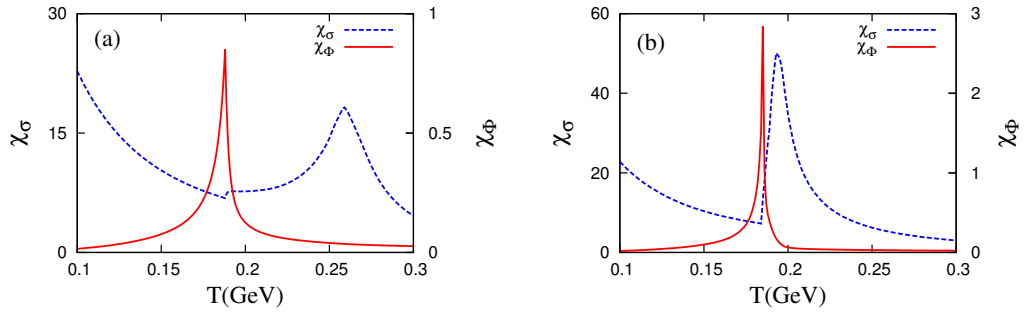

Figure 7.5: T dependence of the susceptibilities of the chiral condensate (dashed curve) and the Polyakov loop (solid curve) at $\theta_q = \pi/3$. Panels (a) and (b) correspond to the results of the PNJL and EPNJL models, respectively.

shows that $T_\sigma \gg T_\Phi$ in the PNJL model, while Panel (b) shows that $T_\sigma \approx T_\Phi$ in the EPNJL model. Thus, the entanglement vertex yields a stronger correlation between the chiral and deconfinement transitions also at $\theta_q = \pi/3$. Figure 7.6(a) shows θ_q dependence of the phase ϕ of the Polyakov loop Φ for four cases of $T/T_c = 0.97,\ 1.01,\ 1.04$, and 1.10 where $T_c = 173$ MeV is the critical temperature at $\mu_q = 0$. The EPNJL results (curves) well reproduce the LQCD data [36]

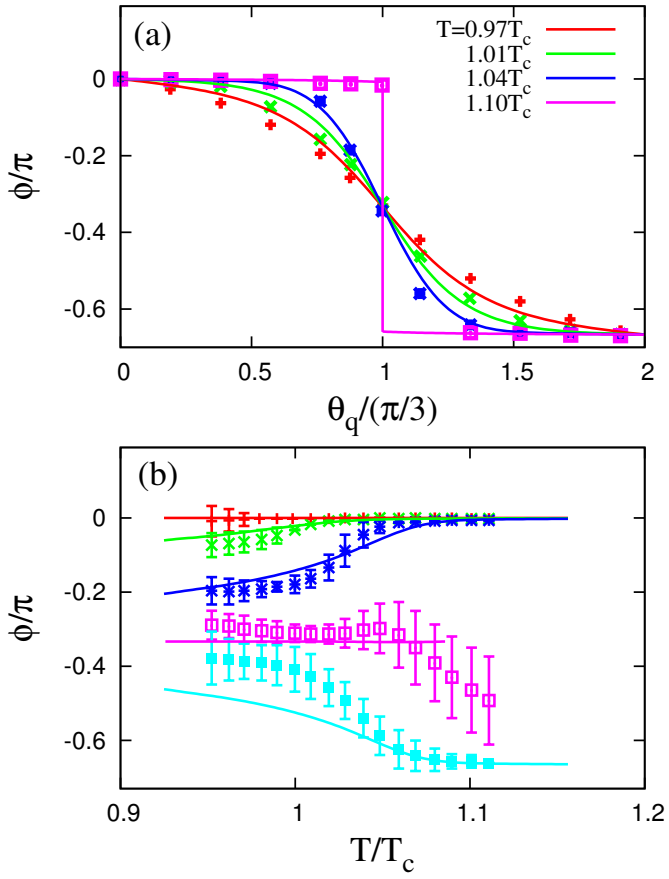

Figure 7.6: Phase ϕ of the Polyakov loop as a function of (a) $\theta_{\rm q}$ and (b) T. LQCD data [34; 36] are plotted by symbols. Curves represent results of EPNJL calculations. In panel (b), four cases (red, green, blue, pink and light-blue) from top to bottom represent results of $\theta_{\rm q} = 0,\ 0.8,\ \pi/3$, and 1.2, respectively. The pink line terminates at $T = T_{\rm RW}$, since ϕ is singular at $T > T_{\rm RW}$ in the case of $\theta_{\rm q} = \pi/3$.

(symbols). It is found from both results that ϕ is continuous at $\theta_q = \pi/3$ in the low-T side $T \leq T_{RW} = 1.07T_c$, but it is discontinuous at $\theta_q = \pi/3$ in the high-T side $T > T_{RW}$. Hence, the RW phase transition occurs at $\theta_q = \pi/3$ for $T > T_{RW}$. Figure 7.6(b) shows T dependence of ϕ for four cases of $\theta_q = 0,\ 0.8,\ \pi/3$, and 1.2. The EPNJL results (curves) also well reproduce the LQCD data [34] (symbols). For $\theta_q < \pi/3$ the phase ϕ tends to zero as T increases, while for $\theta_q > \pi/3$ it does to $-2\pi/3$ as T increases. For $\theta_q = \pi/3$, the RW phase transition occurs at $T > T_{RW}$ and then the phase ϕ is singular there, so that the pink line terminates at $T = T_{RW}$. In the high-T limit, the region (I) $-\pi/3 < \theta_q < \pi/3$ has $\phi = 0$ and the region (II) $\pi/3 < \theta_q < \pi$ does $\phi = -2\pi/3$. Thus, the region (II) is a $\mathbb{Z}_3$ image of the region (I), and the region (III) $\pi < \theta_q < 5\pi/3$ is another $\mathbb{Z}_3$ image of the region (I). Figure 7.7 shows the phase diagram in the θ_q-T plane. In the PNJL model, T_σ is much higher than T_Φ, while both are close to each other in the EPNJL model. The vertical dot-dashed lines at $\theta_q = \pi/3 \bmod 2\pi/3$ are the RW transition line and the $\mathbb{Z}_3$ images. The endpoint of the RW transition line is located at $T = T_{RW} = 190$ MeV in the PNJL model and at 185 MeV in the EPNJL model. On the RW transition line at $T > T_{RW}$, charge-conjugation symmetry is spontaneously broken, so that θ_q-odd quantities are discontinuous, while θ_q-even quantities have a cusp there as shown in Sec. 5.7. Thus, the θ_q-odd quantities such as the phase ψ of the modified Polyakov loop $\Psi = e^{i\theta_q}\Phi$ are order parameters of the RW phase transition. A current topic at imaginary μ_q is what the order of the RW transition is at the endpoint $T = T_{RW}$. The recent LQCD simulations show that it is first-order for small and larger quark masses, but the order is weakened and could be second-order at intermediate masses [68]. In the PNJL model, the transition is first-order as shown in Fig. 7.4. The deconfinement phase transition is first-order near the RW endpoint; the endpoint of the first-order deconfinement transition line is second-order, and susceptibilities of several quantities diverge simultaneously there. In the EPNJL model, such a first-order deconfinement transition line does not appear or very short even if it does emerge, since the deconfinement transition at the RW endpoint seems to be a very weak first-order transition. Figure 7.8 shows results of the EPNJL model for the RW phase transition. Panel (a) presents T dependence of the phase ψ of the modified Polyakov loop Ψ at $\theta_q = \pi/3$ for three cases $m_0 = 5,\ 150$, and 400 MeV.

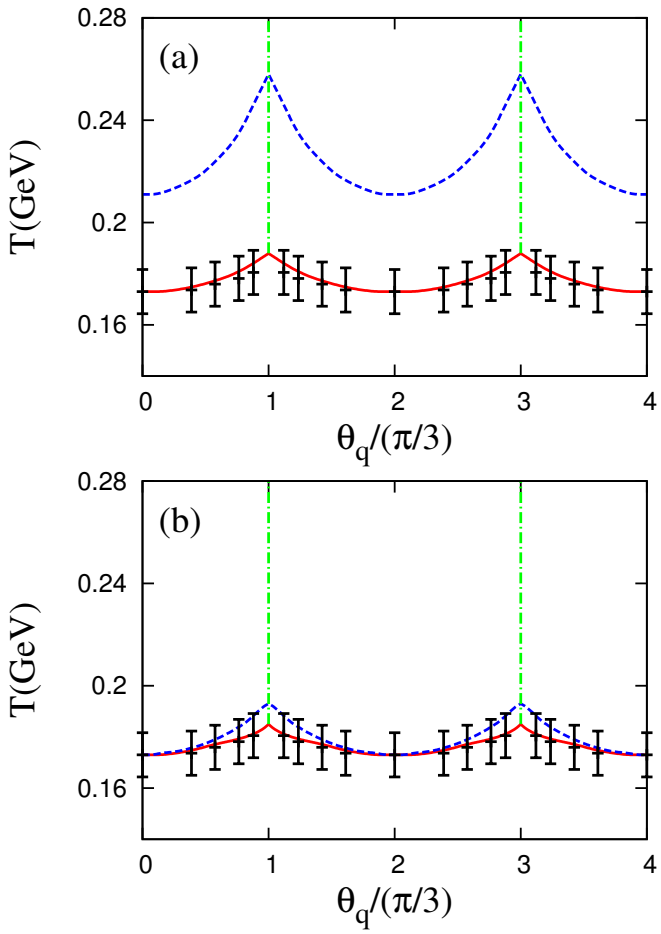

Figure 7.7: Phase diagram in θ_q-T plane. Panel (a) is the result of the standard PNJL model with no entanglement vertex, while panel (b) is the result of the EPNJL model with $(\alpha_1, \alpha_2) = (0.2, 0.2)$. The solid (dashed) curves represent the deconfinement (chiral) transition. The vertical dot-dashed lines denote the RW transition lines. Lattice data are taken from Ref. [34].

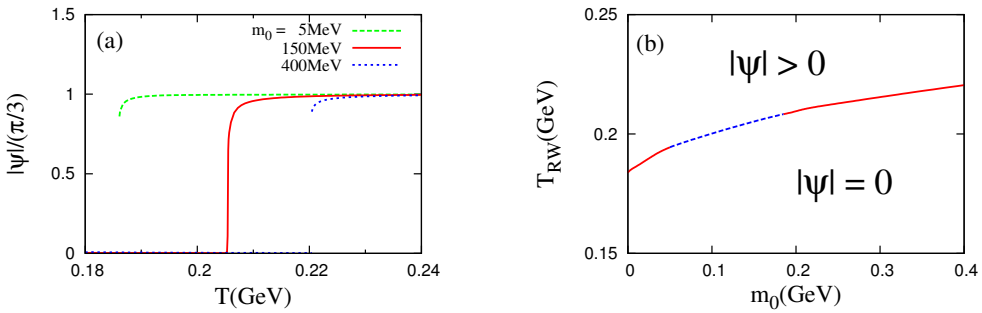

Figure 7.8: The RW phase transition in the EPNJL model. In panel (a), the phase of the modified Polyakov loop at $\theta_{\rm q} = \pi/3$ is plotted as a function of T for three cases of light, intermediate, and heavy quark masses. Panel (b) shows the phase diagram of the RW phase transition in the m_0-T plane. The solid (dotted) curve shows that the RW phase transition on the boundary is first-order (second-order).

The RW transition at the endpoint is first-order for $m_0 = 5$ and 400 MeV, but second-order for $m_0 = 150$ MeV. In the limit of large m_0, the transition is obviously first-order, since the quark contribution to Ω is suppressed and hence the deconfinement transition is controlled by the Polyakov potential U_Φ. Meanwhile, the RW endpoint is always first-order in the PNJL model. Panel (b) shows the phase diagram of the RW phase transition in the m_0-T plane; charge-conjugation symmetry is spontaneously broken above the curve, while it is preserved below the curve. The solid (dashed) curve shows that the RW phase transition is first-order (second-order) on the boundary. The critical mass $m_0(1 \to 2)$ $[m_0(2 \to 1)]$ from the first-order (second-order) to the second-order (first-order) transition is rather sensitive to the numerical accuracy. In the present numerical accuracy, the critical masses are $m_0(1 \to 2) = 50 \pm 5$ MeV and $m_0(2 \to 1) = 180 \pm 5$ MeV. This m_0 dependence of the order of the RW endpoint is consistent with the recent LQCD result [68]. Figure 7.9 shows the phase diagram of the EPNJL model in the whole $\mu_{\rm q}^2$-T. The solid, dotted, dashed and dot-dashed curves represent the first-order chiral phase transition, the crossover chiral transition, the crossover deconfinement transition and the RW transition, respectively. The transition line (dashed and solid curves) in the region $-0.0375 < \mu_{\rm q}^2 < 0.08$ [GeV^2] is expressed

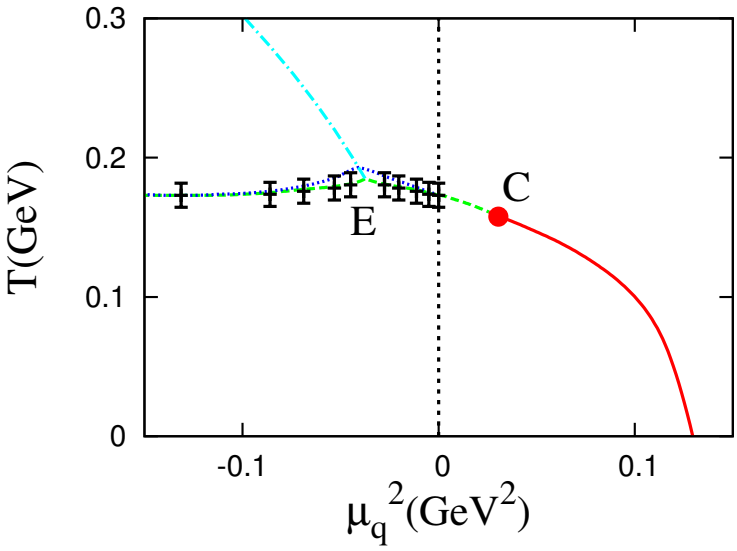

Figure 7.9: Phase diagram in the μ_q^2-T plane in the EPNJL model. The left (right) half-plane corresponds to imaginary (real) μ_q. The solid, dotted, dashed and dot-dashed curves represent the first-order chiral phase transition, the crossover chiral transition, the crossover deconfinement transition and the RW transition, respectively. Point C (E) is an endpoint of the first-order chiral (RW) transition. Lattice data are taken from Ref. [34].

as

$$T = c_0 + c_1\mu_{\rm q}^2 + c_2\mu_{\rm q}^4, \tag{7.4}$$

where $c_0 = 0.173$ [GeV], $c_1 = -0.377$ [GeV^{-1}], and $c_2 = -2.71$ [GeV^{-3}]. Point E is an endpoint of the RW transition, while point C is a CEP of the first-order chiral phase transition. The CEP is located at $(\mu_{\rm q}, T) = (160\text{MeV},\ 161\text{MeV})$ in the EPNJL model which is smaller $\mu_{\rm q}$ and larger T than the PNJL model result at (327MeV, 124MeV). Thus the entanglement vertex yields a drastic effect on the phase diagram at real $\mu_{\rm q}$.

7.3.2 Isospin chemical potential

The parameter set in the EPNJL model was determined in the previous subsection so as to reproduce LQCD data at zero and imaginary $\mu_{\rm q}$. The validity of the parameter set is confirmed in this subsection for real and imaginary $\mu_{\rm iso}$ where LQCD data are available. The formalism of the PNJL model at finite $\mu_{\rm iso}$ is shown in Chapter 6. The thermodynamic potential of the EPNJL model is obtained with $G_{\rm s}$ replaced by $G_{\rm s}(\Phi)$ in the potential (6.21) of the PNJL model. First, we consider the thermal system with imaginary $\mu_{\rm iso} = i\theta_{\rm iso}/\beta$. In Fig. 7.10,

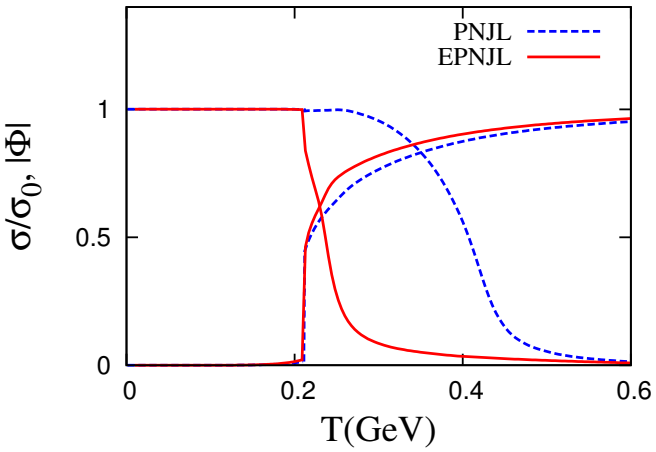

Figure 7.10: T dependence of the chiral condensate and the Polyakov loop at $\theta_{\rm iso} = \pi/2$ and $\mu_{\rm q} = 0$. See Fig. 7.2 for the meaning of lines.

we show T dependence of σ and Φ at $\theta_{\rm iso} = \pi/2$. For $\theta_{\rm iso} = \pi/2$, the u-quark loop contribution to the potential is nearly canceled by the d-quark loop contribution, so that the temperature dependence of the quark part of the potential becomes quite weak. In the PNJL model with no entanglement vertex, T dependence of σ is controlled by the quark part of the potential, while that of Φ is controlled by the Polyakov potential U_Φ. Therefore, the critical temperature T_σ of the chiral crossover transition is about twice the critical one T_Φ of the deconfinement first-order transition, i.e., $T_\sigma \approx 2T_\Phi$ in the PNJL model. LQCD data shows that the two transition are first-order and coincide with each other at $\theta_{\rm iso} = \pi/2$ [52][1] This indicates strong entanglement between the chiral restoration and the deconfinement transition. In the EPNJL model, the entanglement vertex induces a strong correlation between the chiral restoration and the deconfinement transition. Actually, as shown by the solid curves in Fig. 7.10, both the transitions are first-order and $T_\sigma \approx T_\Phi$. The EPNJL result is then consistent with the LQCD data. Next, we consider the thermal system with real $\mu_{\rm iso}$. Figure 7.11 shows T dependence of the Polyakov loop Φ at (a) $\mu_{\rm iso} = 0.96\mu^{\rm c}_{\rm iso}$ and (b) $1.4\mu^{\rm c}_{\rm iso}$, and that of the charged pion condensate π at (c) $\mu_{\rm iso} = 1.4\mu_{\rm c}$, where π is normalized by the value π_0 at $T = 0$ and $\mu^{\rm c}_{\rm iso}$ is the critical $\mu_{\rm iso}$ of the pion-superfluidity phase transition, that is $\mu^{\rm c}_{\rm iso} = M_\pi/2$ as shown in Secs. 6.2 and 6.4. LQCD data [51] are plotted by plus (+) symbols with 10% error bar coming from determining $T_{\rm c}$. The EPNJL model well reproduces all the LQCD data with no free parameter. Figure 7.12 shows the phase diagram in the $\mu_{\rm iso}$-T plane at $\mu_{\rm q} = 0$. The solid and dotted lines stand for the first-order and second-order pion-superfluidity transitions, respectively. The meeting point between the first-order and second-order transition lines is a tricritical point (TCP). The crossover chiral and deconfinement transitions agree with each other, as shown by the dashed line. The EPNJL result reproduces LQCD results [51] on the chiral and deconfinement transitions and also on the pion-superfluidity transition. The TCP is located at $(\mu_{\rm iso}, T) = (95\text{MeV},\ 170\text{MeV})$ in the EPNJL model which is smaller $\mu_{\rm iso}$ than the PNJL result at (401MeV, 171MeV). The entanglement vertex largely thus affects the location of the TCP.

[1]The LQCD data is the eight-flavor case since the two-flavor case is not available.

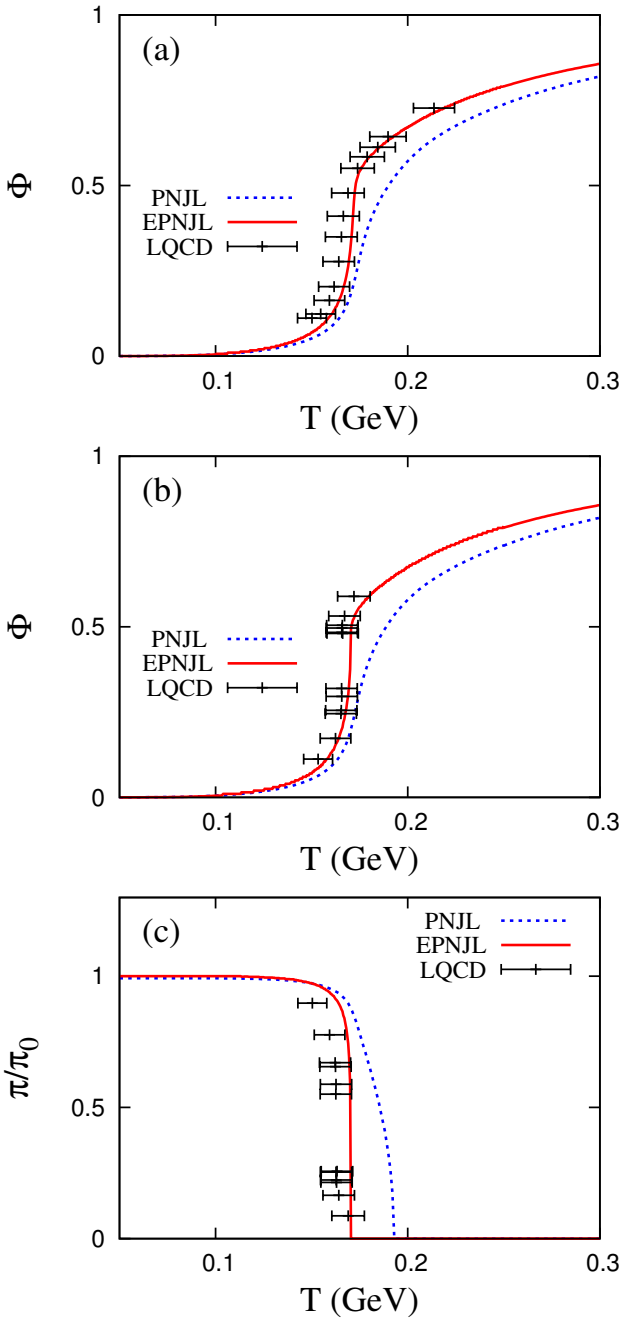

Figure 7.11: T dependence of the Polyakov loop Φ at (a) $\mu_{\rm iso} = 0.96\mu^{\rm c}_{\rm iso}$ and (b) $1.4\mu^{\rm c}_{\rm iso}$, and that of the charged pion condensate π at (c) $\mu_{\rm iso} = 1.4\mu^{\rm c}_{\rm iso}$. The solid (dotted) curve represents the EPNJL (PNJL) result. LQCD data are taken from Ref. [51].

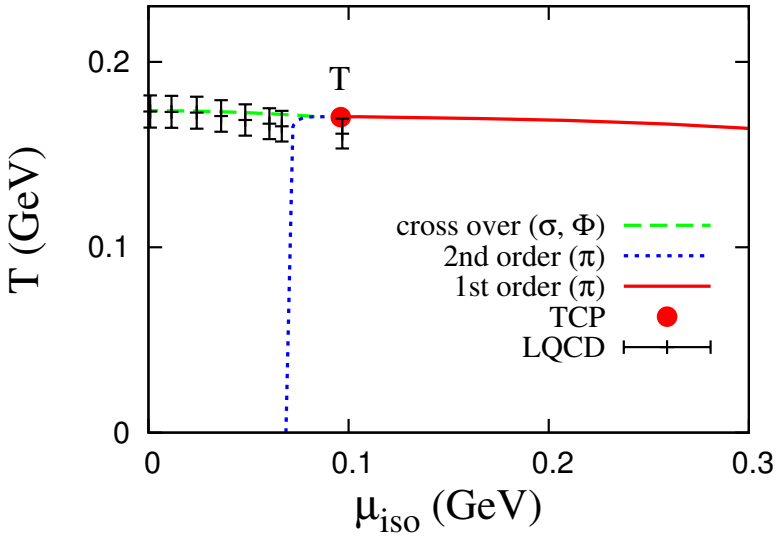

Figure 7.12: Phase diagram in the $\mu_{\rm iso}$-T plane at $\mu_{\rm q} = 0$ in the EPNJL model. The solid (dotted) line represents the first-order (second-order) pion-superfluidity transition, while the dashed line does the chiral and deconfinement crossover transition. Point T is a tricritical point (TCP). LQCD data are taken from Ref. [51].

7.3.3 Small real quark chemical potential

Finally, we test the reliability of the EPNJL model by comparing the model results with LQCD data on the equation of state (EOS) at real $\mu_{\rm q}$. For small real $\mu_{\rm q}$, LQCD data evaluated by the Taylor expansion [70] is available. Figure 7.13 shows (a) the pressure p, (b) the energy density ε at $\mu_{\rm q} = 0$ and (c) the quark-number density $\rho_{\rm q}$ at $\mu_{\rm q} = 0.8T_{\rm c}$. For p and ε, LQCD data [69] provide only the deviations, $p - p_0$ and $\varepsilon - \varepsilon_0$, from $T_0 = 0.9T_{\rm c}$. Hence, p_0 and ε_0 at $T = T_0$ are evaluated in the free-gas model of hadrons with vacuum masses. This procedure is reliable at $T = 0.9T_{\rm c}$, because p and ε are dominated by the hadron components there. The p and ε thus estimated from the LQCD data [69] are shown by the dots in panels (a) and (b); note that in these panels p and ε are normalized by the values in the Stefan-Boltzmann limit. In panel (c), $\rho_{\rm q}$ is nondimensionalized by T^3. For all the quantities, the EPNJL results (solid lines) are more consistent with LQCD data [69; 70] than the PNJL results (dashed lines) as shown in Fig. 7.13. The entanglement interaction makes the chiral symmetry restoration faster, so that the EPNJL model has rapid change in the quantities with T. Hence the model reproduces the sharp change of LQCD result better than the PNJL model. For $\rho_{\rm q}$, however, the EPNJL model underestimates LQCD results [70] at $T < T_{\rm c}$, because the model has no hadronic excitation effects in the mean field calculation. The hadronic excitations are considered as free gas for $T < T_{\rm c}$ where hadrons have no decay modes. This approximation is discussed in Sec. 6.3.6 and the thermodynamic potential $\Omega_{\rm q+h}$ with hadronic excitations is expressed in (6.34)-(6.36). Here we consider the nucleons with the physical mass and the pions with the same mass $M_\pi = 280$MeV as the LQCD calculation. The new $\rho_{\rm q}$ is plotted by the dotted line up to $T_{\rm c}$ in panel (c). This line agrees with the LQCD data at $T < T_{\rm c}$. By considering the hadronic excitations, the EPNJL result is consistent with LQCD data in all the regions.

7.4 Summary

We have extended the PNJL model by introducing an entanglement vertex depending on the Polyakov loop phenomenologically. The effective vertex generates

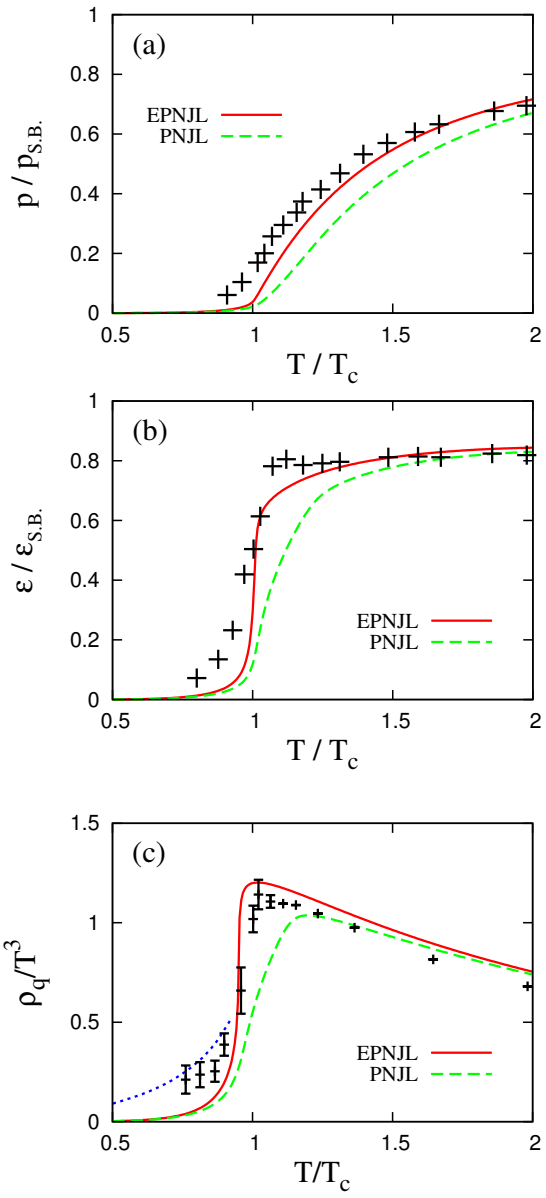

Figure 7.13: T dependence of (a) the pressure p and (b) the energy density ε at $\mu_{\rm q} = 0$ and (c) the quark-number density $\rho_{\rm q}$ at $\mu_{\rm q}/T_{\rm c} = 0.8$. The pressure and the energy density are divided by the values in the Stefan-Boltzmann limit, while the net quark-number density is divided by T^3. The solid (dashed) lines show the EPNJL (PNJL) result. The LQCD data, shown by points with error bars, are taken from Ref. [69] in panels (a) and (b) and from Ref. [70] in panel (c).

entanglement interactions between the chiral condensate σ and the Polyakov loop Φ. As a result of the strong entanglement, the chiral and deconfinement transitions occur simultaneously. The functional form of the entanglement vertex is determined by respecting the extended $\mathbb{Z}_3$ symmetry and charge-conjugation symmetry. The strength of the entanglement vertex is determined by LQCD data at imaginary quark chemical potential $\mu_{\rm q}$, and the validity of this model building is confirmed by LQCD data at real and imaginary isospin chemical potentials $\mu_{\rm iso}$. The EPNJL model can reproduce the LQCD data in all the regions. Furthermore the model reproduces the LQCD data evaluated by the Taylor expansion at small real $\mu_{\rm q}$. The entanglement vertex yields a drastic effect on the location of the critical endpoint of the chiral transition at real $\mu_{\rm q}$. It is reported in Ref. [71] that the EPNJL model is also consistent with LQCD data in the case with the strong magnet field, which is relevant to magnetars of the neutron stars and non-central heavy-ion collisions. The present phenomenological approach seems to be complementary to the exact renormalization-group approach. It is highly expected that the functional form and the strength of the entanglement vertex will be determined in future by the theoretical approach.

Chapter 8

Conclusions

In this thesis, we have proposed a new strategy to investigate the QCD phase diagram at finite quark chemical potential $\mu_{\rm q}$. Study of the phase diagram is relevant for the early universe, compact stars and heavy-ion collisions. The first-principle lattice QCD (LQCD) suffers from the sign problem at real $\mu_{\rm q}$ where the integrand of the partition function is complex and LQCD techniques break down. Therefore the QCD phase diagram at finite $\mu_{\rm q}$ is unclear. There are some regions with no sign problem, imaginary $\mu_{\rm q}$ and real and imaginary isospin chemical potentials $\mu_{\rm iso}$. We then propose an analytic continuation from the regions with no sign problem to the real $\mu_{\rm q}$ region by using an effective model that can evaluate the QCD partition function in all the regions. The Polyakov-loop extended Nambu–Jona-Lasinio (PNJL) model is an effective model that can do this. We showed that the PNJL model reproduces LQCD data qualitatively in all the regions with no sign problem, but not quantitatively. We then extended the PNJL model in order to reproduce the LQCD data quantitatively. First, we investigated the sign problem by using the PNJL model. We evaluated the average phase factor as an indicator of the sign problem. The severe region where the factor is small or zero spreads widely over the phase diagram. It is thus difficult to investigate the phase diagram by LQCD directly. In order to circumvent this difficulty, we proposed the strategy of the analytic continuation from the regions with no sign problem to the real $\mu_{\rm q}$ region. For imaginary $\mu_{\rm q}$, the QCD partition function is a function of $\mu_{\rm q}^2$ and the physical quantities can be analytically continued from imaginary $\mu_{\rm q}$ to real $\mu_{\rm q}$. The partition function with real $\mu_{\rm q}$ is obtained mathematically

from that with imaginary $\mu_{\rm q}$ through the Fourier transformation. For real and imaginary $\mu_{\rm iso}$, the validity of the strategy is confirmable by comparing LQCD data in both the regions. The real $\mu_{\rm iso}$ region is also relevant to neutron stars and relativistic heavy-ion collisions. Therefore all the regions are relevant to the phase diagram at real $\mu_{\rm q}$. We investigated the imaginary $\mu_{\rm q}$ region and the real and imaginary $\mu_{\rm iso}$ regions by using the PNJL model. For all the regions, the PNJL model reproduces LQCD data qualitatively. However, there is a sizable difference between the PNJL results and the LQCD data for the coincidence of the chiral and deconfinement transitions. The two transitions coincide with each other in LQCD, but in the PNJL model. Thus the correlation between the two transitions is weaker in the PNJL model than in LQCD. In order to solve this problem, we extended the PNJL model by introducing an entanglement vertex depending on the Polyakov loop. The effective vertex generates entanglement interactions between the chiral condensate and the Polyakov loop. As a result of the strong entanglement, the chiral and deconfinement transitions occur simultaneously. The new model reproduces the LQCD data quantitatively in all the regions with no sign problem. Furthermore the model reproduces the LQCD data evaluated by the Taylor expansion at small real $\mu_{\rm q}$. Finally we predicted the QCD phase diagram with the new model. The entanglement vertex yields a drastic effect on the location of the critical endpoint of the chiral transition at real $\mu_{\rm q}$.

References

[1] J. B. Kogut and M. A. Stephanov, *The Phases of Qauntym Chromodynamics*, Cambridge University Press (2004); K. Yagi, T. Hatsuda and Y. Miake, *Quark-Gluon Plasma*, Cambridge University Press (2005) 3

[2] D. J. Gross and F. Wilczek, Phys. Rev. Lett. **30**, 1343 (1973); H. D. Politzer, Phys. Rev. Lett. **30**, 1346 (1973). 4

[3] B. L. Friman, *et al*, Lect. Notes in Phys. **814**, Springer (2011). 10

[4] A. Casher, Phys. Lett. B**83**, 395 (1979). 8

[5] S. Coleman and E. Witten, Phys. Rev. Lett. **45**, 100 (1980). 8

[6] G. 't Hooft, *Recent Developments in Gauge Theories*, Plenum Press (1980) ; S. Coleman and B. Grossman, Nucl. Phys. B**203**, 205 (1982). 8

[7] M. Gell-Mann, R. J. Oakes, and B. Renner, Phys. Rev. **175**, 2195 (1968). 6

[8] K.G. Wilson, Phys. Rev. D**14**, 2455 (1974). 7

[9] A. M. Polyakov, Phys. Lett. B**72**, 477 (1978); L. Susskind, Phys. Rev. D**20**, 2610 (1979). 11

[10] L. D. McLerran and B. Svetitsky Phys. Rev. D**24**, 450 (1981); S. Nadkarni, Phys. Rev. D**33**, 3738 (1986); Phys. Rev. D**34**, 3904 (1986). 11

[11] B. Svetitsky and L. G. Yaffe, Nucl. Phys. B**210**, 423 (1982); B. Svetitsky, Phys. Rept. **132**, 1 (1986). 11

[12] I. M. Barbourt, Nucl. Phys. A**642**, 251 (1998); Z. Fodor and S. D. Katz, Phys. Lett. B**534**, 87 (2002); JHEP **03**, 014 (2002). 12

[13] C. R. Allton, *et al*, Phys. Rev. D**66**, 074507 (2002); Phys. Rev. D**71**, 054508 (2005); R. V. Gavai and S. Gupta, Phys. Rev. D**78**, 114503 (2008). 12

[14] Y. Nambu and G. Jona-Lasinio, Phys. Rev. **122**, 345 (1961); Phys. Rev. **124**, 246 (1961). 14

[15] U. Vogl and W. Weise, Prog. Part. Nucl. Phys. **27**, 195 (1991); S. P. Klevansky, Rev. Mod. Phys. **64**, 649 (1992); T. Hatsuda and T. Kunihiro, Phys. Rept. **247**, 221 (1994); M. Buballa, Phys. Rept. **407**, 205 (205). 14

[16] A. Di Giacomo, H.G. Dosch, V.I. Shevchenkoc, Yu. A. Simonov, Phys. Rept. **372**, 319 (2002). 15

[17] J. Polónyi and K. Szlachányi, Phys. Lett. B**110**, 395 (1982); M. Gross, Phys. Lett. B**132**, 125 (1983). 16

[18] E.-M. Ilgenfritz and J. Kripfganz, Z. Phys. C**29**, 79 (1985); A. Gocksch and M. Ogilvie, Phys. Rev. D**31**, 877 (1985); A. Gocksch and R. D. Pisarski, Nucl. Phys. B**402**, 657 (1993); F. Lenz and M. Thies, Ann. Phys. **268**, 308 (1998). 17

[19] G. Boyd, *et al*, Nucl. Phys. B**469**, 419 (1996); S. Gupta, K. Huebner and O. Kaczmarek, Phys. Rev. D**77**, 034503 (2008). 17

[20] K. Kashiwa, H. Kouno, T. Sakaguchi, M. Matsuzaki, and M. Yahiro, Phys. Lett. B**647**, 446 (2007). 21

[21] B. -J. Schaefer, J.M. Pawlowski, and J. Wambach, Phys. Rev. D**76**, 074023 (2007). 22

[22] Y. Sakai, T, Sasaki, H. Kouno and M. Yahiro, Phys. Rev. D**82**, 096007 (2010). 26

[23] A. Dumitru, Y. Hatta, J. Lenaghan, K. Orginos and R. D. Pisarski, Phys. Rev. D**70**, 034511 (2004). 28

[24] A. Dumitru, R. D. Pisarski and D. Zschiesche, Phys. Rev. D**72**, 065008 (2005). 28

[25] S. Rößner, C. Ratti and W. Weise, Phys. Rev. D**75**, 034007 (2007); S. Rößner, T. Hell, C. Ratti and W. Weise, Nucl. Phys. A**814**, 118 (2008). 17, 25, 29, 34, 38, 48

[64] K. Fukushima, Phys. Lett. B**591**, 277 (2004). 16, 29, 98

[27] J. Danzer, C. Gattringer, C. Liptak and M. Marinkovic, Phys. Lett. B**682**, 240 (2009). 30

[28] K. Splittorff and J. J. M. Verbaarschot, Phys. Rev. D**75**, 116003 (2007); Phys. Rev. D**77**, 014514 (2008). 30

[29] J. C. R. Bloch and T. Wettig, JHEP **0903**, 100 (2009). 30

[30] J. Hüfner, S. P. Klevansky, P. Zhuang and H. Voss, Ann. Phys. **234**, 225 (1994); P. Zhuang, J. Hüfner and S. P. Klevansky, Nucl. Phys. A**576**, 525 (1994). 35

[31] M. D'Elia and F. Sanfilippo, Phys. Rev. D**80**, 014502 (2009). 39, 41, 72, 76, 84, 86, 88, 89, 92

[32] Y. Sakai, K. Kashiwa, H. Kouno and M. Yahiro, Phys. Rev. D**77**, 051901(R) (2008); Phys. Rev. D**78**, 036001 (2008); Y. Sakai, K. Kashiwa, H. Kouno, M. Matsuzaki and M. Yahiro, Phys. Rev. D**78**, 076007 (2008); Phys. Rev. D**79**, 076008 (2009); Phys. Rev. D**79**, 096001 (2009); H. Kouno, M. Yahiro, H. Kouno, M. Matsuzaki and Y. Sakai, J. Phys. G**36**, 105001 (2009); H. Kouno, Y. Sakai, K. Kashiwa and M. Yahiro, J. Phys. G**36**, 115010 (2009); H. Kouno, Y. Sakai, T. Sasaki, K. Kashiwa and M. Yahiro, Phys. Rev. D**83**, 076009 (2011). 45

[33] A. Roberge and N. Weiss, Nucl. Phys. B**275**, 734 (1986). 46, 48, 49, 50, 51

[34] P. de Forcrand and O. Philipsen, Nucl. Phys. B**642**, 290 (2002); Nucl. Phys. B**673**, 170 (2003). 12, 45, 47, 56, 63, 64, 104, 105, 106, 108

[35] M. D'Elia and M. P. Lombardo, Phys. Rev. D**67**. 014505 (2003); Phys. Rev. D**70**, 074509 (2004); M. D'Elia, F. D. Renzo and M. P. Lombardo, Phys. Rev. D**76**, 114509 (2007). 12, 45, 47, 58, 59, 63, 64

[36] H. S. Chen and X. Q. Luo, Phys. Rev. D**72**, 034504 (2005); arXiv:hep-lat/0702025 (2007); L. K. Wu, X. Q. Luo and H. S. Chen, Phys. Rev. D**76**, 034505 (2007). 12, 45, 47, 63, 64, 103, 104

[37] K. Nagata and A. Nakamura, Phys. Rev. D**83**, 114507 (2011). 12, 45, 47, 57, 63, 64

[38] HotQCD Collaboration, A. Bazavov, *et al*, Phys. Rev. D**80**, 014504 (2009); M. Cheng, *et al*, Phys. Rev. D**81**, 054504 (2010). 47, 98

[39] Wuppertal-Budapest Collaboration, S. Borsányi, *et al*, JHEP **11**, 077 (2010); JHEP **09**, 073 (2010); Nucl. Phys. A**855**, 253 (2011). 47, 98

[40] M. A. Stephanov, PoS, LAT2006, 024 (2006). 47, 48

[41] M. Asakawa and K. Yazaki, Nucl. Phys. A**504**, 668 (1989). 48

[42] M. A. Halasz, A. D. Jackson, R. E. Shrock, M. A. Stephanov and J. J. M. Verbaarschot, Phys. Rev. D**58**, 096007 (1998). 48

[43] O. Scavenius, A. Mocsy, I. N. Mishustin and D. H. Rischke, Phys. Rev. C**64**, 045202 (2001). 48

[44] Y. Hatta and T. Ikeda, Phys. Rev. D**67**, 014028 (2003). 48

[45] R. V. Gavai and S. Gupta, Phys. Rev. D**71**, 114014 (2005). 48

[46] Z. Fodor and S. D. Katz, JHEP **0404**, 050 (2004). 48

[47] R. Dashen, Phys. Rev. D**3**, 1879 (1971). 66

[48] E. Witten, Ann. Phys. **128**, 363 (1980). 66

[49] Y. Sakai, H. Kouno and M. Yahiro, J. Phys. G**37**, 105007 (2010); T. Sasaki, Y. Sakai, H. Kouno and M. Yahiro, Phys. Rev. D**82**, 116004 (2010). 71, 75

[50] D. T. Son and M. A. Stephanov, Phys. Rev. Lett. **86**, 592 (2001). 72, 73, 74

[51] J. Kogut and D. Sinclair, Phys. Rev. D**66**, 034505 (2002); Phys. Rev. D**66**, 014508 (2002); Phys. Rev. D**70**, 094501 (2004). 72, 92, 110, 111, 112

[52] P. Cea, L. Cosmai, M. D'Elia, C. Manneschi and A. Papa, Phys. Rev. D**80**, 034501 (2009). 72, 90, 91, 110

[53] D. Weingarten, Phys. Rev. Lett. **51**, 1830 (1983); E. Witten, Phys. Rev. Lett. **51**, 2351 (1983); S. Nussinov, Phys. Rev. Lett. **52**, 966 (1984); D. Espriu, M. Gross, and J. F. Wheater, Phys. Lett. B**146**, 67 (1984). 73

[54] J. B. Kogut and D. Toublan, Phys. Rev. D**64**, 034007 (2001); K. Splittorff, D. T. Son, and M. A. Stephanov, Phys. Rev. D**64**, 016003 (2001); M. Loewe and C. Villavicencio, Phys. Rev. D**67**, 074034 (2003); Phys. Rev. D**70**, 074005 (2004). 92

[55] D. Toublan and J. B. Kogut, Phys. Lett. B**564**, 212 (2003); A. Barducci, R. Casalbuoni, G. Pettini, and L. Ravagli, Phys. Rev. D**69**, 096004 (2004); Phys. Rev. D**71**, 016011 (2005). L. He, M. Jin and P. Zhuang, Phys. Rev. D**71**, 116001 (2005). 92

[56] Z. Zhang and Y. -X. Liu, Phys. Rev. C**75**, 064910 (2007); J. Xiong, M. Jin, J. Li, J .Phys. G**36**, 125005 (2009) 92

[57] Y. Sakai, T. Sasaki, H. Kouno and M. Yahiro, Phys. Rev. D**82**, 076003 (2010); arXiv: 1104.2394 [hep-ph] (2011); Y. Sakai, H. Kouno, T. Sasaki, M. Yahiro, Phys. Lett. B**705**, 349 (2011) 97

[58] J. Cleymans, K. Redlich, H.Satz and E.Suhonen, Z. Phys. C**33**, 151 (1986); H. Kouno and F. Takagi, Z. Phys. C**42**, 209 (1989). 97

[59] L. McLerran and R. D. Pisarski, Nucl. Phys. A**796**, 83 (2007); Y. Hidaka, L. McLerran and R. D. Pisarski, Nucl. Phys. A**808**, 117 (2008). 97

[60] A. Barducci, R. Casalbuoni, G. Pettini, and R. Gatto, Phys. Lett. B**301**, 95 (1993). 97

[61] H. Fujii, Phys. Rev. D**67**, 094018 (2003). 97

[62] F. Karsch and E. Laermann, Phys. Rev. D**50**, 6954 (1994); F. Karsch, Lect. Notes Phys. **583**, 209-249 (2002). 98

[63] S. Borsányi, *et al*, arXiv:1005.3508 [hep-lat] (2010). 98

[64] K. Fukushima, Phys. Lett. B**591**, 277 (2004). 16, 29, 98

[65] J. Braun, L. M. Haas, F. Marhauser, and J. M. Pawlowski, Phys. Rev. Lett. **106**, 022002 (2011); K.-I. Kondo, Phys. Rev. D**82**, 065024 (2010). 98, 100

[66] C. Wetterich, Phys. Lett. B**301**, 90 (1993). 98, 100

[67] F. Karsch, E. Laermann, and A. Peikert, Nucl. Phys. B**605**, 579 (2001); F. Karsch, Lect. Notes Phys. **583**, 209 (2002). 99, 101, 102

[68] M. D'Elia and F. Sanfilippo, Phys. Rev. D**80**, 111501(R) (2009); M. D'Elia, S. Mukherjee, F. Sanfilippo, Phys. Rev. D**83**, 054505 (2011): P. de Forcrand and O. Philipsen, Phys. Rev. Lett. **105**, 152001 (2010). 101, 105, 107

[69] A. Ali Khan, *et al*, Phys. Rev. D**64**, 074510 (2001). 113, 114

[70] C. R. Allton, *et al*, Phys. Rev. D**68**, 014507 (2003). 113, 114

[71] R. Gatto, and M. Ruggieri, Phys. Rev. D**83**, 034016 (2011). 115